



大湾区显微科学与技术研究中心

Bay Area Center for Electron Microscopy

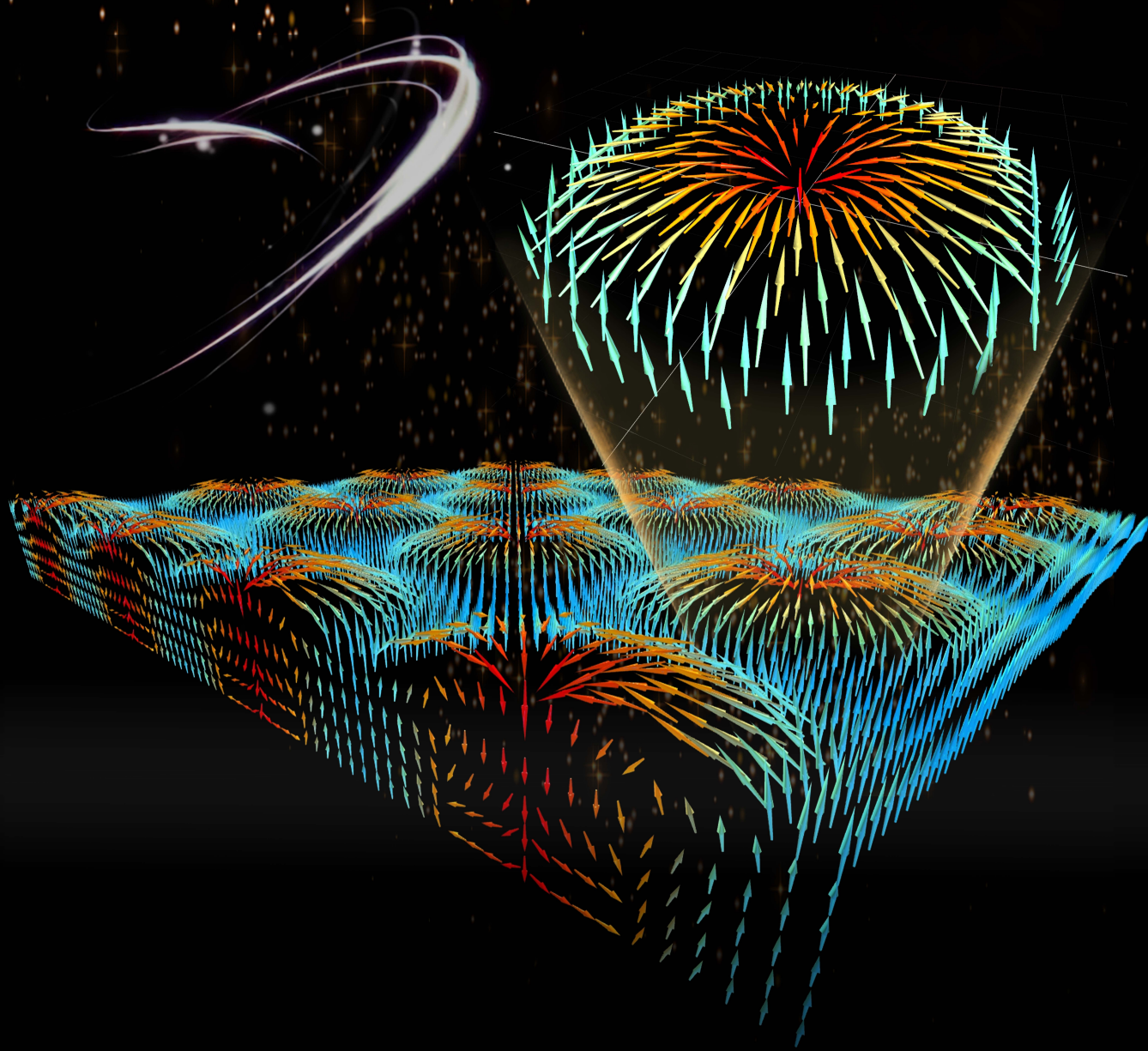
# 简讯

## 第12期

松山湖材料实验室

广东省东莞市大朗镇屏东路333号

Email: [bacem@sslaborg.cn](mailto:bacem@sslaborg.cn)



2025年第1期 (总第12期)

出版日期: 2025年2月10日



## 铁电拓扑有序态研究取得重要进展(Nature Nanotechnology 2025)

铁电拓扑结构在非易失性和超高密度信息存储等方面具有重要的应用价值。然而，高密度的存储应用必然依赖于大范围铁电拓扑畴的有序化分布。

近日，大湾区显微科学与技术研究中心耿皖荣、朱银莲、马秀良等在实验上发现极性斯格明子超晶体，并证实多波矢相互耦合进而稳定极性斯格明子超晶体的物理模型；中国科学院金属研究所博士生朱美雄通过相场模拟确定了电学 Dzyaloshinskii-Moriya 相互作用在铁电拓扑有序态形成中发挥的决定性作用。2025 年 1 月 16 日，相关研究结果以“Dipolar wavevector interference induces a polar skyrmion lattice in strained BiFeO<sub>3</sub> films”为题，在线发表在《自然-纳米科技》(Nature Nanotechnology)期刊上。

这一发现是继通量全闭合(Science, 2015)、双相涡旋(ACS Nano, 2018)、半子(Nature Materials, 2020)、电偶极化波(Science Advances, 2021)、布洛赫点(Nature Communications, 2024)之后，该研究团队在有关铁电拓扑畴结构方面的又一项重要进展。

自铁电拓扑结构相继通过实验发现以来，基于外场作用下的原位电子显微学方法证实了拓扑结构及其结构演化的可控性，强化了其作为存储功能单元的可行性。然而，稳定、高密度的存储应用必然依赖于大范围铁电拓扑畴的有序化定向分布，其形成前提是铁电体系内引入周期性的应变、电场分布及沿有序化方向的协同耦合，这就需要通过巧妙的实验设计使铁电体在特定边界条件下实现各种能量态的平衡。

以往研究中多数基于超晶格/多层膜中复杂界面效应调控出极性拓扑结构，通常以平行于薄膜表面的一维有序态分布为主要特征。这类一维有序态作为信息技术的功能单元应用于超高密度存储难度较大。

该研究团队通过原子尺度的外延生长，在 LaAlO<sub>3</sub> 衬底上制备出极大压应变(4.36%)下的 BiFeO<sub>3</sub> 超薄薄膜。像差校正条件下的透射电子显微学成像以及在此基础上的定量分析发现 BiFeO<sub>3</sub> 薄膜中具有一维(1D)和二维(2D)超结构调制。二维调制结构伴随着周期性的电场和应变分布，并稳定了网格状分布的铁电斯格明子晶体。该斯格明子晶体在倒空间表现为两个倒易方向上的周期性超衍射峰，因此可归类为双波矢(2 $q$ )的拓扑有序态。另外，以单波矢(1 $q$ )为特征的一维拓扑有序态实现了涡旋管阵列的稳定。

铁电斯格明子晶体的形成可归因于两个相互垂直的单波矢(1 $q$ )拓扑有序态相交并交互作用，它们在相交区域晶格、电荷的协同耦合进而形成双波矢(2 $q$ )的拓扑有序态，即斯格明子晶体。该工作在实验上证实了铁磁体系中关于形成拓扑有序态的物理模型在铁电体系中的相似性。

该工作表明在铁电材料中，拓扑有序态的周期和对称性能够得到有效的调控，未来有望进一步发现各向同性拓扑有序、各向异性拓扑有序等新型多重波矢拓扑态。这些新型拓扑态及其伴随的新奇物理特性必然为新一代铁电存储带来更广的应用。(原文附后)



## 电场调控铁电拓扑结构研究取得新进展(Advanced Materials 2025)

铁电极化拓扑结构具有纳米级三维尺寸、拓扑保护性、负电容等特点，在高密度、非易失性、低功耗信息存储器方面具有广泛的应用前景。利用外场对铁电拓扑畴实现精确操控并研究其在外场下的动力学行为，有助于加速铁电拓扑畴在信息存储器中的应用进程。

近日，大湾区显微科学与技术研究中心冯燕朋、朱银莲、马秀良等人利用原位电子显微技术实现了铁电极化拓扑畴结构的电场调控。2024年12月17日，Advanced Materials 以“Reversible Manipulation of Polar Topologies in Oxide Ferroelectrics via Electric Fields”为题在线发表了该研究成果。

该研究团队在前期工作(Science, 2015; Nano Letters, 2017)的基础上，设计并利用脉冲激光沉积设备生长了  $\text{PbTiO}_3/\text{SrTiO}_3$  双层膜与  $(\text{PbTiO}_3/\text{SrTiO}_3)_5$  多层膜，利用原位透射电子显

微技术首先在双层膜中利用外加电场实现了 a/c 畴到大尺度全闭合阵列的转变，并且发现该转变是可逆的。结合原子尺度原位 STEM 成像、应变分析和离子位移提取发现在 2V 下 a/c 畴可转变为极化呈顺时针和逆时针交替排列的全闭合畴结构。同时对  $(\text{PbTiO}_3/\text{SrTiO}_3)_5$  多层膜施加电场观察到了 a/c 畴到全闭合畴的转变细节，具体表现为：首先在原 a 畴区域形成极化方向相反的 c 畴，该 c 畴随着电压的增加逐渐长大并于原 c 畴相连接，进而形成大尺度全闭合阵列。利用相场模拟证实了这一转变过程，并揭示了静电能的降低是这一转变的主要驱动力。该项工作利用外加电场实现了铁电全闭合畴的可逆调控，揭示了全闭合畴在外场下的动力学行为，并论证了外加电场或可作为一种新的手段实现对其他铁电拓扑畴的精确调控。(原文附后)

## 反铁电体储能性能研究取得重要进展(Nature 2025)

近日，清华大学南策文院士和林元华教授领导的研究团队与澳大利亚伍伦贡大学张树君教授以及大湾区显微科学与技术研究中心姜如建(博士生)、朱银莲、马秀良合作，提出了一种通过引入非极性或极性成分来阻挫反铁电体中反极性有序的新策略，该方法能够有效调节反铁电-铁电相变场，并显著降低电滞损耗，使  $\text{PbZrO}_3$  基薄膜在 5.51 MV/cm 的电场下实现了

189 J/cm<sup>3</sup> 的高能量密度和 81% 的高效率，创下了反铁电体领域的新纪录。他们通过像差校正透射电子显微镜的原子尺度解析，直接展示了随机分布的非极性区域有效阻挫了长程反极性有序，揭示了储能性能之所以提高的微观机理。2025年1月30日，相关结果以“Enhanced energy storage in antiferroelectrics via antipolar frustration”为题发表在 Nature 上。(原文附后)

# Dipolar wavevector interference induces a polar skyrmion lattice in strained BiFeO<sub>3</sub> films

Received: 12 October 2023

Accepted: 4 December 2024

Published online: 16 January 2025

 Check for updates

W. R. Geng<sup>1,10</sup>, Y. L. Zhu<sup>1,2,3,10</sup>, M. X. Zhu<sup>1,2,4,10</sup>, Y. L. Tang<sup>1,2</sup>, H. J. Zhao<sup>5</sup>,  
C. H. Lei<sup>6</sup>, Y. J. Wang<sup>1,2</sup>, J. H. Wang<sup>2,4</sup>, R. J. Jiang<sup>2,4</sup>, S. Z. Liu<sup>2,4</sup>, X. Y. San<sup>7</sup>,  
Y. P. Feng<sup>1</sup>, M. J. Zou<sup>1</sup> & X. L. Ma<sup>1,8,9</sup> ✉

Skyrmions can form regular arrangements, so-called skyrmion crystals (SkXs). A mode with multiple wavevectors  $\mathbf{q}$  then describes the arrangement. While magnetic SkXs, which can emerge in the presence of Dzyaloshinskii–Moriya interaction, are well established, polar skyrmion lattices are still elusive. Here we report the observation of polar SkXs with a well-defined double- $\mathbf{q}$  state in ultrathin BiFeO<sub>3</sub> films on LaAlO<sub>3</sub>. The compressive strain induced by the LaAlO<sub>3</sub> substrate yields a dipolar topological texture with a periodic arrangement of skyrmions. The square-like superstructure with a lattice constant of 2.68 nm features a periodic modulation of polarization fields and topological charge density. The film furthermore exhibits an enhanced electromechanical response with an increased converse piezoelectric coefficient ( $d_{33}$ ) compared with SkX-free films. Transmission electron microscopy experiments in combination with phase-field simulations indicate that the dipole skyrmion texture results from the interference of two orthogonal single- $\mathbf{q}$  dipole patterns. We anticipate that the interference of multiple wavevectors may lead to a diversity of topological crystals with a variety of symmetries and lattice constants.

In magnetism, spins may form in nontrivial textures under specific condition of magnetic field and temperature<sup>1,2</sup>. For example, an ordered noncollinear and noncoplanar spin texture driven by Dzyaloshinskii–Moriya interaction (DMI) features a one-, two- or three-dimensional modulated arrangement of the spin topological domains<sup>3,4</sup>. Generally, an ordering state of a topological spin texture could be theoretically described by multiple- $\mathbf{q}$  mode, where  $\mathbf{q}$  is the wavevector of in-plane helices<sup>5,6</sup>. The nontrivial ordered topological spin states are thus expressed as the interference patterns by multiple helical spin density waves<sup>7</sup>, with the symmetry and properties of these topological

textures being influenced by the relative phase shifts of corresponding constituent helical waves<sup>7</sup>. The interference mode of spin density waves determines the topological spin textures, such as the single- $\mathbf{q}$  state (helical ordering<sup>8</sup>), double- $\mathbf{q}$  state (meron–antimeron lattice<sup>9</sup>) and triple- $\mathbf{q}$  state (hexagonal or triangular-like skyrmion lattice<sup>1,2</sup>), which are characterized by the coupled number of helical wavevectors<sup>6</sup>.

In contrast to ferromagnets, which have an asymmetry in electronic spin, ferroelectrics feature a non-centrosymmetric arrangement of the constituent ions, such as A or B cations (or both) off-centre relative to the oxygen anions in a perovskite structure<sup>10</sup>. The coupling

<sup>1</sup>Bay Area Center for Electron Microscopy, Songshan Lake Materials Laboratory, Dongguan, China. <sup>2</sup>Shenyang National Laboratory for Materials Science, Institute of Metal Research, Chinese Academy of Sciences, Shenyang, China. <sup>3</sup>Hunan University of Science and Technology, Xiangtan, China. <sup>4</sup>School of Materials Science and Engineering, University of Science and Technology of China, Shenyang, China. <sup>5</sup>Key Laboratory of Material Simulation Methods and Software of Ministry of Education, College of Physics, Jilin University, Changchun, China. <sup>6</sup>Department of Physics and Engineering, University of Scranton, Scranton, PA, USA. <sup>7</sup>Hebei Key Laboratory of Optic-electronic Information and Materials, The College of Physics Science and Technology, Hebei University, Baoding, China. <sup>8</sup>Institute of Physics, Chinese Academy of Sciences, Beijing, China. <sup>9</sup>Quantum Science Center of Guangdong-HongKong-Macau Greater Bay Area (Guangdong), Shenzhen, China. <sup>10</sup>These authors contributed equally: W. R. Geng, Y. L. Zhu, M. X. Zhu.

✉ e-mail: [xlma@iphy.ac.cn](mailto:xlma@iphy.ac.cn)

between the off-centre-induced polarization and spontaneous strain is generally substantial<sup>11–13</sup>. Consequently, the formation of topological dipole domains usually results in severe disclination strains<sup>11</sup>. Despite the fundamental difference between ferroelectric and ferromagnet, more and more complex topological structures, which were known earlier in ferromagnets, are found to have their counterparts in strained ferroelectric films such as flux-closure<sup>11</sup>, vortices<sup>14</sup>, skyrmion<sup>15</sup>, meron<sup>16</sup> and other polar topological states<sup>17–19</sup>.

The electric counterpart of magnetic DMI is proposed to describe an interaction between *i*- and *j*-site polar displacements in the form of  $D'_{ij} \cdot (u_i \times u_j)$ <sup>20,21</sup>, which might lead to the formation of noncollinear electric dipole patterns. Although electric DMI was demonstrated by first-principles simulations and group theoretical symmetry analysis<sup>20,21</sup>, so far electric dipole textures are limited to theoretical discussion<sup>22</sup> and experimental observations of incommensurate dipole helical ordering in BiMn<sub>7</sub>O<sub>12</sub> material<sup>23</sup> and the periodic vortices modulated by a second ordering with an incommensurate state in the SrRuO<sub>3</sub>/PbTiO<sub>3</sub>/SrRuO<sub>3</sub> system<sup>24</sup>. The spontaneous formation of the periodic polar skyrmion texture, which is analogous to the extensively studied DMI-driven magnetic counterpart, has not been observed so far in real materials.

In this paper, using aberration-corrected scanning transmission electron microscopy, we visualize that Néel-type skyrmion crystals (SkXs) are stabilized in the strained BiFeO<sub>3</sub> (BFO) ultrathin films grown on a LaAlO<sub>3</sub> (LAO) substrate, showing a periodic modulation of electric fields and topological charge density. Transmission electron microscopic (TEM) observation and phase-field simulations indicate that the as-received dipole skyrmion texture results from the electric DMI-driven interference of two perpendicular helical-like dipole patterns. Our findings show the ordered multiple-*q* mode of ferroelectric topological states, which would facilitate the nanoscale magnetoelectric coupling of topological states.

### Polar SkXs with double wavevectors

Using pulsed laser deposition technique, the ferroelectric BFO ultrathin films were fabricated on LAO (001) substrates (Fig. 1a,b), with a large lattice mismatch of about 4.36% between rhombohedral BFO and LAO substrates (Extended Data Table 1). The out-of-plane lattice constant of the BFO film is calculated as 0.463 nm according to the X-ray diffraction result in Fig. 1a, suggesting the tetragonally distorted BFO phase (*P4mm* symmetry)<sup>25</sup>. The roughness of the BFO film in Fig. 1c is calculated as about 120 pm. The dark-field (DF) TEM image (Fig. 1d) shows the prevailing dot-like contrast in the 8 nm BFO films in a manner of ordered distribution, which is further confirmed by the satellite spots around the basic reflections (Fig. 1e). The distance between satellite spots and the basic reflections remains constant with the magnitude of diffraction vector, eliminating the potential contributions of interfacial misfit dislocations on the spot splitting. The periodic dot-like contrast forms the square-like pattern, as shown in Fig. 1f, implying some polarization modulations in the BFO film. It is noted that the polarization in ferroelectric is accompanied with the local polarization field, which would be revealed by the differential phase-contrast (DPC) imaging<sup>26</sup>. In the DPC-STEM investigation (Fig. 1g–i), the regular distribution of polarization field fluctuation in the BFO thin film is detected.

The periodic modulation in Fig. 2a is reflected by the satellite spots in the fast Fourier transformation (FFT) pattern (Extended Data Fig. 1a,f) along the [110] and  $[\bar{1}10]$  directions, which could be described as the two-directional reciprocal-space vectors of  $q_1$  and  $q_2$ . Thus, the regular lattice modulation is expected to induce the polarization patterns as the double-*q* ordered state considering the strong coupling between polarization and strain in ferroelectrics<sup>12,13</sup>. According to Fig. 2a, the atomic positions and thereby the reversed Fe-ionic displacement ( $-\delta_{Fe}$ ) vector map could be determined<sup>27</sup>, further supported by Supplementary Figs. 1 and 2. The  $-\delta_{Fe}$  vector map (Fig. 2b) shows the periodic distribution of the centre-convergent domains (red circles),

forming the ordered topological lattices, with the lattice constant being calculated as  $2.68 \pm 0.15$  nm by measuring the centre distance between neighbouring centre-convergent domains at multiple locations in Fig. 2b. One topological unit cell is constituted by four centre-convergent domains (Fig. 2c). Within one centre-convergent domains, the maximum in-plane polarization is observed at the domain periphery, whereas the minimum is at their cores in Fig. 2c, suggesting larger out-of-plane polarizations at the cores. The periodic topological lattices are also confirmed by the strain superstructures in Fig. 2d corresponding to Supplementary Fig. 3, where the grid-like strain state is shown. The detailed strain states are also revealed in Extended Data Fig. 1b–e,g–j. In addition, the cross-sectional TEM sample of the BFO film shows the alternative out-of-plane polarization modulation (Fig. 2e,f). As a result, the three-dimensional polarization configuration of the centre-convergent domains (skyrmion structure) is depicted in Fig. 2g, revealed as polar Néel-type skyrmions. Thereby, the SkX is stabilized in BFO films.

For the formation reasons of the SkX, three factors should be considered. First, the in-plane polarization distribution of SkX is an effective way for relaxing the isotropic misfit strain, given the strong coupling between spontaneous polarization and strain in ferroelectrics<sup>12</sup>. Second, the alternative out-of-plane polarization of the skyrmions is expected to decrease the large depolarization field in BFO ultrathin films. The polarization rotation in the periodic SkX is accompanied by the ferroelastic strain in the BFO films, which is revealed by the atomic force microscopy imaging in Supplementary Figs. 4 and 5. Finally, the eDMI is also crucial for the formation of SkX, which will be discussed later based on the results of phase-field simulation. It is further confirmed that the film thicknesses (Supplementary Figs. 6–18) and misfit strains (Supplementary Figs. 19–25) also influence the polarization distribution of BFO films, as discussed in Supplementary Note 1. In addition, the polar SkX is accompanied with the periodic oxygen octahedral distortion (Extended Data Fig. 2), suggesting the potential interactions between off-centre-induced polarization and oxygen octahedral distortion.

### Polar topological ordering with single wavevector

As mentioned above, the two-dimensional (2D) lattice modulation results in the square-like SkXs, defined as the double-*q* spin ordering. By analogy, the reduced dimensionality of the lattice modulation would generate different topological patterns. In BFO films, both the 2D and one-dimensional (1D) lattice modulations are simultaneously obtained induced by inhomogeneous strain relaxation owing to potential growth defects<sup>12,28</sup>. The obtained 1D lattice modulation is revealed by multiple imaging modes in TEM (Fig. 3a). As shown in Fig. 3b,c, the Bi and Fe atomic columns are clearly resolved. Evident structural modulation is revealed by the superstructure spots in Fig. 3d and inset in Fig. 3e, suggesting the existence of 1D lattice modulation. The period of the lattice modulation is determined to be about 2.2 nm (inset in Fig. 3e and Extended Data Fig. 3). In addition, the 1D lattice modulation is accompanied with the stripe-like strain state (Supplementary Figs. 26–28). The polarization for the single-*q* dipole ordering is determined as tail-to-tail and head-to-head charged domain wall patterns (Fig. 3f and Supplementary Fig. 29), further schematized in Fig. 3g. The polarization directions at neighbouring domains are not exactly antiparallel but with slight angle, which would reduce the large electrostatic energy at charged domain walls rather than the slight misorientation from the zone axis (confirmed in Supplementary Fig. 30). The polarization distribution profile along the cyan arrow in Fig. 3f shows the periodic displacement modulation (Extended Data Fig. 4). The absolute magnitudes of the  $\delta_{Fe}$  reach the minimum value at the tail-to-tail charged domain walls, implying the potential vortex tubes of the single-*q* dipole ordering (Extended Data Fig. 5 and Supplementary Fig. 31). In addition, regular electric field modulation is also induced by the 1D-ordered polarization patterns (Fig. 3h), which is consistent with the A-site structural modulation

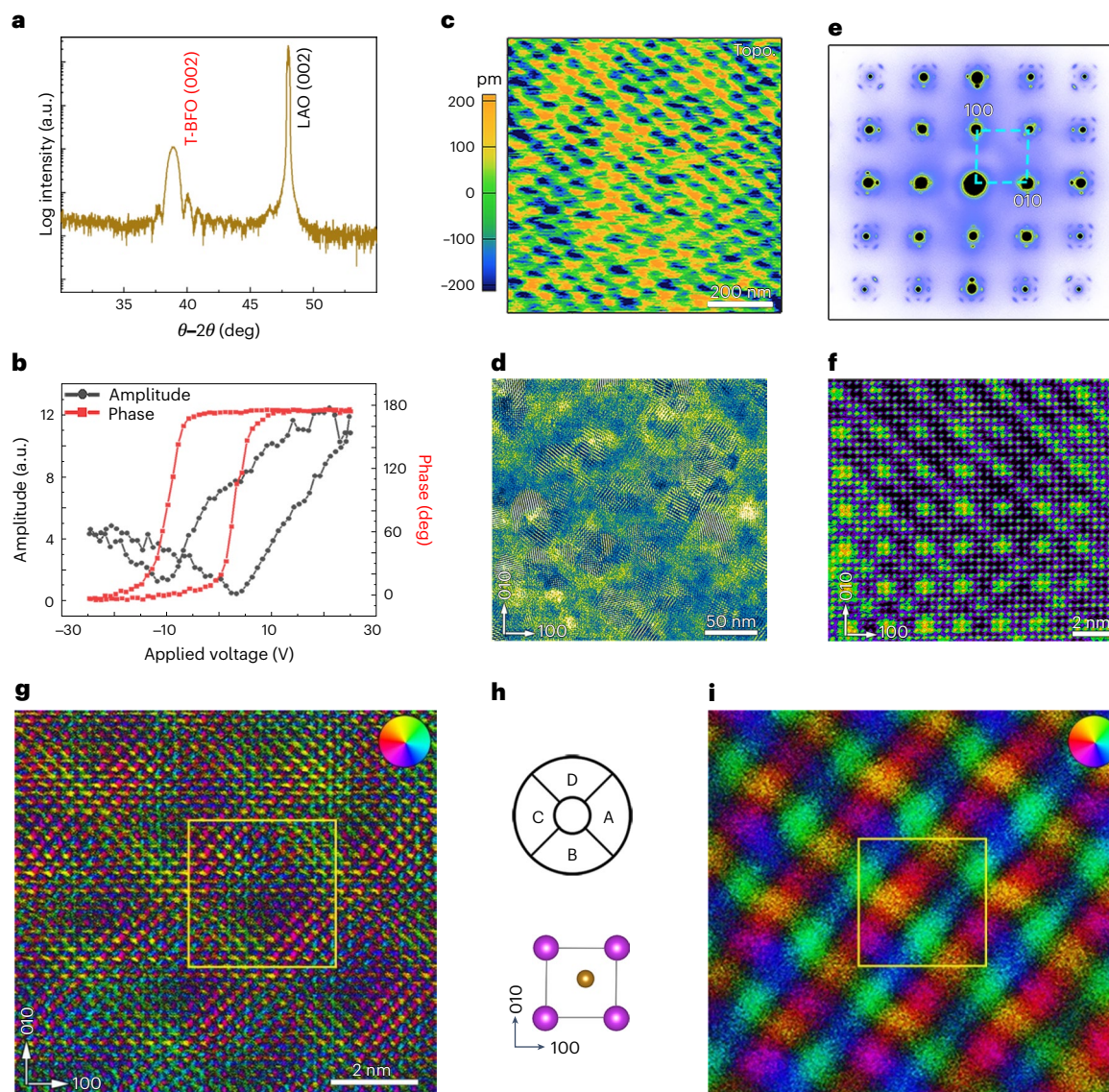


**Fig. 1 | Experimental observation of the periodic 2D modulated patterns in the BFO film grown on a LAO (001) substrate.** **a**, High-resolution X-ray  $2\theta$ - $\omega$  scan showing the pseudocubic 002 peaks of the BFO/LAO (001) film, with the surrounding thickness fringes indicating the smooth surface of the BFO films. **b**, Local piezoresponse phase and amplitude hysteresis loops of the BFO film. **c**, Topography image (Topo.) of the  $830 \times 830 \text{ nm}^2$  region in the BFO film. **d**, DF TEM image of the BFO film showing the periodic distribution of dot-like contrast. **e**, Selected area electron diffraction pattern of the BFO film along the [001] zone axis. **f**, Under-focused atomic-resolved high-angle annular dark-field scanning

TEM (HAADF-STEM) image of the BFO film, showing the dot-like contrast. **g**, Atomic-resolved electric vector colour map of the 2D modulated patterns. **h**, Sketch of the sample orientation with respect to the segmented detector, with the [100] and [010] directions of the BFO unit cells being parallel to the A–C and B–D segments of the detectors, respectively. **i**, Under-focused electric vector colour map showing the grid-like periodic 2D modulation patterns. The inset colour wheels in **g** and **i** represent the vector direction and magnitude by the colour and brightness, respectively. The rectangles in **g** and **i** highlight one modulation period.

in Fig. 3b,e and the oxygen octahedral distortion in Extended Data Fig. 6, excluding the systematic errors during DPC-STEM imaging<sup>29</sup>. As a result, the helical-like dipole ordering is obtained in BFO films. The evident oxygen octahedral distortion and slight polarization rotation in the neighbouring domains hint the potential electric DMI<sup>20,23</sup> in the BFO ultrathin films.

### Dipolar wavevector interference

As discussed above, the periodic polarization modulations with double and single reciprocal vectors are obtained in BFO films, which could be defined as double- $q$  polar ordering and single- $q$  polar ordering, respectively. It is expected that the double- $q$  SkXs could be characterized by the superposition of two perpendicular single- $q$  dipole orderings (Fig. 4a–g and Supplementary Fig. 32). As seen in Fig. 4a,b, two

orthogonal 1D-ordered dipole patterns have different reciprocal-space vectors in the FFT patterns (insets in Fig. 4a). The polarizations of the intersections (white dots in Fig. 4a) are determined to be the centre-convergent domains (Fig. 4b). As a result, the interplay of two perpendicular single- $q$  dipole orderings constitutes the 2D ordered patterns, as shown in Fig. 4c–g. In other words, the 2D ordered patterns could be decomposed as the two intersected perpendicular single- $q$  dipole orderings, as schematized in Fig. 4e.

Electron beam irradiation in TEM is a powerful tool to regulate the structure and physical properties of TEM samples based on the mechanisms of heating effect and charging process<sup>30–32</sup>. To investigate the potential transition of the topological states, the in situ experiments under electron beam irradiation were performed. The time-dependent images in Fig. 4h–m show the transition process between different

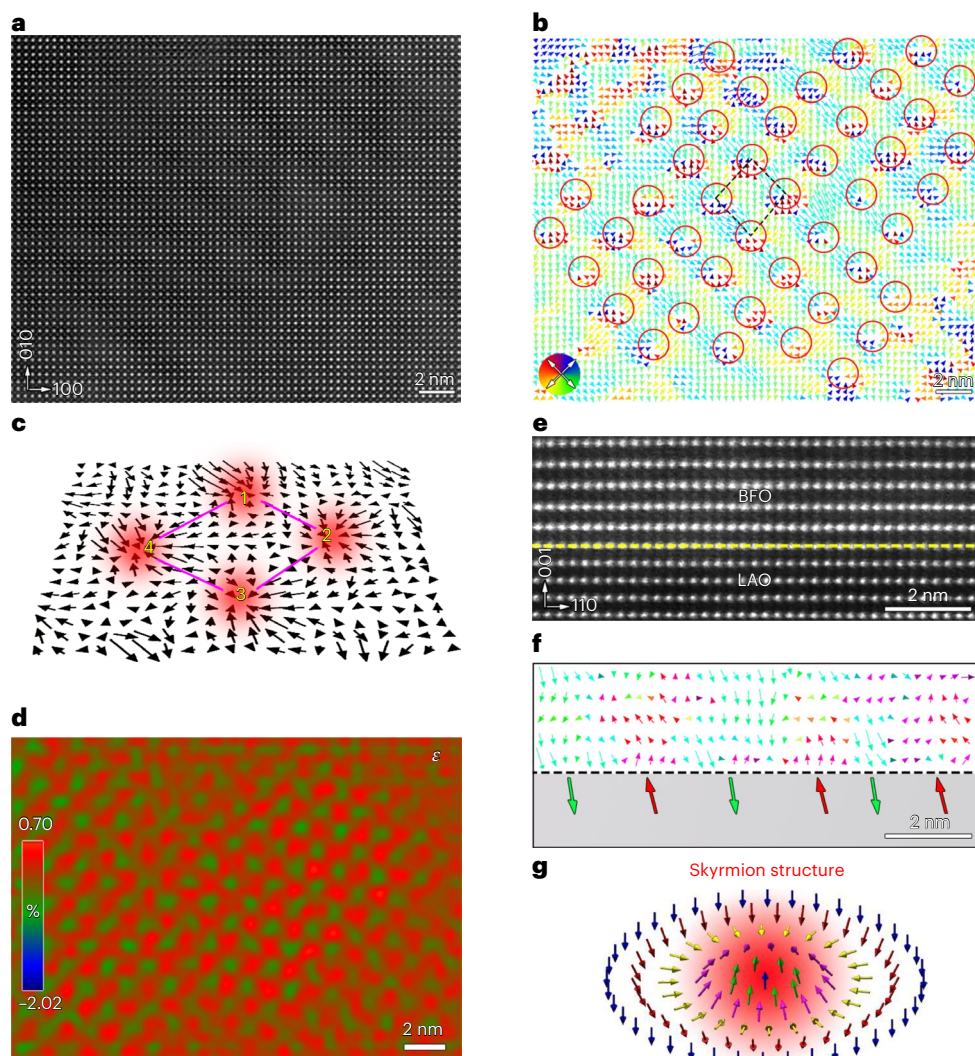


**Fig. 2 | Experimental polarization distribution of the periodic topological lattices in BFO films.** **a**, Atomic-resolved HAADF-STEM image of the planar-view TEM sample with the 2D modulation patterns. **b**, Corresponding  $-\delta_{\text{Fe}}$  vector map of **a**. The rectangle in **b** defines a unit cell of the topological lattice. **c**, Schematic of the polarization distribution for one topological unit cell constituted by four centre-convergent domains. **d**, Averaged strain distribution ( $\epsilon$ ) map derived from

geometric phase analysis, showing the 2D grid-like strain distribution. **e**, Cross-sectional atomic-resolved HAADF-STEM image viewed along the  $[1\bar{1}0]$  direction of the BFO film. **f**, Corresponding  $-\delta_{\text{Fe}}$  vector map of **e** and the schematic illustration of polarization distribution. **g**, Reconstructed schematic of the polarization distribution for the centre-convergent domain (Skyrmion structure).

multiple- $\mathbf{q}$  dipole orderings under the electron beam irradiation. As seen in Fig. 4h, the stripy dipole pattern is dominant in the initial domain state. After 3 min of the electron beam irradiation, the dipole textures first maintained robust as the 1D stripe-like domains (Fig. 4i). On increasing the irradiation time, some skyrmions tend to appear, as the helical-like stripes are fragmented (Fig. 4j). Finally, the stripe-like domains are completely replaced by the 2D-ordered skyrmions, namely the SkX (Fig. 4k). The above transformation is also confirmed by the Bragg reflections in FFT images. The FFT image corresponding to the initial state shows the one-directional Bragg reflections,  $\mathbf{q}_1$  (Fig. 4l), confirming the 1D-ordered dipole texture. By contrast, the FFT image corresponding to the SkX state features two reciprocal vectors,  $\mathbf{q}_1$  and  $\mathbf{q}_2$  (Fig. 4m). Each of the two mutually orthogonal vectors corresponds to a single helical-like dipole state. It is proposed that the 2D SkX dipole state could be represented as the interference pattern of two helical-like dipole states.

On the basis of the interferometric displacement sensor<sup>33</sup>, local butterfly loops of the BFO films with varying thicknesses are measured to reveal the piezoresponse behaviours of the ordered topological

states. As shown in Fig. 4n and Supplementary Fig. 33, the representative piezoresponse amplitude loops for a series of BFO films are shown. When the BFO film thickness ranges from 1.6 nm to 10.4 nm, the domain patterns change from diffused topological domains (DTD), SkX, to strike-like domains (SLD), as shown in Supplementary Figs. 8–18. The values of  $d_{33}$  in different BFO films are shown in Fig. 4o. In contrast to the strong dependence of  $d_{33}$  on film thickness reported in ferroelectric BaTiO<sub>3</sub> films<sup>34</sup>, the  $d_{33}$  for the films (8 nm and 8.8 nm) with double- $\mathbf{q}$  ordered SkX features maximum, as highlighted by the red mask in Fig. 4o. The  $d_{33}$  reaches 9.03 pm V<sup>-1</sup> at 8.8 nm, which is higher than that of 10.4 nm (about 7.24 pm V<sup>-1</sup>). As a result, the BFO films with SkX exhibit an enhanced electromechanical response compared with the SkX-free BFO films.

### Phase-field simulations

To rationalize the experimental observations of the single- $\mathbf{q}$  states and the double- $\mathbf{q}$  SkX driven by the eDMI at the ultrathin BFO films, phase-field simulations are further performed. As reported previously<sup>20</sup>, there exists a one-to-one correspondence between magnetic DMI and

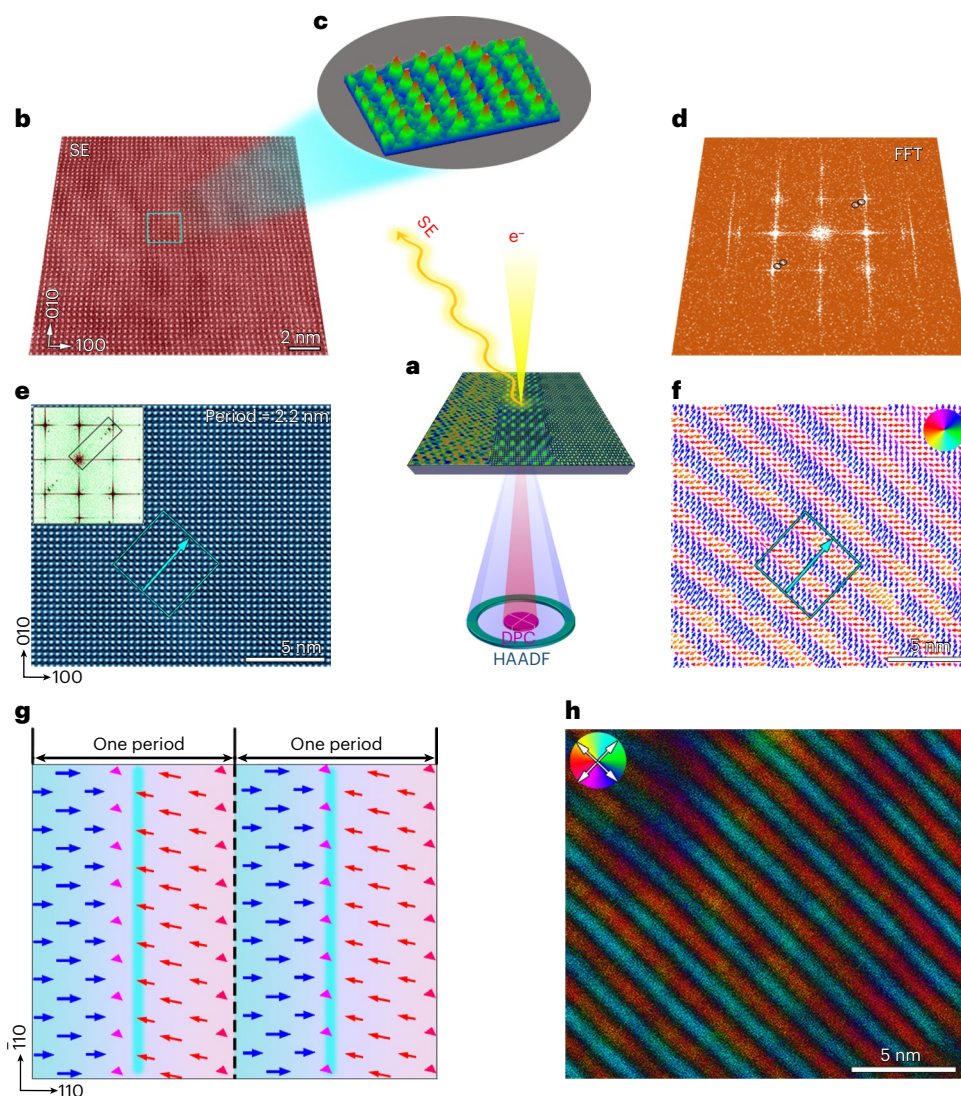


**Fig. 3 | Experimental polarization distribution of the single- $q$  topological state in BFO films.** **a**, Schematic of the SE, HAADF and DPC-STEM imaging under the STEM mode. **b**, Atomic-resolved SE imaging of BFO films. **c**, Three-dimensional diagram of the enlarged cyan rectangle in **b**, showing the distribution of atomic columns. **d**, Corresponding FFT image of **b** with superstructure spots highlighted by black circles. **e**, Atomic-resolved planar-view HAADF-STEM images of the 1D modulation fringes with the period of 2.2 nm. Inset: corresponding FFT

pattern showing the superstructure spots. **f**, Corresponding  $-\delta_{\text{Fe}}$  vector map. **g**, Schematic illustration of the charged domain walls induced by 1D structural modulation, corresponding to the rectangle in **f**. Solid and broken lines in **g** denote the head-to-head and tail-to-tail charged domain walls, respectively. **h**, Under-focused DPC-STEM image showing the periodic electric field modulation of the single- $q$  ordering.

electric DMI, whereby Néel- and Bloch-type electric skyrmions are described by the terms given by  $D_N[\mathbf{u}_z(\nabla \cdot \mathbf{u}) - (\mathbf{u} \cdot \nabla)\mathbf{u}_z]$  and  $D_B\mathbf{u} \cdot (\nabla \times \mathbf{u})$  (with  $\mathbf{u}$  and  $\mathbf{u}_z$  being the displacement vector and its  $z$  component), respectively. In our simulation, the displacement field  $\mathbf{u}$  is represented by the polarization order parameter  $\mathbf{P}$ , while the strengths of the Néel- and Bloch-type interactions are modulated by the coefficients  $D_N$  and  $D_B$ , respectively (see Methods for detailed implementation). Two initial structures are designed, as depicted in Supplementary Fig. 34, featuring stripe domains that collide and merge orthogonally to form a lattice through the interference of single- $q$  states and a fully constructed lattice, respectively. Owing to the lack of documented values for the eDMI coefficients in the continuous model, we incrementally increase the  $D_N$  and  $D_B$  values until the simulated polar states matched the experimental observations (see Supplementary Note 2 for details). As illustrated in Fig. 5a,c, a  $D_N$  value of  $2.71 \text{ C}^{-2} \text{ m}^3 \text{ N}$  allows both initial structures to form SkX with the skyrmion diameters of approximately 2 nm, aligning closely with experimental

observations (Fig. 4) (see Supplementary Note 2 and Supplementary Figs. 35 and 36 for other  $D_N$  and  $D_B$  values). The periodic SkX (Fig. 5c) resembles the skyrmion lattice found in ferromagnetic materials<sup>3</sup>. The stabilization of SkX at the ends of vortex tubes, as observed in the experimental findings in Fig. 4a,b, suggests that the SkX may originate from the superposition of vortex tubes, underscoring the critical role of eDMI in stabilizing multiple- $q$  dipole states. In BFO, the formation of eDMI can be explained through the following microscopic aspects: first, in ferroelectric materials, the microscopic origin of eDMI primarily arises from the breaking of local symmetry, leading to antisymmetric exchange interactions<sup>20</sup>. Specifically, the hybridization between the 6s lone pair electrons of Bi ions and the  $2p$  orbitals of O ions in BFO undergoes distortions along the body diagonal direction owing to constraints imposed by crystal symmetry<sup>35</sup>. These distortions result in trilinear coupling, which involves the displacement of two adjacent Bi (or Fe) ions and the intermediate oxygen ion (Supplementary Fig. 37), giving rise to an indirect interaction similar to that observed between

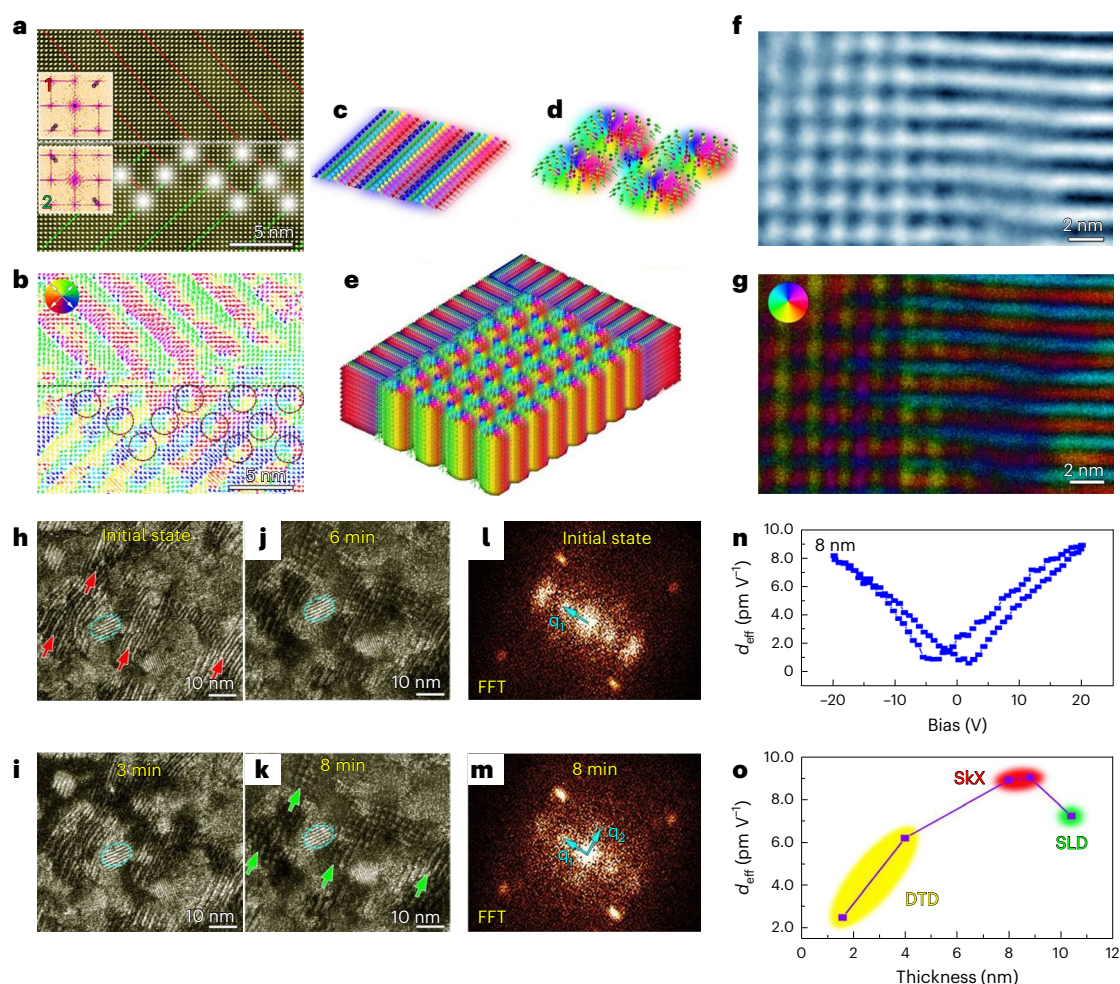


**Fig. 4 | The double- $q$  topological lattice resultant from the intersection of two single- $q$  topological dipole orderings.** **a**, Atomic-resolved HAADF-STEM image of the planar-view TEM sample, showing the twin boundary derived from the intersection of two perpendicular 1D modulation fringes. The white dots denote the intersections. Insets: FFT patterns of the two 1D modulation fringes numbered with 1 and 2 in **a**. **b**, Corresponding  $-\delta_{\text{Fe}}$  vector map of **a**, showing the centre-convergent domains at the crosses. **c, d**, Magnified 1D modulation pattern (**c**) and skyrmion unit cell (**d**). **e**, Schematic illustration showing the formation of 2D SkX derived from the interaction of 1D modulation patterns. **f, g**, Under-focused iDPC-STEM (**f**) and DPC-STEM (**g**) maps, showing the formation of 2D modulation patterns derived from the intersection of two 1D modulation patterns. The colour wheel in **g** represents the vector direction and

magnitude of local electric field by the colour and brightness, respectively. **h–k**, A series of DF TEM images showing the process of the topological phase transition from 1D modulation patterns to 2D modulation patterns under electron beam irradiation, which is highlighted by the red and green arrows. The irradiation time is increased from 0 min thereby the initial state (**h**), 3 min (**i**), 6 min (**j**) to 8 min (**k**). Note that all the DF TEM images were acquired in the same region as referenced with the cyan ellipses. **l, m**, FFT images of the DF TEM images in **h** and **k**, respectively, showing the transformation from single- $q$  dipole wavevector to double- $q$  dipole wavevector. **n**, Quantitative measurements of effective  $d_{33}$  for BFO films being 8 nm. **o**, Effective  $d_{33}$  versus BFO film thickness, where the DTD, SkX and SLD denote the diffused topological domains, skyrmion crystal and strike-like domains in different thicknesses, respectively.

nearest-neighbour Pb sites mediated by the displaced intermediate oxygen ion in  $\text{PbTiO}_3$  (ref. 36). In addition, when the BFO film is subjected to epitaxial strain exceeding  $-4.4\%$  (for example, on a LAO substrate), it transforms from a rhombohedral to a distorted tetragonal phase. The phase transformation induces evident displacements of Fe ions along the  $[001]$  direction relative to the O ions<sup>37</sup>, thereby amplifying ferroelectric polarization and increasing local inversion symmetry breaking. All the aforementioned factors collectively establish favourable conditions for eDMI.

To gain further insight into the stabilized topological states, in-depth views of the polarization distribution for the marked region in Fig. 5a and Fig. 5c are presented in Fig. 5b and Fig. 5d, respectively. At the boundary between the vortex tubes and the SkX, there emerge ‘half-skyrmion’-like structures comprised of a half downward-converging skyrmion and 1D-ordered dipole state, as highlighted by the red dashed circle. The magnified polarization configuration of a single skyrmion in Fig. 5d reveals that the polarization involved

in a radially symmetric skyrmion rotates from upward-pointing to downward-pointing through the in-plane component. To further understand the topological nature of the polar texture, Fig. 5e shows the planar distribution of polarization within the marked region in Fig. 5c, and the corresponding distribution of topological charge density is presented in Fig. 5f. Regions with downward-converging polarization exhibit the negative topological charge density, while those with upward-diverging polarization show the positive topological charge density, yielding a topological charge of  $-1$  for a single skyrmion.

In addition, we have systematically studied the effects of the film thickness and the misfit strain on the formation of multiple- $q$  dipole states while maintaining  $D_{\text{N}} = 2.71 \text{ C}^{-2} \text{ m}^3 \text{ N}$ . Our findings indicate that when the film thickness is in the range of 4–6 nm, the SkX is stabilized (Supplementary Fig. 38). This can be explained from an energy perspective. As shown in Supplementary Fig. 39, the eDMI energy density, which varies with the film thickness, reaches a relative minimum within 4–6 nm, thereby stabilizing the SkX. At other thicknesses, the eDMI

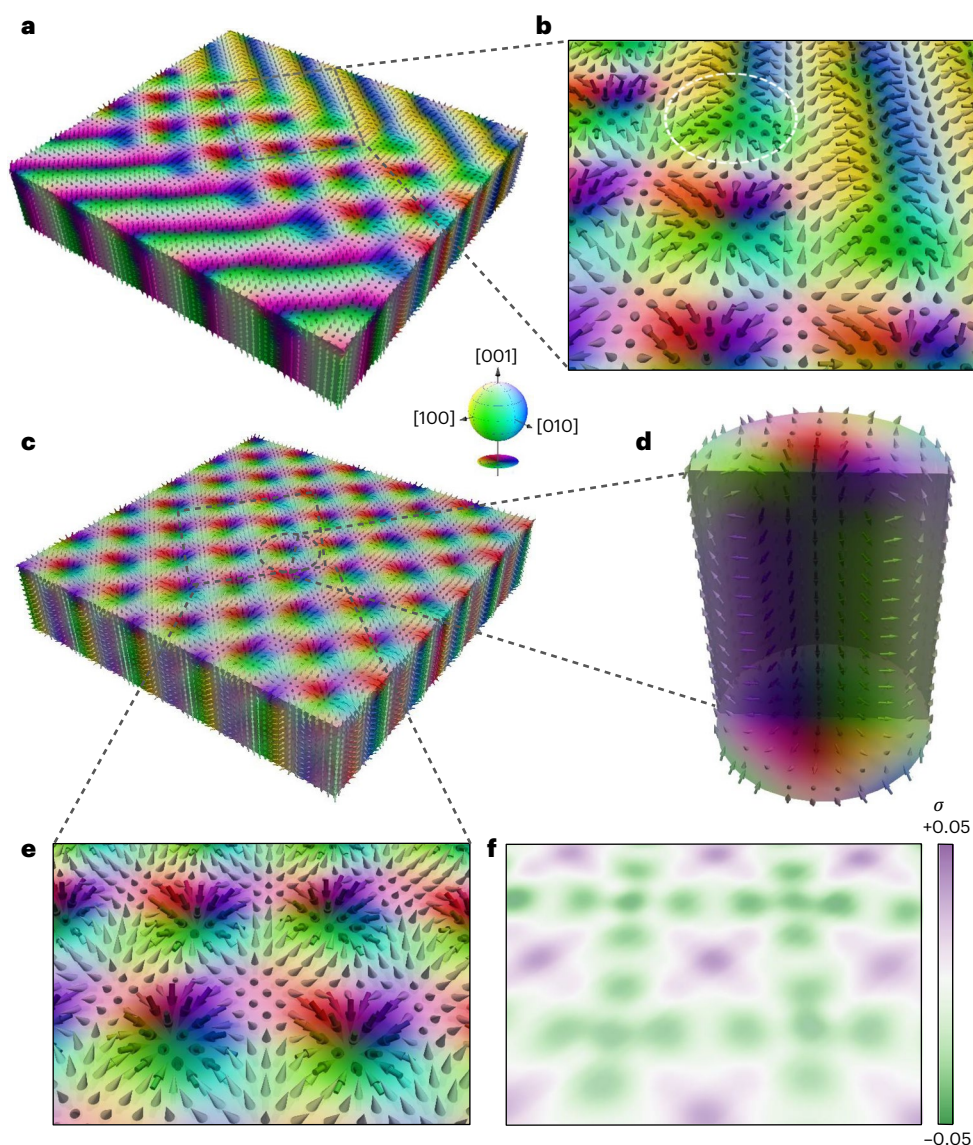


**Fig. 5 | The single- $q$  and double- $q$  topological polar orderings derived from phase-field simulations. a**, Relaxed polarization configuration formed by two intersecting single- $q$  states with 50% overlap. **b**, Planar polarization distribution at the interface between the single- $q$  polar ordering and the double- $q$  topological lattice configuration. **c**, Detailed three-dimensional polarization arrangement within the double- $q$  lattice model. **d**, Specific depiction of the polarization structure of an individual skyrmion in the lattice. **e**, Planar view of

the polarization distribution within the highlighted region of the lattice model. **f**, Corresponding topological charge density map of **e**, with the colour bar indicating the topological charge density in units of  $1 \text{ nm}^{-2}$ . The colours in the three-dimensional depiction indicate in-plane polarization angles with white for polarization pointing upwards and dark for polarization pointing downwards in the out-of-plane direction, as shown in the HSV colour sphere.

driving force is insufficient to stabilize the lattice. Besides, simulations under different misfit strains indicate that smaller compressive strain destroys the SkX (Supplementary Fig. 40), supporting the experimental findings (Supplementary Figs. 19–25). In addition, we compute the polarization evolution of random initial configurations under varying eDMI strengths in Supplementary Figs. 41 and 42. In the absence of eDMI, the open circuit condition leads to the formation of a single- $q$  state (Supplementary Fig. 41), while the short circuit condition yields trivial domains (Supplementary Fig. 42). Notably, at  $D_N = 2.71 \text{ C}^{-2} \text{ m}^3 \text{ N}$ , where the SkX can be stabilized from an initial lattice model set-up, the density of skyrmions increases while their diameters decrease, approaching those in the lattice model in the open circuit condition, and the short circuit condition also results in the formation of skyrmions, thereby affirming the pivotal role of eDMI in the SkX formation. The results from the random model under different thickness and strain conditions are consistent with the results from

the lattice model (Supplementary Figs. 43 and 44). Furthermore, we have calculated the effect of flexoelectricity on the random model. As shown in Supplementary Fig. 45, the polarization distribution does not change under various flexoelectric conditions, except for a subtle increase in polarization magnitude.

## Conclusion

We have observed emergent skyrmion lattice with double- $q$  dipole orderings that feature an enhanced electromechanical response behaviour in ferroelectric films. The regular Néel-type SkX, described as the double- $q$  dipole state, is stabilized in BFO multiferroic films with periodic modulation of polarization field and topological charge density. TEM imaging and phase-field simulations indicate that the double- $q$  SkX in the ferroelectric films is derived from the interplay of two orthogonal single- $q$  dipole patterns, which provides the direct experimental and theoretical evidences in interpreting the formation of SkX.

This work provides a new perspective for ferroelectric topology. The reported double- $q$  SkXs are expected to be accompanied with nontrivial magnetoelectric coupling considering the multiferroic nature<sup>38</sup> of BFO. However, the appearance of only single square-like superstructure in this work is limited by the symmetry of the film structure and lattice mismatch between films and substrates. More broadly, by engineering other ferroelectric films under special mismatch strain, the interference of multiple dipole wavevectors is expected to generate a diversity of polar topological crystals with a variety of symmetries and lattice constants in the future experiments. In addition, the enhanced electromechanical response for the BFO films with SkXs hints that many other dipolar topological orderings are about to be discovered with rich physical properties.

## Online content

Any methods, additional references, Nature Portfolio reporting summaries, source data, extended data, supplementary information, acknowledgements, peer review information; details of author contributions and competing interests; and statements of data and code availability are available at <https://doi.org/10.1038/s41565-024-01845-5>.

## References

- Muhlbauer, S. et al. Skyrmion lattice in a chiral magnet. *Science* **323**, 915–919 (2009).
- Yu, X. Z. et al. Near room-temperature formation of a skyrmion crystal in thin-films of the helimagnet FeGe. *Nat. Mater.* **10**, 106–109 (2011).
- Yu, X. Z. et al. Real-space observation of a two-dimensional skyrmion crystal. *Nature* **465**, 901–904 (2010).
- Leonov, A. O. & Mostovoy, M. Multiply periodic states and isolated skyrmions in an anisotropic frustrated magnet. *Nat. Commun.* **6**, 8275 (2015).
- Takagi, R. et al. Multiple- $q$  noncollinear magnetism in an itinerant hexagonal magnet. *Sci. Adv.* **4**, eaau3402 (2018).
- Spethmann, J. et al. Discovery of magnetic single- and triple- $q$  states in Mn/Re(OO01). *Phys. Rev. Lett.* **124**, 227203 (2020).
- Hayami, S. et al. Phase shift in skyrmion crystals. *Nat. Commun.* **12**, 6927 (2020).
- Uchida, M., Onose, Y., Matsui, Y. & Tokura, Y. Real-space observation of helical spin order. *Science* **311**, 359–361 (2006).
- Yu, X. Z. et al. Transformation between meron and skyrmion topological spin textures in a chiral magnet. *Nature* **564**, 95–98 (2018).
- Jia, C. L. et al. Direct observation of continuous electric dipole rotation in flux-closure domains in ferroelectric Pb(Zr,Ti)O<sub>3</sub>. *Science* **331**, 1420–1423 (2011).
- Tang, Y. L. et al. Observation of a periodic array of flux-closure quadrants in strained ferroelectric PbTiO<sub>3</sub> films. *Science* **348**, 547–551 (2015).
- Geng, W. et al. Atomic-scale tunable flexoelectric couplings in oxide multiferroics. *Nano Lett.* **21**, 9601–9608 (2021).
- Tang, Y. L. et al. Giant linear strain gradient with extremely low elastic energy in a perovskite nanostructure array. *Nat. Commun.* **8**, 15994 (2017).
- Yadav, A. K. et al. Observation of polar vortices in oxide superlattices. *Nature* **530**, 198–201 (2016).
- Das, S. et al. Observation of room-temperature polar skyrmions. *Nature* **568**, 368–372 (2019).
- Wang, Y. J. et al. Polar meron lattice in strained oxide ferroelectrics. *Nat. Mater.* **19**, 881–886 (2020).
- Gong, F. H. et al. Atomic mapping of periodic dipole waves in ferroelectric oxide. *Sci. Adv.* **7**, eabg5503 (2021).
- Govinden, V. et al. Ferroelectric solitons crafted in epitaxial bismuth ferrite superlattices. *Nat. Commun.* **14**, 4178 (2023).
- Govinden, V. et al. Spherical ferroelectric solitons. *Nat. Mater.* **22**, 553–561 (2023).
- Zhao, H. J. et al. Dzyaloshinskii–Moriya-like interaction in ferroelectrics and antiferroelectrics. *Nat. Mater.* **20**, 341–345 (2021).
- Yu, L. et al. The anti-symmetric and anisotropic symmetric exchange interactions between electric dipoles in hafnia. *Nat. Commun.* **14**, 8127 (2023).
- Yuan, S. et al. Hexagonal close-packed polar-skyrmion lattice in ultrathin ferroelectric PbTiO<sub>3</sub> films. *Phys. Rev. Lett.* **130**, 226801 (2023).
- Khalyavin, D. D. et al. Emergent helical texture of electric dipoles. *Science* **369**, 680–684 (2020).
- Rusu, D. et al. Ferroelectric incommensurate spin crystals. *Nature* **602**, 240–244 (2022).
- Zeches, R. J. et al. A strain-driven morphotropic phase boundary in BiFeO<sub>3</sub>. *Science* **326**, 977–980 (2009).
- Shibata, N. et al. Differential phase-contrast microscopy at atomic resolution. *Nat. Phys.* **8**, 611–615 (2012).
- Anthony, S. M. & Granick, S. Image analysis with rapid and accurate two-dimensional Gaussian fitting. *Langmuir* **25**, 8152–8160 (2009).
- Liu, Z. et al. In-plane charged domain walls with memristive behaviour in a ferroelectric film. *Nature* **613**, 656–661 (2023).
- Strauch, A. et al. Systematic errors of electric field measurements in ferroelectrics by unit cell averaged momentum transfers in STEM. *Microsc. Microanal.* **29**, 499–511 (2023).
- Chen, Z. et al. Manipulation of nanoscale domain switching using an electron beam with omnidirectional electric field distribution. *Phys. Rev. Lett.* **117**, 027601 (2016).
- Guo, S. et al. Mending cracks atom-by-atom in rutile TiO<sub>2</sub> with electron beam radiolysis. *Nat. Commun.* **14**, 6005 (2023).
- Wei, J. et al. Direct imaging of atomistic grain boundary migration. *Nat. Mater.* **20**, 951–955 (2021).
- Labuda, A. & Proksch, R. Quantitative measurements of electromechanical response with a combined optical beam and interferometric atomic force microscope. *Appl. Phys. Lett.* **106**, 253103 (2015).
- Kelley, K. et al. Thickness and strain dependence of piezoelectric coefficient in BaTiO<sub>3</sub> thin films. *Phys. Rev. Mater.* **4**, 024407 (2020).
- Wang, J. et al. Epitaxial BiFeO<sub>3</sub> multiferroic thin film heterostructures. *Science* **299**, 1719–1722 (2003).
- Chen, P. et al. Microscopic origin of the electric Dzyaloshinskii–Moriya interaction. *Phys. Rev. B* **106**, 224101 (2022).
- Zhang, J. X. et al. Microscopic origin of the giant ferroelectric polarization in tetragonal-like BiFeO<sub>3</sub>. *Phys. Rev. Lett.* **107**, 147602 (2011).
- Geng, W. R. et al. Magneto-electric-optical coupling in multiferroic BiFeO<sub>3</sub>-based films. *Adv. Mater.* **34**, e2106396 (2022).

**Publisher's note** Springer Nature remains neutral with regard to jurisdictional claims in published maps and institutional affiliations.

Springer Nature or its licensor (e.g. a society or other partner) holds exclusive rights to this article under a publishing agreement with the author(s) or other rightsholder(s); author self-archiving of the accepted manuscript version of this article is solely governed by the terms of such publishing agreement and applicable law.

© The Author(s), under exclusive licence to Springer Nature Limited 2025

## Methods

### Film deposition details

A series of epitaxial BFO ultrathin films were grown on [001]-oriented LAO substrates using pulsed laser deposition with a Coherent Compex PRO 201 F KrF ( $\lambda = 248$  nm) excimer laser. The [001]-oriented LAO commercial substrates were used without extra chemical or heat treatment. Before deposition, the substrates were heated to 850 °C for 20 min to clean the substrate surfaces and then cooled to the film deposition temperature at a rate of 5 °C min<sup>-1</sup>. The 1 mol% Bi-enriched BFO target was used to deposit the BFO films, which was pre-sputtered for 20 min to get the fresh surface. When growing the BFO films, these growth parameters were used, including a deposition rate of 6 Hz, a substrate temperature of 800 °C, an oxygen partial pressure of 90 mTorr and a laser energy of 370 mJ. After deposition, these films first remained temperature at 800 °C for 20 min, then cooled to 200 °C at a rate of -5 °C min<sup>-1</sup> and finally cooled naturally to room temperature in an oxygen partial pressure of 200 Torr.

### TEM sample preparation and TEM observation

The TEM samples were prepared and observed using the methods previously reported<sup>38</sup>. The cross-sectional samples for STEM observation were prepared by traditional processes: slicing, gluing, grinding, dimpling and finally ion milling. A Gatan 691 PIPS was used for ion milling. During the ion milling process, a low angle (5°) and a cooling stage were used first, and the final ion milling voltage was 0.3 eV for 10 min to reduce the beam damage. The DF TEM images were recorded using a conventional TEM (JEM-F200 (JEOL) working at 200 kV). High-angle annular dark-field (HAADF) STEM images were recorded using an aberration-corrected (scanning) transmission electron microscope (ThermoFisher Spectra 300 equipped with a double Cs corrector from CEOS and operated at 300 kV). DPC-STEM and iDPC-STEM imaging were performed with a convergence angle of 25 mrad and a Panther detector.

### SE-STEM imaging

The secondary electron (SE)-STEM experiments were carried out in the JEM-ARM300F2 equipped with a high-brightness cold field-emission gun, a probe corrector (dodeca-pole ETA corrector) using the software of JEOL COSMO and a high-efficiency SE detector situated above the upper pole-piece, operated at 300 kV. The facility allows to record the annual dark-field (ADF), bright-field (BF) and SE images spontaneously under the STEM mode. By using the probe aberration corrector, it can get a resolution of about 60 pm in ADF-STEM images and a resolution of below 1 Å in SE-STEM images.

### STEM result analyses

The analyses of the STEM results were performed using the methods previously reported<sup>38</sup>. Strain analyses were based on geometric phase analysis<sup>39</sup> using Gatan GMS3 software. Atom positions were accurately determined using 2D Gaussian peak fitting in Matlab<sup>27</sup>, aiming to get the information of the B-site ionic displacement and A-site ionic in-plane rotation. A Wiener filter of HAADF and a low-pass annular mask restricted to the instrument resolution limit of the images were used to reduce the noise of the obtained images. The drift-corrected frame integration function was used in Velox software to create a single image by aligning and combining the individual frames in an acquired series, aiming to reduce the shifts and instabilities and improve the image contrast.

### Piezoresponse force microscopy observation

Interferometric displacement sensor measurements were carried out on a commercial atomic force microscopy system (Asylum Research Cypher ES) equipped with a Polytec OFV-5000 modular vibrometer routed to the tip for measuring tip displacements, that is, converse piezoelectric coefficient ( $d_{33}$ ). The probe used was Au-coated tips (FM-LC) with nominal  $k = 8$  (4–16) N m<sup>-1</sup>. During the interferometric

displacement sensor measurements, the dual AC resonance tracking mode was used to obtain the local butterfly loops. The scanner of Asylum Research Cypher ES has the imaging ability of high spatial resolution, with the closed-loop sensor noise being 60 pm along the  $x/y$  directions and 50 pm along the  $z$  direction, respectively.

### Phase-field simulation

We use the spatial distribution  $P_i(r)$  ( $i = 1, 2, 3$ ) of the local polarization vector and antiferrodistortive oxygen octahedral tilt (OT)  $\theta_i(r)$  ( $i = 1, 2, 3$ ) as the order parameters, governed by the time-dependent Ginzburg–Landau equation<sup>40</sup>:

$$\frac{\partial P_i}{\partial t} = -L_P \frac{\delta F_{\text{tot}}}{\delta P_i}, (i = 1, 2, 3) \quad (1)$$

$$\frac{\partial \theta_i}{\partial t} = -L_\theta \frac{\delta F_{\text{tot}}}{\delta \theta_i}, (i = 1, 2, 3) \quad (2)$$

where  $L_P$  and  $L_\theta$ , both set to be 1 in reduced unit, are the kinetic coefficients related with the domain-wall motion. The total free energy is then the volume integration of the bulk, gradient, electrostatic, elastic, flexoelectric and eDMI energy densities:

$$F_{\text{tot}} = \iiint_{V_{\text{BFO}}} (f_{\text{land}} + f_{\text{grad}} + f_{\text{elec}} + f_{\text{elas}} + f_{\text{flexo}} + f_{\text{DMI}}) dV \quad (3)$$

The bulk energy density is given by

$$\begin{aligned} f_{\text{land}} = & \alpha_{ij} P_i P_j + \alpha_{ijkl} P_i P_j P_k P_l + \alpha_{ijklmn} P_i P_j P_k P_l P_m P_n \\ & + \alpha_{ijklmnuv} P_i P_j P_k P_l P_m P_n P_u P_v + \beta_{ij} \theta_i \theta_j \\ & + \beta_{ijkl} \theta_i \theta_j \theta_k \theta_l + t_{ijkl} P_i P_j \theta_k \theta_l \end{aligned} \quad (4)$$

which includes the Landau energy for polarization, oxygen OT and the coupling terms.  $\alpha_{ij}$ ,  $\alpha_{ijkl}$ ,  $\alpha_{ijklmn}$ ,  $\alpha_{ijklmnuv}$ ,  $\beta_{ij}$ ,  $\beta_{ijkl}$  and  $t_{ijkl}$  are local potential coefficients representing the stiffness with respect to the changes in polarization and oxygen OT. The gradient energy density  $f_{\text{grad}}$  is represented as

$$f_{\text{grad}} = \frac{1}{2} g_{ijkl} P_{i,j} P_{k,l} + \frac{1}{2} \kappa_{ijkl} \theta_{i,j} \theta_{k,l} \quad (5)$$

where  $g_{ijkl}$  and  $\kappa_{ijkl}$  are the gradient energy coefficients of polarization and OT, respectively. The electrostatic energy density  $f_{\text{elec}}$  is given by

$$f_{\text{elec}} = -\frac{1}{2} \epsilon_0 \epsilon_{ij}^b E_i E_j - E_i P_i \quad (6)$$

where  $\epsilon_{ij}^b$  is the background dielectric constant<sup>41</sup> and  $E_i$  is the electric field obtained by solving the electrostatic equilibrium equation  $\epsilon_0 \epsilon_{ij}^b \phi_{,ji} = P_{i,i}$  ( $\phi$  is the electric potential). The flexoelectric energy density  $f_{\text{flexo}}$  can be expressed as

$$f_{\text{flexo}} = \frac{f_{ijkl}}{2} \left( \epsilon_{ij} \frac{\partial P_k}{\partial x_l} - P_k \frac{\epsilon_{ij}}{\partial x_l} \right) \quad (7)$$

where  $f_{ijkl}$  denotes the flexocoupling coefficient tensor<sup>42,43</sup>. The driving force from the flexoelectric effect yields the flexoelectric field  $E_k^{\text{flexo}}$ :

$$\frac{\delta f_{\text{flexo}}}{\delta P_k} = \frac{\partial f_{\text{flexo}}}{\partial P_k} - \frac{\partial}{\partial x_l} \left( \frac{\partial f_{\text{flexo}}}{\partial P_k \partial x_l} \right) = -f_{ijkl} \frac{\partial \epsilon_{ij}}{\partial x_l} = -E_k^{\text{flexo}} \quad (8)$$

Owing to the uncertainties of the magnitude of  $f_{ijkl}$ , four different groups of flexoelectric coefficients are considered, that is, (i)  $f_{ijkl} = 0$ , (ii)  $f_{1111} = 6V$ ,  $f_{1122} = f_{1212} = 0$ , (iii)  $f_{1122} = 6V$ ,  $f_{1111} = f_{1212} = 0$ , and (iv)

$f_{1212} = 6V$ ,  $f_{1111} = f_{1122} = 0$  for simplicity based on the reasonable estimation from previous literature<sup>44,45</sup>. The elastic energy density is

$$f_{\text{elas}} = \frac{1}{2} C_{ijkl} (\varepsilon_{ij} - \varepsilon_{ij}^0) (\varepsilon_{kl} - \varepsilon_{kl}^0) \quad (9)$$

in which  $\varepsilon_{ij}$  is the total strain distribution obtained by solving the mechanical equilibrium equation  $\sigma_{ij,j} = 0$  and  $\sigma_{ij} = C_{ijkl} (\varepsilon_{kl} - \varepsilon_{kl}^0)$ . The eigenstrain  $\varepsilon_{ij}^0$  is coupled to polarization and OT through  $\varepsilon_{ij}^0 = \lambda_{ijkl} \theta_k \theta_l + Q_{ijkl} P_k P_l - F_{ijkl} P_{k,l}$ , where  $Q_{ijkl}$  and  $\lambda_{ijkl}$  are the electrostrictive and rotostrictive tensors<sup>46</sup>, separately. The third term on the right-hand side is incorporated by polarization gradients owing to flexoelectric contribution via the inverse flexoelectric strain coefficient  $F_{ijkl} = S_{ijmn} f_{mnkl}$ , where  $S_{ijmn}$  is the elastic compliance tensor. All equations with repeating subscripts follow the Einstein summation notation, and the comma in subscript means spatial differentiation, for example,  $P_{i,j} = \frac{\partial P_i}{\partial x_j}$ .

As illuminated in the previous reference<sup>20</sup>, the electric Néel and Bloch skyrmions could be induced by the terms  $D_N [\mathbf{u}_z (\nabla \cdot \mathbf{u}) - (\mathbf{u} \cdot \nabla) \mathbf{u}_z]$  and  $D_B \mathbf{u} \cdot (\nabla \times \mathbf{u})$ , respectively. In indicial notation, these terms can be written as  $u_3 u_{i,i} - u_i u_{3,i}$  and  $u_i \varepsilon_{ijk} u_{k,j}$ , respectively, where  $\varepsilon_{ijk}$  is the Levi-Civita symbol. Within the framework of the continual phase-field model, the displacement  $\mathbf{u}$  can be reasonably represented by the order parameter  $\mathbf{P}$ . The eDMI energy contribution can be succinctly expressed as follows:

$$E_{\text{DMI}} = \alpha E_{\text{DMI}}^N + (1 - \alpha) E_{\text{DMI}}^B \quad (10)$$

$$= \alpha D_N (P_3 P_{i,i} - P_i P_{3,i}) + (1 - \alpha) D_B P_i \varepsilon_{ijk} P_{k,j}$$

where  $D_N$  and  $D_B$  denote parameters that modulate the strength of the eDMI with units of  $\text{C}^{-2} \text{m}^3 \text{N}$ . The detailed derivation process of the eDMI driving forces can be found in Supplementary Note 3.

We use the backward Euler method to evolve the phase-field equation. Periodic boundary conditions are applied along the in-plane dimensions, whereas a superposition scheme is implemented along the thickness direction. The thin-film boundary condition is applied, that is, the bottom film interface is coherently clamped by the substrate while the top surface is assumed to be traction-free<sup>47</sup>. All the calculations are performed under open circuit electric boundary conditions unless otherwise specified<sup>48</sup>. All simulations are performed for a temperature of 298 K. The values of all coefficients used in the simulations are listed in Supplementary Table 1.

The discrete three-dimensional mesh of  $64 \Delta x \times 64 \Delta y \times 46 \Delta z$  with a real grid space of  $\Delta x = \Delta y = 0.4 \text{ nm}$  and  $\Delta z = 0.2 \text{ nm}$  are used to describe the system with 15 grids of substrate, 25 grids of thin-film layers and 6 grids of vacuum stacked from the bottom to the top, strained by  $-4.4\%$  compressive biaxial misfit. Besides starting from fully random noise, the simulation commences from a collection of manually constructed states, that is, artificial chains consisting of alternating polarization  $P = (0, 0, +1)$  and  $P = (0, 0, -1)$  stack along the  $[110]$  and  $[\bar{1}10]$  directions respectively with reference to an experimentally determined 1D array width of 2 nm. Additional randomized thermal fluctuations are imposed.

## Data availability

All data are available in the main text or Supplementary Information and also available via Zenodo at <https://doi.org/10.5281/zenodo.14071478> (ref. 49). Source data are provided with this paper.

## References

- Hytch, M. J. et al. Quantitative measurement of displacement and strain fields from HREM micrographs. *Ultramicroscopy* **74**, 131–146 (1998).
- Xue, F. et al. Strain phase separation: formation of ferroelastic domain structures. *Phys. Rev. B* **94**, 220101 (2016).
- Tagantsev, A. K. Landau expansion for ferroelectrics: which variable to use? *Ferroelectrics* **375**, 19–27 (2008).
- Cao, Y. et al. Pressure-induced switching in ferroelectrics: phase-field modeling, electrochemistry, flexoelectric effect, and bulk vacancy dynamics. *Phys. Rev. B* **96**, 184109 (2017).
- Eliseev, E. A. et al. Spontaneous flexoelectric/flexomagnetic effect in nanoferroics. *Phys. Rev. B* **79**, 165433 (2009).
- Liu, D. et al. Phase-field simulations of vortex chirality manipulation in ferroelectric thin films. *npj Quantum Mater.* **7**, 34 (2022).
- Park, S. M. et al. Selective control of multiple ferroelectric switching pathways using a trailing flexoelectric field. *Nat. Nanotechnol.* **13**, 366–370 (2018).
- Morozovska, A. N. et al. Interfacial polarization and pyroelectricity in antiferrodistortive structures induced by a flexoelectric effect and rotostriction. *Phys. Rev. B* **85**, 094107 (2012).
- Li, Y. L. et al. Effect of substrate constraint on the stability and evolution of ferroelectric domain structures in thin films. *Acta Mater.* **50**, 395–411 (2002).
- Li, Y. L. et al. Effect of electrical boundary conditions on ferroelectric domain structures in thin films. *Appl. Phys. Lett.* **81**, 427–429 (2002).
- Geng, W. R. et al. Dipolar wavevector interference induces a polar skyrmion lattice in strained BiFeO<sub>3</sub> films. *Zenodo* <https://doi.org/10.5281/zenodo.14071478> (2024).
- Feng, Y. et al. Misfit strain relaxations of (101)-oriented ferroelectric PbTiO<sub>3</sub>/(La, Sr)(Al, Ta)O<sub>3</sub> thin film systems. *J. Mater. Res.* **33**, 4156–4164 (2018).
- Mateika, D. et al. Mixed-perovskite substrates for high-Tc superconductors. *J. Cryst. Growth* **109**, 447–456 (1991).
- Sasaura, M. et al. Thermal expansion coefficients of high-Tc superconductor substrate NdGaO<sub>3</sub> single crystal. *J. Appl. Phys.* **68**, 3643–3644 (1990).

## Acknowledgements

This work is supported by the National Natural Science Foundation of China (52201018 (W.R.G.), 51971223 (Y.L.Z.), 51922100 (Y.L.T.) and 52122101 (Y.J.W.)), the Guangdong Basic and Applied Basic Research Foundation (2021A1515110291 (W.R.G.) and 2023A1515012796 (W.R.G.)), the China Postdoctoral Science Foundation (2022T150690 (W.R.G.)), the Guangdong Provincial Quantum Science Strategic Initiative (GDZX2202001, GDZX2302001 and GDZX2402001 (X.L.M.)), the Key Research Program of Frontier Sciences CAS (QYZDJ-SSW-JSC010 (X.L.M.)) and the Shenyang National Laboratory for Materials Science (L2019R06 (X.L.M.), L2019R08 (Y.L.Z.), L2019F01 (Y.L.T.) and L2019F13 (Y.J.W.)). Y.L.T. acknowledges the Scientific Instrument Developing Project of CAS (YJKYYQ20200066) and the Youth Innovation Promotion Association of CAS (Y202048). Y.J.W. acknowledges the Youth Innovation Promotion Association CAS (number 2021187). We are grateful to X.-L. Li and X. Zheng at the BL02U2 beamline of Shanghai Synchrotron Radiation Facility for experimental assistance and discussions.

## Author contributions

W.R.G., Y.L.Z. and M.X.Z. contributed equally to this work. X.L.M. conceived the project on the architecture of quantum materials modulated by ferroelectric polarizations. W.R.G., Y.L.Z. and X.L.M. designed the sample structures and subsequent experiments. W.R.G. performed the thin-film growth and STEM observations. W.R.G., Y.L.T., J.H.W., R.J.J., S.Z.L., X.Y.S., Y.P.F. and M.J.Z. performed the TEM and STEM observations. M.X.Z., H.J.Z., C.H.L. and Y.J.W. performed the phase-field simulations. Y.J.W. carried out digital analysis of the STEM data. All authors participated in discussion and interpretation of the data.

# Reversible Manipulation of Polar Topologies in Oxide Ferroelectrics via Electric Fields

Yan-Peng Feng, Han Wu, Yin-Lian Zhu,\* Yu-Jia Wang, Yun-Long Tang, and Xiu-Liang Ma\*

**Polar topologies show great potentials in memories and other nano-micro devices. To integrate with silicon conducting circuits, it is vital to understand the dynamic evolution and the transformation of different domain configurations under external stimulus. Here in situ transmission electron microscopy is performed and the electrically controlled creation and annihilation of large-scale polar flux-closure array from typical  $c/a$  domains in  $\text{PbTiO}_3/\text{SrTiO}_3$  bilayers is directly observed. It is found that the transformation is reversible after removal of external electric fields. Increasing external electric fields on  $(\text{PbTiO}_3/\text{SrTiO}_3)_5$  multilayered films, it is further found that the flux-closure domains are nucleated and propagated via the steps of first the formation of new  $c$  domains and then connection with neighboring  $c$  domains. The transition from  $a/c$  domains to flux-closure arrays under electric fields is collaborated with evaluating energy variations by phase-field simulations in which the electrostatic energy plays an important role. These results demonstrate the polar topologies can be reversibly manipulated by external stimuli, which sheds light on further understanding the dynamics behavior of polar topologies and helps for future nanoelectric applications.**

energy, the electrostatic energy and the polarization gradient energy in ferroelectric oxide films, which have attracted much attention from researchers.

It is necessary for future applications in electronics that the topological polar structures are effectively modulated by external stimuli. Some theoretical and experimental studies have revealed the evolution of topological polar structures under external heating, optical, electric and straining field. For example, the flux-closure domains hold stable under the temperature heating to  $\approx 450$  °C and the polar vortices can transform to ferroelectric  $a_1/a_2$  domains at  $\approx 200$  °C.<sup>[15,16]</sup> It is reported that the mixed phases with polar vortices and  $a_1/a_2$  domains can convert to a pure vortex phase under electric field and transform to a supercrystal phase by ultrafast optical pulse.<sup>[16,17]</sup> Other studies demonstrated different phenomena such as the polar flux-closure and vortices have transitions to  $a/c$  domains or polar waves,<sup>[18–22]</sup>

## 1. Introduction

Topological polar structures with nanometer sizes and exotic physical properties hold promise for electronics applications, including the high-density information storage devices and low power field effect transistor.<sup>[1–8]</sup> Recently, many topological polar structures, such as polar flux-closures,<sup>[9]</sup> vortices,<sup>[10]</sup> skyrmions,<sup>[11]</sup> merons,<sup>[12]</sup> Solomon rings,<sup>[13]</sup> and Bloch points<sup>[14]</sup> have been stabilized by balancing the competition of the elastic

and polar skyrmions are converted to a trivial monodomain under electric or mechanical strain stimuli.<sup>[23]</sup> Besides, the reversible transition from a polar skyrmions to meron lattices was also reported under varying the temperature in  $\text{PbTiO}_3/\text{SrTiO}_3$  (PTO/STO) membranes.<sup>[24]</sup> Up to now, the phase transition behavior of topological polar structures under external stimulus remains elusive and need further elucidation.

Furthermore, to facilitate the design and integration of electronic devices, it is essential to obtain large scale period arrays

Y.-P. Feng, Y.-L. Zhu, X.-L. Ma  
Bay Area Center for Electron Microscopy  
Songsan Lake Materials Laboratory  
Dongguan, Guangdong 523808, China  
E-mail: zhuyinlian@sslslab.org.cn; xhma@iphy.ac.cn

Y.-P. Feng, Y.-L. Zhu, X.-L. Ma  
Quantum Science Center of Guangdong-HongKong-Macao Greater Bay Area  
Shenzhen 518048, China

H. Wu, Y.-J. Wang, Y.-L. Tang  
Shenyang National Laboratory for Materials Science  
Institute of Metal Research  
Chinese Academy of Sciences  
Wenhua Road 72, Shenyang 110016, China

H. Wu, Y.-J. Wang, Y.-L. Tang  
School of Materials Science and Engineering  
University of Science and Technology of China  
Wenhua Road 72, Shenyang 110016, China

Y.-L. Zhu  
School of Materials Science and Engineering  
Hunan University of Science and Technology  
Xiangtan 411201, China

X.-L. Ma  
Institute of Physics  
Chinese Academy of Sciences  
Beijing 100190, China

X.-L. Ma  
State Key Lab of Advanced Processing and Recycling on Non-ferrous Metals  
Lanzhou University of Technology  
Lanzhou 730050, China

The ORCID identification number(s) for the author(s) of this article can be found under <https://doi.org/10.1002/adma.202414346>

DOI: 10.1002/adma.202414346

of polar topologies under external stimulus. Previously, it has been revealed that isolated three-fold polar vertices are nucleated and moved under electric field by in situ transmission electron microscopy (TEM) method.<sup>[25]</sup> On the other hand, the centre-convergent and centre-divergent polar textures were written and erased by conductive piezoelectric force microscope (PFM) tips in multiferroic BiFeO<sub>3</sub> films.<sup>[26]</sup> Nonetheless, the former mainly focuses on the creation and movement of several scattered topological structures and the latter writes too large polar textures with submicrometer size due to the restriction of PFM method. Thus, how to create the large-scale topological polar array from ordinary ferroelectric domains by external stimuli is more challenging.

In this work, the polar flux-closure domains were chosen as a model system to investigate the dynamic behaviors of polar topologies under external stimuli. We experimentally perform in situ TEM to reveal the electrically controlled creation and annihilation of flux-closure arrays in both PTO/STO bilayers and (PTO/STO)<sub>5</sub> multilayered films. The nucleation and propagation of flux-closure domains from ordinary *a/c* domains were displayed via the formation of new *c* domains from parent *a* domains with the electric field increase. The new *c* domains exhibit opposite polarizations and connect with neighboring *c* domains to form a large-scale flux-closure array. Besides, the flux-closure domains are annihilated and reverted to *a/c* domains with the reduction of external electric field. Phase-field simulations demonstrate that the transition from *a/c* to flux-closure domains is accompanied with the reduction of total energy, which mainly due to the decrease of electrostatic energy. These results verify that the electrically controlled polar topological structures can be successfully achieved, which is useful for applications in nanoelectronic devices.

## 2. Results and Discussion

The (PTO)<sub>21</sub>/(STO)<sub>10</sub> bilayer films were grown on SrRuO<sub>3</sub>-buffered orthorhombic (110)-oriented GdScO<sub>3</sub> (GSO) substrate by pulsed laser deposition (PLD) (film deposition details are shown in Experimental Section), where the subscripts “21” and “10” denote the number of unit cells in PTO and STO layers, respectively. For simplicity, the orthorhombic (110)-oriented GSO is treated as pseudocubic (simplified as “pc”) (001)-oriented. The X-ray diffraction (XRD) measurements were performed for PTO/STO bilayer, as shown in Figure S1 (Supporting Information). The  $\theta-2\theta$  scan pattern (Figure S1a, Supporting Information) of PTO/STO bilayers exhibits no obvious impure peak except three main peaks from GSO substrate, which indicates that the films have a well crystallinity and no impure phases. Meanwhile, several weak peaks appear around each main peak, which come from films. The inset shows fine  $\theta-2\theta$  scan for (002) peak of PTO/STO bilayers. Two peaks marked as (002) and (200) of PTO are distributed on the left and right sides of the main peak, respectively. It indicates that *c* and *a* domains simultaneously appear in PTO layer. Figure S1b (Supporting Information) shows the reciprocal space mapping (RSM) of (002) diffraction pattern of PTO/STO bilayers. It is seen that the PTO-(200) spot exhibits a narrow pattern and no significant expansion along the  $q_x$  direction. The cross-sectional dark-field TEM image along [010]<sub>pc</sub> zone axis (Figure 1a) shows the inclined stripe domains appear in PTO layer, which is identified as 90°

*a/c* domains as reported previously.<sup>[27]</sup> A cross-sectional high-angle annular dark-field (HAADF) scanning transmission electron microscopy (STEM) image (Figure 1b) was acquired by an aberration-corrected scanning transmission electron microscope, showing the sharp and smooth interface between PTO and STO layer. It is seen that the thickness the PTO and STO layer are  $\approx 21$ - and 10-unit cells, respectively. The out-of-plane lattice strain ( $\epsilon_{yy}$ ) (Figure 1c) was extracted by geometric phase analysis (GPA), showing the periodic 90° *a/c* domains. The widely red-colored areas denote *c* domains with out-of-plane polarizations while the narrowly green-colored areas denote *a* domains with in-plane polarizations. A typical area marked by dashed box in Figure 1b was magnified and the atomic-scale HAADF-STEM images were acquired. The superposition of reversed Ti-displacement vectors ( $-\delta_{Ti}$ ) and the atomic-resolved HAADF-STEM image is shown in Figure 1d, where the  $-\delta_{Ti}$  vectors (marked by yellow arrows) of PTO unit cells are consistent with the polarization directions. It is seen that the polarization direction of PTO unit cells features the change of  $\approx 90^\circ$  across the inclined domain walls, which indicates that the stripe domains are typical 90° *a/c* domains. The out-of-plane lattice parameter mapping (Figure 1e) corresponding to Figure 1d also exhibits an inclined stripe pattern, which is consistent with GPA results.

The external electric bias was added on the cross-sectional TEM samples to investigate the evolution of ferroelectric domains under electric fields via a tungsten (W) tip in TEM by a double-tilt in situ TEM holder. During in situ experiments, the electric potential of the W tip is kept to 0 V since the W tip is connected to the ground. A chronological series of dark-field TEM images (Figure 2) were cut from in situ Movie S1 (Supporting Information), which shows the creation and annihilation processes of polar flux-closure domains from ordinary 90° *a/c* domains in the PTO layer. More details of the process are shown in Movie S1 (Supporting Information). The schematic of the transition process is displayed at the bottom of each image (Figure 2a–f). The typical areas labeled as dashed rectangle boxes in Figure 2a–f were magnified to show the transition details of the process in Figure 2g. It is seen that a new *c* domain (marked by yellow dashed lines in Figure 2g) along the direction of a white arrow starts to appear from parent *a* domains and connects with neighboring *c* domains to form sinusoidal wave contrast at 1 V (Figure 2b). It is the typical polar flux-closure domains as reported previously.<sup>[9]</sup> When the external electric voltage is increased to 2 V, more *c* domains appear from parent *a* domains and transform to a large flux-closure array with the length of  $\approx 130$  nm in the PTO layer (Figure 2c). When the electric voltage is continually increased to 3 V, the flux-closure array has no obvious expansion (Figure 2d). Figures S2a–c (Supporting Information) show the formation of the large-scale flux-closure array is accomplished within a single time step of 100 ms at 2V. The length variation of flux-closure array with time is shown in Figure S2d (Supporting Information). It is noted that the expansion velocity of flux-closure array is more than 1200 nm s<sup>-1</sup> as the external voltage is increased to 2 V. When a smaller time step of 10 ms was adapted to record the in situ transition of *a/c* domains to flux-closures, it is found that the formation of flux-closures can still be accomplished within a single time step of 10 ms (Figure S3, Supporting Information), which indicates that the transition from *a/c* to flux-closures is really very fast. When the electric

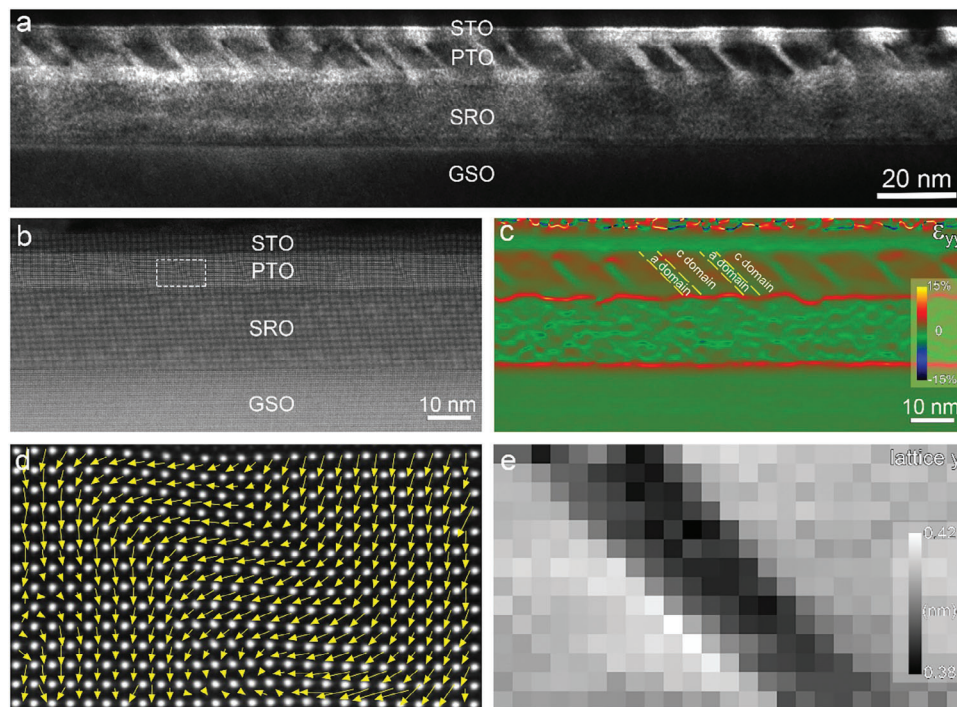


**Figure 1.** The domain structures in PTO/STO bilayer films grown on SRO-buffered GSO(110) substrates. a) Dark-field TEM image taken along  $[010]_{pc}$  zone axis of the PTO/STO bilayer film showing the formation of ordinary  $a/c$  domains in PTO layer. b) The low-magnification HAADF-STEM image taken along  $[010]_{pc}$  direction of the PTO/STO bilayer film. c) Out-of-plane lattice strain ( $\epsilon_{yy}$ ) by geometric phase analysis (GPA) corresponding to the area of (b). d) Superposition of reversed Ti-displacement vectors ( $-\delta_{Ti}$ ) and the atomic-resolved HAADF-STEM image corresponding to the area marked by dashed box in (b), revealing the polarization mapping of  $a/c$  domains. e) Out-of-plane lattice parameter mapping corresponding to the area of (d).

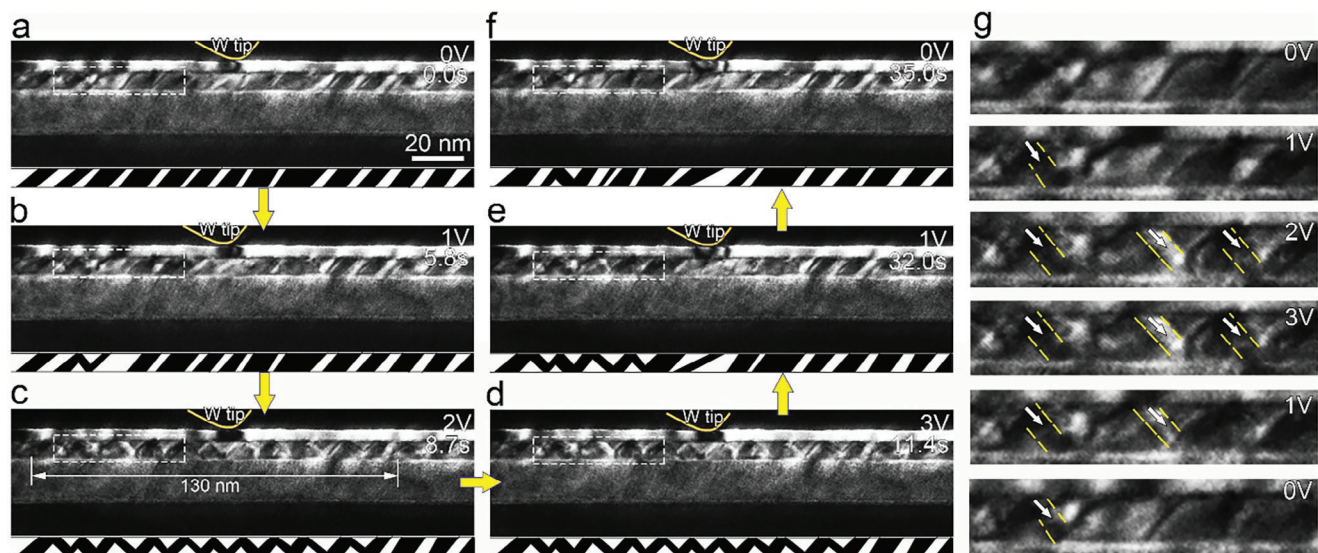


**Figure 2.** A series of dark-field TEM images with the same magnification from in situ video under external electric fields of the PTO/STO bilayer film. a–d) The dark-field TEM image series with  $g = 200$  under the external electric field increased from (a) 0 V to (b) 1 V, (c) 2 V, (d) 3 V. e, f) The dark-field TEM image series with  $g = 200$  under the external electric field decreased from 5 V, to (e) 1 V, (f) 0 V. g) The magnified dark-field TEM images marked by dashed rectangle boxes in (a–f), respectively. The yellow dashed lines denote the generated  $c$  domains from parent  $a$  domains, which are along the directions of white arrows.

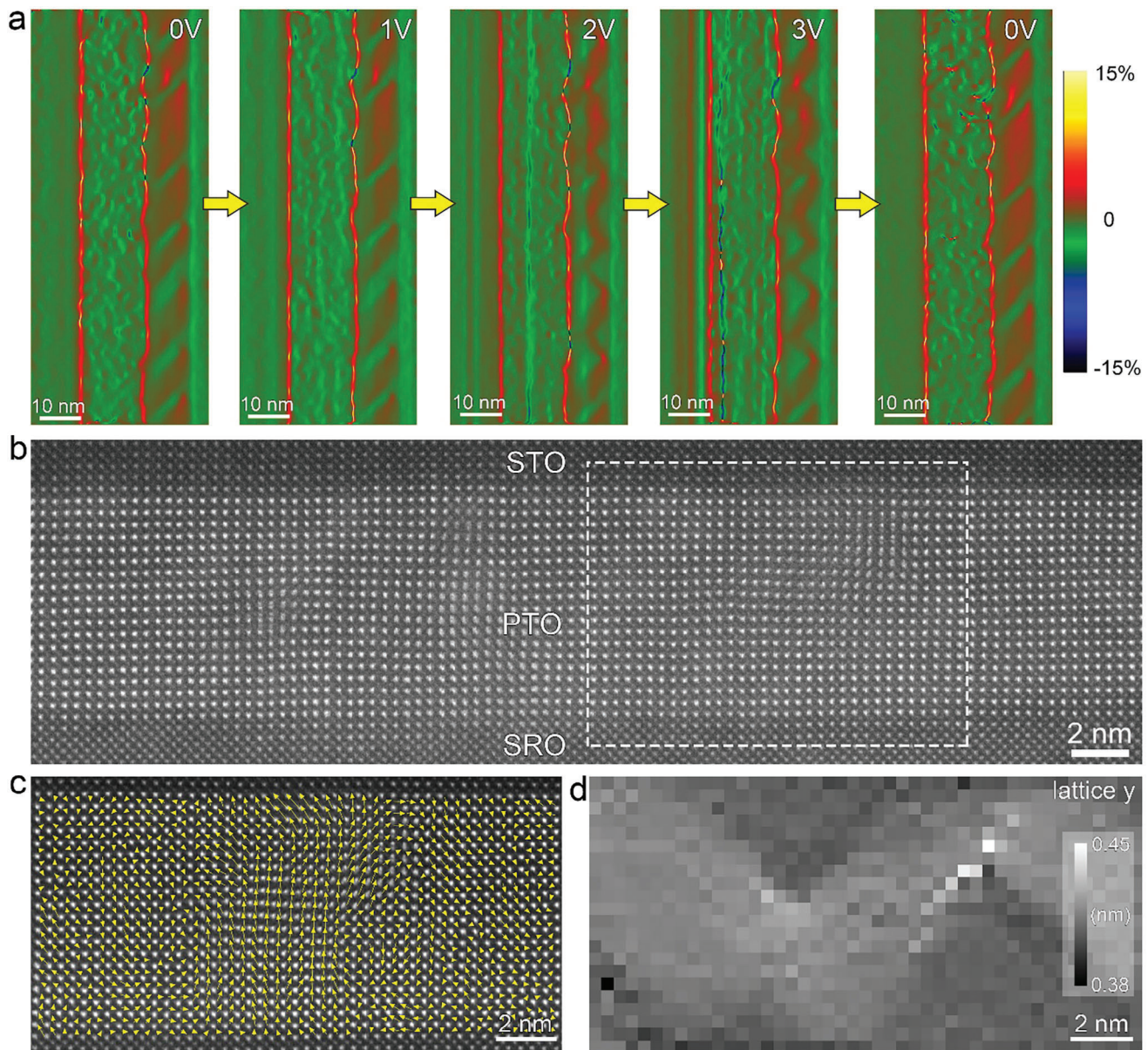


**Figure 3.** The evolution of domains in PTO/STO bilayered films under external electric fields. a) The out-of-plane lattice strain ( $\epsilon_{yy}$ ) mapping showing the evolution of domains in PTO/STO bilayer film under external electric field. b) The atomic-scale HAADF-STEM image of PTO layer under external electric voltage of 3V. c) Superposition of reversed Ti-displacement vectors ( $-\delta_{Ti}$ ) and the atomic-resolved HAADF-STEM image corresponding to the area marked by dashed box in (b), revealing the polarization mapping of flux-closure domains at 3 V. d) The out-of-plane lattice parameters of PTO unit cells corresponding to the area of (c).

voltage is decreased to 1 V, the large flux-closure array starts to be broken, and a shorter flux-closure array is reserved (Figure 2e). When the electric voltage returns to 0 V, one flux-closure domain (marked by a white arrow in Figure 2g) is still reserved, which displays an asymmetric transition between the processes of the increasing and decreasing electric field.

To precisely investigate the creation and annihilation processes of flux-closure domains, in situ external electric field experiment was performed under STEM mode in an aberration-corrected scanning transmission electron microscope. The out-of-plane lattice strain ( $\epsilon_{yy}$ ) mappings (Figure 3a) corresponding to a chrono-

logical series of original high-resolution HAADF-STEM images taken along  $[010]_{pc}$  directions (Figure S4, Supporting Information) were acquired to show the formation details of the flux-closure array. The domain configuration in the observed area has no obvious change when the external electric voltage is increased to 1 V. The large flux-closure array with a sinusoidal wave starts to appear at 2 V, which is different from the variation under TEM observation (Figure 2). The further current measurements of transition from  $a/c$  to flux-closures are performed under TEM and STEM modes, respectively. It indicates that the  $a/c$  domains start to transform into flux-closures with the current of

$8.01 \times 10^{-9}$  A under TEM mode and  $7.18 \times 10^{-9}$  A under STEM mode, which are very approximate. The difference in voltages between TEM and STEM modes might come from several factors, such as different tips, physical contact and the surface condition of samples. Then the flux-closure array has no obvious expansion as the external electric voltage reaches to 3 V, where the period of the created flux-closure domains is  $\approx 16$  nm. Finally, the flux-closure array disappears and transform to  $a/c$  domains in the observed area when the external electric voltage returns to 0 V. Besides, the atomic-resolved HAADF-STEM image at 3 V was acquired and shown in Figure 3b. Figure 3c shows the superposition of reversed Ti-displacement vectors ( $-\delta_{\text{Ti}}$ ) and the atomic-resolved HAADF-STEM image corresponding to the area labeled as dashed box in Figure 3b. It is clearly seen that the flux-closure polarization pattern appears in PTO layer. The out-of-plane lattice strain mapping (Figure 3d) corresponding to Figure 3c exhibits a sinusoidal wave pattern, which is a typical feature of the flux-closure domains. Therefore, the creation and annihilation of polar flux-closure array were controllably achieved by the external electric field in the PTO/STO bilayer film.

Even so, the details of nucleation and expansion for polar flux-closure domains were not captured in PTO/STO bilayer films, which might be due to the too fast transition of ordinary  $a/c$  to polar flux-closure domains. To slow down this process, the [(PTO)<sub>22</sub>/(STO)<sub>10</sub>]<sub>5</sub> multilayer films were grown on SrRuO<sub>3</sub>-buffered GSO(110) substrate by pulsed laser deposition (film deposition details are shown in Experimental Section), where the subscripts “22” and “10” denote the number of unit cells in PTO and STO layers, and “5” denotes five periods of the (PTO)<sub>22</sub>/(STO)<sub>10</sub> unit. Similarly, the XRD  $\theta$ - $2\theta$  scan pattern (Figure S5a, Supporting Information) of (PTO/STO)<sub>5</sub> multilayered films indicates that the films have a well crystallinity and no impure phases. The difference with PTO/STO bilayer is that the PTO-(002) RSM diffraction pattern (Figure S5b, Supporting Information) of (PTO/STO)<sub>5</sub> multilayered films exhibits an obvious expansion along the  $q_x$  direction, which might indicate that the periodic polar topological domains appear in the films as previously.<sup>[28]</sup> The cross-sectional dark-field TEM image (Figure S6, Supporting Information) shows the inclined  $a/c$  stripe domains in the first PTO layer and flux-closure domains in the second to fifth PTO layers. A cross-sectional HAADF-STEM image (Figure S7a, Supporting Information) shows the thicknesses of each PTO and STO layers are  $\approx 22$ - and 10-unit cells, respectively. Similarly, the out-of-plane strain ( $\epsilon_{yy}$ ) mapping (Figure S7b, Supporting Information) exhibits the inclined stripe contrast in the first PTO layer and a periodic sinusoidal wave in the second to fifth PTO layers. It is confirmed that the inclined stripe contrast is  $90^\circ$   $a/c$  domains and the periodic sinusoidal wave are flux-closure domains by the polarization mapping (Figure S7c,e, Supporting Information) corresponding to the area labeled as “I”-“II” in Figure S7a (Supporting Information). The out-of-plane lattice parameter mappings (Figure S7d,f, Supporting Information) corresponding to Figure S7c,e (Supporting Information), respectively, also feature an inclined stripe pattern in  $a/c$  domains and periodic sinusoidal wave pattern in flux-closure domains, which are consistent with GPA results in Figure S7b (Supporting Information). Therefore, the dark-field TEM images and the out-of-plane strain mapping (or lattice parameter mapping) based on atomic-resolved HAADF-STEM images can be utilized to iden-

tify  $90^\circ$   $a/c$  and flux-closure domains. Similarly, a chronological series of dark-field TEM images (Figure S8, Supporting Information) shows that the processes of nucleation, expansion, and annihilation for flux-closure domains in the first PTO layer. To highlight the transition in the first PTO layer, the non-interest areas of second to fifth PTO layers are cropped in these images. More details of the process are shown in Movie S2 (Supporting Information). The schematic of the transition process is also displayed at the bottom of each image (Figure S8a, Supporting Information). Figure S8b (Supporting Information) shows the magnified dark-field TEM images corresponding to the selected areas at several typical electric voltages (marked by white boxes), which clearly displays the process of nucleation, expansion, and annihilation for flux-closure domains. It is seen that the flux-closure domain nucleates at 10 V, where a new  $c$  domain appears from the top PTO/STO interface (marked by a dashed circle in Figure S8b, Supporting Information). When the external electric voltage is increased to 11 V, other five new  $c$  domains appear and connect with neighboring  $c$  domains to form flux-closure domains (Figure S8a, Supporting Information). When the electric voltage is kept at 11 V and the time is increased from 25.3 to 26.6 s, the formation of more new  $c$  domains generates a large flux-closure array. When the electric voltage is increased to 13 and 15 V, the flux-closure domain array continues to extend. The length of finally flux-closure array at 15 V is up to 160 nm. The reduction of electric voltage was continually performed to observe the annihilation processes of flux-closure array. When the electric voltage is decreased to 10 V, the flux-closure array has no obvious change (Figure S8a, Supporting Information). Until the electric decreases to 7 V, the continuous flux-closure array starts to be broken via some  $c$  domains switched to  $a$  domains (marked by dashed rectangle box in Figure S8b, Supporting Information). Finally, all flux-closure domains disappear and transform to  $a/c$  domains at 4 V. The domain configuration returns to original state when the voltage reduces to 0 V.

Similarly, in situ external electric field experiment of the (PTO/STO)<sub>5</sub> multilayer film was performed under STEM mode to clearly reveal the process of nucleation, expansion, and annihilation for polar flux-closure domains. The out-of-plane lattice strain mappings (Figure 4) corresponding to a chronological series of original high-resolution HAADF-STEM images (Figure S9, Supporting Information) show the flux-closure domains start to nucleate at 10 V. It is seen that two new  $c$  domains (labeled as white arrows) appear from parent  $a$  domains and connect with neighboring  $c$  domains to form flux-closure domains while one narrowly new  $c$  domain (labeled as a dashed box) starts to nucleate (Figure 4b). The  $c$  domain widens and grows up to connect with neighboring  $c$  domains at 11 V (Figure 4c) and continually widens at 13 V (Figure 4d). Therefore, it is directly observed that the formation of flux-closure domains is realized by the nucleation, growth, and widening of new  $c$  domains from parent  $a$  domains. Ultimately, the flux-closure domains extend to form a sinusoidal wave array at 13 V (Figure 4d). Similarly, the annihilation of flux-closure domains was observed with the external electric voltage reduced. The out-of-plane strain mapping (Figure 4e) at 7 V shows that several  $c$  domains (labeled as yellow dashed boxes) transform to  $a$  domains and further break the flux-closure array. Besides, other  $c$  domains (labeled as a white arrow) reduce to narrow stripes. Finally, the flux-closure array fully returns to

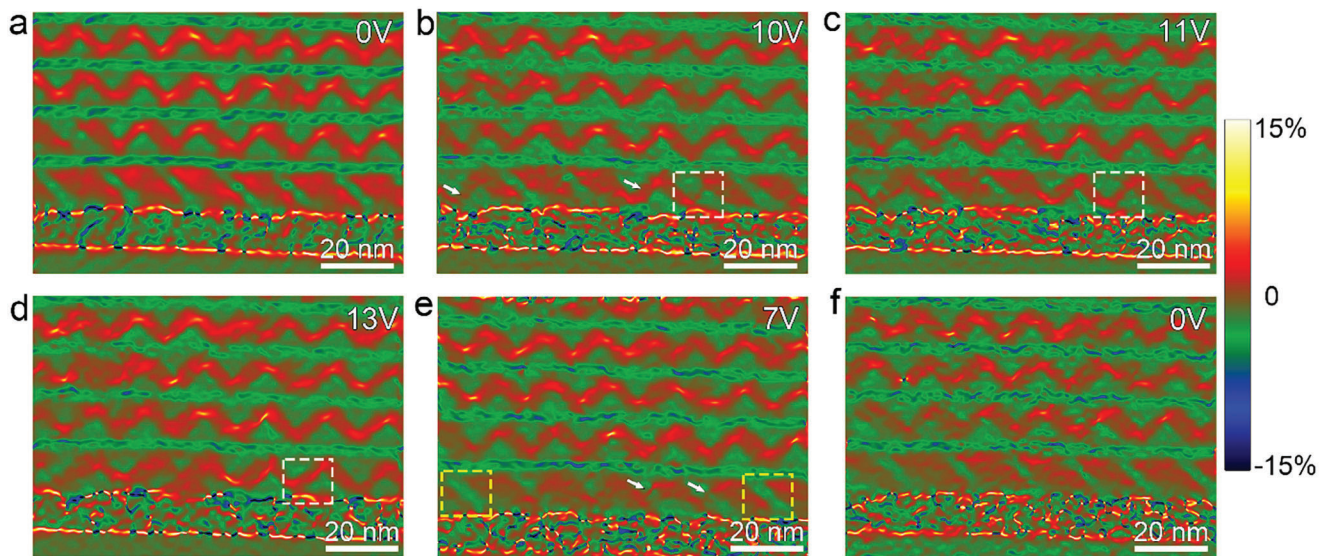


**Figure 4.** The out-of-plane lattice strain ( $\epsilon_{yy}$ ) mapping shows the evolution of domains in  $(\text{PTO}/\text{STO})_5$  multilayered films under external electric fields. a) The initial domain structures in  $(\text{PTO}/\text{STO})_5$  films under an applied voltage of 0 V. b–d) The evolution of domain structures in  $(\text{PTO}/\text{STO})_5$  films with the external electric voltage increased from 0 V to 10 V (b), 11 V (c), 13 V (d). e, f) The evolution of domain structures in  $(\text{PTO}/\text{STO})_5$  films with the external electric voltage decreased to 7 V (e), 0 V (f).

$a/c$  domains when the electric voltage reduces to 0 V (Figure 4f). Therefore, the annihilation of flux-closure domains is realized by the narrowing of  $c$  domains and further transition to  $a$  domains.

Generally, the domain configuration in ferroelectric films depends on the competition of the bulk, gradient, elastic, and electrostatic energies of system.<sup>[10,12,14]</sup> As reported previously, when the upper and lower sides of the PTO layer are the same electrodes or insulators, the flux-closure domains are more easily stabilized.<sup>[9,29,30]</sup> Whereas the flux-closure domains will change to  $a/c$  domains if the upper and lower sides of the PTO layer are the different films.<sup>[30]</sup> Therefore, the formation of  $a/c$  domains in the  $(\text{PTO})_{21}/(\text{STO})_{10}$  bilayer film and the first PTO layer of  $[(\text{PTO})_{22}/(\text{STO})_{10}]_5$  multilayer film might be attributed to the asymmetric top STO and bottom SRO of the PTO layer. The built-in electric field is induced in the PTO layer and points to SRO electrode due to the work function difference between top STO, bottom SRO, and PTO layer, which leads to the polarization away from top STO and pointing to bottom SRO electrode.<sup>[31–33]</sup> When the positive electric voltage was added to PTO layers, the current flows from films to W tips, which can induce the formation of new  $c$  domains with opposite polarization. As the polarization of new  $c$  domains transitions from ferroelectric PTO to dielectric STO layer, a large polar discontinuity normal to the interface is likely to appear and therefore there is a strong driving force to make polarization rotation, which may promote the transition from  $a/c$  domains to flux-closures.<sup>[10,34]</sup>

The phase-field simulations were performed to rationalize the formation of  $a/c$  domains in the PTO layer with the asymmetric boundary condition and the nucleation, expansion, and annihilation mechanisms of flux-closure domains under external electric field. Two electric fields, i.e., the built-in one due to the asymmetric boundary condition and the one generated by the biased tip, were considered to compete with each other, resulting in the observed transformation, as schematically shown in Figure 5a.

First, a built-in electric field with  $0.9 \text{ MV cm}^{-1}$  was introduced to simulate the asymmetric boundary condition. Under this built-in electric field, the  $a/c$  domains are stabilized in the PTO layer (Figure 5b). Next, a tip with the diameter of 20 nm was applied to the top of the film, which generates an electric field ( $E_{\text{tip}}$ ) with opposite direction to the built-in one. The electric potential distribution on the top of the film generated by the tip reads:<sup>[35]</sup>

$$\Phi(x) = \Phi_0 \frac{r}{\sqrt{(x-x_0)^2 + r^2}} \quad (1)$$

where  $x_0$  is the location of the tip,  $\Phi_0$  is the electric potential of the tip, and  $r$  is the radius of the tip. The distributions of the electric field generated in the film for tip potentials of 0.8 and 2.0 V are shown in Figure S10 (Supporting Information). It is seen that the  $a/c$  domains start to partially transform into flux-closure domains with the time step of 20 000 (where each time step is 1 fs) at 0.8 V (Figure 5c), which indicates that the nucleation of flux-closures occurs in  $\approx 20$  picoseconds. When the tip potential increases to 2.0 V, the  $a/c$  domains in PTO layer completely disappear and transform into the flux-closure array. The period of created flux-closure domains is  $\approx 18 \text{ nm}$  (Figure 5d), which is approximate to the experimental results (Figure 3a). Besides, as marked by dashed boxes in Figure 5c,d, it is clearly seen that a new  $c$  domain appears from the parent  $a$  domain with the increasing of the tip potential from 0.8 to 2.0 V, which promotes the formation of flux-closure domains. Then, when the tip potential is reduced from 2.0 to 0.8 V, the flux-closure array is broken and partially returns to  $a/c$  domains (Figure 5e). When the tip potential is reduced to 0 V, the flux-closure array does not fully return to  $a/c$  domains and a flux-closure domain is still retained (Figure 5f), which is consistent with experimental observation in the bilayer PTO/STO film (Figure 2). Figure 5g shows the variation of the

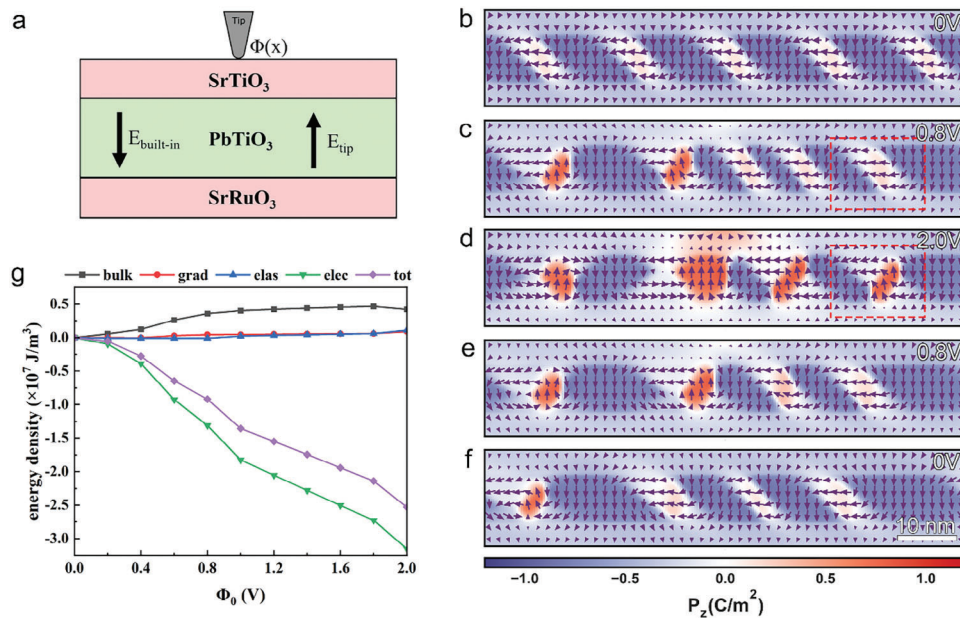


**Figure 5.** The domain evolution in PTO/STO films under electric fields by phase-field simulations. a) The schematic structure of the model used for phase-field simulations. The competition of the built-in electric field due to the work function difference between PTO and SRO ( $E_{\text{built-in}}$ ) and that caused by the tip electric potential ( $E_{\text{tip}}$ ) is shown. b–f) The domain structures of the model with different electric potentials from the tip. The potentials of the tip are 0 V (b), 0.8 V (c), 2.0 V (d), 0.8 V (e) and 0 V (f), respectively. g) Variation of the averaged bulk (bulk), gradient (grad), elastic (elas), electrostatic (elec), and total (tot) energy densities with the increase of tip potential in the PTO film by phase-field simulations.

averaged bulk (bulk), gradient (grad), elastic (elas), electrostatic (elec), and total (tot) energy densities in the PTO layer with the increase of tip potential by phase-field simulations. It is revealed that the total energy density of the film decreases continuously due to the decrease of the electrostatic energy density as the transition from *a/c* to the flux-closure domains, which is probably attributed to the effect of external electric field. Thus, the electrostatic energy plays the important role in the nucleation and expansion of flux-closure domains.

As previously, many polar topological domains have been prepared by selecting proper misfit strain and growing multi-layer or superlattice films.<sup>[9–14]</sup> The phase transition behaviors of some polar topological domains under external electric field have been mainly reported. Specifically, Hong et al revealed that polar vortices can move toward each other and then change into polar skyrmion bubbles under electric fields by phase-field simulations.<sup>[36]</sup> Experimentally, the polar vortices or flux-closures can transform into a wave state, vortex domain walls, or *a/c* domains and eventually evolve into a single polarization state with the increase of the applied electric field.<sup>[18,20,37]</sup> The electrostatic or gradient energy was pointed to be a main driving force in these transition processes of polar topologies. Besides, it has been reported that polarization vortex can be induced by switching electric field in ferroelectric films.<sup>[38]</sup> In our work, we mainly focused on the process of controllably manipulating polar topologies from ordinary domains by external stimuli. The large-scale flux-closure array can be created from ordinary *a/c* domains under electric field, which bridges the gap between *a/c* domains and polar topologies. It is pointed out that the decrease of electrostatic energy is the main driving force. It indicates that the dynamics behavior of flux-closures is similar to polar vortices,

which might be related to the similar polar configuration between flux-closures and vortices. Besides, the phase diagram for (PTO)<sub>*n*</sub>/(STO)<sub>*n*</sub> superlattices have revealed that the flux-closure domains can be stabilized when the thickness of PTO is over 18 unit cells.<sup>[10]</sup> Thus, the transition from *a/c* to flux-closures is reasonable under electric field due to the PTO layers to be more than 20 unit cells in our films.

Meanwhile, theoretical simulation has predicted that the phase transitions of polar vortices to single polarization state are finished within several picoseconds.<sup>[16]</sup> Gruverman et al observed experimentally that a vortex domain can be formed during polarization switching with 100 ns scale in small circular capacitors.<sup>[39]</sup> In our work, experimentally, due to the limit of exposure speed of recording camera, we only observed that the formation of flux-closures from *a/c* domains is accomplished within a single time step of 10 ms. But phase-field simulations demonstrate that the transition from *a/c* to flux-closures in PTO/STO bilayers occurs in  $\approx 20$  picoseconds, which is comparable with previous work.<sup>[16]</sup> Meanwhile, the formation of large-scale flux-closure array exhibits a large expansion velocity of  $> 1200 \text{ nm s}^{-1}$ , which is much faster than the moving velocity of domain walls and isolated three-fold vertices.<sup>[25,40]</sup> Furthermore, a large-scale flux-closure array over 100 nm was created in both PTO/STO bilayers and (PTO/STO)<sub>5</sub> multilayered films. As reported previously, the closure domains are usually formed to be a low-field phenomenon.<sup>[39,41]</sup> On the other hand, we observed that it just needs to create new *c* domains from parent *a* domains in the transition from *a/c* to flux-closures, rather than completely reversal of ferroelastic domains. Thus, we think the creation of flux-closures from *a/c* domains in our films might need a lower switching field compared with conventional switching, which leads to the fast

and large-scale transition. Our results not only indicate that the large-scale polar topologies can be manipulated by external stimuli, but also might provide an approach to achieve ultra-fast information storage with low-power consumption.

Finally, it is noted that the process of TEM sample preparation can also lead to phase transitions in ferroelectric films. For example, Tan et al reported that the topologically trivial  $a_1/a_2$  stripe-like domains can transform into arrays of polar vortex in (PTO)/(STO) superlattice grown on DyScO<sub>3</sub> (DSO) substrates when preparing cross-sectional TEM lamella.<sup>[42]</sup> Nevertheless, in our work, the XRD results exhibit that the PTO-(200) spot of PTO/STO bilayers have no significant expansion along the  $q_x$  direction (Figure S1, Supporting Information), which indicates that the flux-closures do not appear in the PTO/STO bilayers. On the other hand, the PTO/STO bilayers grown on SRO-buffered GSO substrates sustain a larger tensile strain constraint compared to the PTO/STO superlattices on DSO substrates, which might make the domains more stable. Therefore, it demonstrated that the domain structure in PTO/STO bilayers remains invariant associated with TEM sample preparation.

### 3. Conclusion

In summary, we demonstrated electrically controlled creation and annihilation of polar flux-closure domains. By using in situ (S)TEM methods, we observed that the large-scale flux-closure array is nucleated and propagated from ordinary a/c domains in both PTO/STO bilayer and (PTO/STO)<sub>5</sub> multilayer films under external electric field. Specifically, the new c domains appear from parent a domains and then connect with neighboring c domains, which promotes the formation of large-scale flux-closure array. The length of flux-closure array is up to 160 nm. After removal of external electric field, the flux-closure array is broken and gradually converts to a/c domains. Phase-field simulations reveal the formation process of flux-closure domains and indicate that the transition of a/c domains to flux-closure array is accompanied by the reduction of electrostatic energy. This work demonstrates the possibilities of artificial modulation of periodic topological polar structures, which may provide a method to modulate other topological polar arrays by external electric field, such as polar vortices and skyrmions, and further help for future application in nanoelectric devices.

### 4. Experimental Section

**Film Deposition:** The PTO/STO bilayer and multilayer films were grown on SRO-buffered orthorhombic (110)-oriented GSO single-crystal substrate by pulsed laser deposition (PLD). The sintered SRO target, STO target with stoichiometry, and sintered PTO target with 3 mol % Pb enrichment were used to deposit SRO, STO, and PTO layers, respectively. Before deposition, the GSO substrates were heated to 800 °C and then kept for 10 min to clean the substrate surface. Meanwhile, each target was alternately pre-sputtered for 5 min to clean the target surface. During SRO films deposition, the temperature of 680 °C, an oxygen pressure of 7 Pa, laser energy of 300 mJ, and repetition rate of 4 Hz were used, while the temperature of 700 °C, an oxygen pressure of 10 Pa, laser energy of 350 mJ and repetition rate of 4 Hz were used when depositing PTO and STO films. After films deposition, the samples were preserved at 700 °C for 5 min in an oxygen pressure of  $3 \times 10^4$  Pa, and then cooled down to 25 °C with the rate of 5 °C min<sup>-1</sup>.

**X-Ray Diffraction Analysis:** X-ray diffraction (XRD) measurements of  $\theta-2\theta$  scan and reciprocal space mapping (RSM) were used to test the crystalline quality of PTO/STO bilayers and (PTO/STO)<sub>5</sub> multilayered films, which was performed by Malvern PANalytical Xpert<sup>3</sup> MRD X-ray diffractometer.

**TEM Samples Preparation, HAADF-STEM Imaging, In Situ TEM and Atomic-Scale STEM Imaging:** The cross-sectional samples for STEM observations and in situ (S)TEM experiments were prepared by mechanical method of gluing, grinding, dimpling, and final ion milling. Before ion milling, the samples were dimpled down to 10 μm by Gatan Dimpling Grinder 656. When ion milling, a voltage of 4.5 kV and an angle of 7° were used at first by Gatan Precision Ion Polishing System 695. Then the voltage and angle gradually reduced in the milling process. The final voltage of 0.5 kV was used to reduce the amorphous at the surface of samples, which was generated by ion beam damage.

The statically cross-sectional HAADF-STEM images were recorded by a double aberration-corrected scanning transmission electron microscope (Spectra 300 X-FEG microscope, ThermoFisher Scientific) at 300 kV. To reduce the drift of STEM imaging, the atomic-scale HAADF-STEM images for extracting the polarization maps were acquired by STEM Drift Corrected Frame Integration (DCFI).<sup>[43,44]</sup> Each atomic-scale HAADF-STEM image was acquired by adding up 20 original images with the dwell time of 200 ns, which was performed by using the Velox software (Thermo Fisher Scientific).

The in situ TEM and STEM experiments under external electric fields were carried out on an aberration-corrected JEOL ARM 300F2 microscope with an in situ double-tilt electric bias TEM holder (Zeptools Technology). The dark-field TEM images and in situ video under external electric field were recorded in the microscope under TEM mode with OneView camera (Gatan). The recording parameters for in situ video were 1024 × 1024 pixel for each frame and 10 frames s<sup>-1</sup>. The atomic-scale HAADF-STEM images were acquired in the microscope under STEM mode with the recorded parameters of 2048 × 2048 pixel for each frame and the dwell time of 2 μs for each pixel.

**The Strain Analysis and Determining the Position of Atom Columns:** The large-scale strain field in HAADF-STEM images were deduced by Geometric Phase Analysis (GPA), which is an effective tool to determine lattice variation from HAADF-STEM images.<sup>[45,46]</sup> The process was carried out by Gatan Digital Micrograph software. The positions of atom columns in atomic-scale HAADF-STEM images were determined based on the 2D Gaussian fitting, which was carried out by using the Matlab software.<sup>[47]</sup>

**Phase Field Modeling:** In the phase field model, the three components of the polarization were chosen as the order parameters. The optimal polarization configuration under certain condition is obtained by solving the time-dependent Ginzburg–Landau (TDGL) equation:

$$\frac{\partial P_i(x, t)}{\partial t} = -L \frac{\delta F}{\delta P_i(x, t)}, \quad (i = 1, 2, 3) \quad (2)$$

where  $L$  is the kinetic coefficient and  $F$  is the total free energy of the system, which consists of the bulk energy, the gradient energy, the elastic energy, and the electrostatic energy:

$$F = \int_V \left[ f_{\text{bulk}}(P_i) + f_{\text{grad}}(P_{i,j}) + f_{\text{elas}}(P_i, \epsilon_{kl}) + f_{\text{elec}}(P_i, E_i) \right] dV \quad (3)$$

The dimension of the model is chosen to be  $200\Delta x \times 2\Delta y \times 80\Delta z$ , where  $\Delta x = \Delta y = 0.4$  nm, and  $\Delta z = 0.2$  nm, which correspond to the actual dimensions of  $80 \times 0.8 \times 16$  nm<sup>3</sup>. The thickness of the PTO layer is 8 nm, and the thickness of each STO layer is 4 nm. All material coefficients of PbTiO<sub>3</sub> and SrTiO<sub>3</sub> are adopted from a previous literature.<sup>[48]</sup>

### Supporting Information

Supporting Information is available from the Wiley Online Library or from the author.

## Acknowledgements

This work is supported by the Guangdong Basic and Applied Basic Research Foundation (No. 2023A1515011058), Guangdong Provincial Quantum Science Strategic Initiative (Nos. GDZX2202001 and GDZX2302001), and the National Natural Science Foundation of China (Nos. 52122101, 52471022, and 51971223). Y.J.W. acknowledges the Youth Innovation Promotion Association CAS (No. 2021187). Y.L.T. acknowledges the IMR Innovation Fund (2024-ZD01).

## Conflict of Interest

The authors declare no conflict of interest.

## Data Availability Statement

The data that support the findings of this study are available from the corresponding author upon reasonable request.

## Keywords

external stimuli, ferroelectric thin films, in situ transmission electron microscopy, reversible transition, topological domains

Received: September 23, 2024

Revised: December 9, 2024

Published online:

- [1] J. F. Scott, *Science* **2007**, *315*, 954.
- [2] S. Das, A. Ghosh, M. R. McCarter, S.-L. Hsu, Y.-L. Tang, A. R. Damodaran, R. Ramesh, L. W. Martin, *APL Mater.* **2018**, *6*, 100901.
- [3] S. Chen, S. Yuan, Z. Hou, Y. Tang, J. Zhang, T. Wang, K. Li, W. Zhao, X. Liu, L. Chen, L. W. Martin, Z. Chen, *Adv. Mater.* **2020**, *33*, 2000857.
- [4] Y. L. Tang, Y. L. Zhu, X. L. Ma, *J. Appl. Phys.* **2021**, *129*, 200904.
- [5] I. I. Naumov, L. Bellaiche, H. Fu, *Nature* **2004**, *432*, 737.
- [6] J. Ma, J. Ma, Q. Zhang, R. Peng, J. Wang, C. Liu, M. Wang, N. Li, M. Chen, X. Cheng, P. Gao, L. Gu, L. Q. Chen, P. Yu, J. Zhang, C. W. Nan, *Nat. Nanotechnol.* **2018**, *13*, 947.
- [7] J. Íñiguez, P. Zubko, I. Luk'yanchuk, A. Cano, *Nat. Rev. Mater.* **2019**, *4*, 243.
- [8] S. D. Salahuddin, S. Datta, *Nano Lett.* **2008**, *8*, 405.
- [9] Y. L. Tang, Y. L. Zhu, X. L. Ma, A. Y. Borisevich, A. N. Morozovska, E. A. Eliseev, W. Y. Wang, Y. J. Wang, Y. B. Xu, Z. D. Zhang, S. J. Pennycook, *Science* **2015**, *348*, 547.
- [10] A. K. Yadav, C. T. Nelson, S. L. Hsu, Z. Hong, J. D. Clarkson, C. M. Schlepütz, A. R. Damodaran, P. Shafer, E. Arenholz, L. R. Dedon, D. Chen, A. Vishwanath, A. M. Minor, L. Q. Chen, J. F. Scott, L. W. Martin, R. Ramesh, *Nature* **2016**, *530*, 198.
- [11] S. Das, Y. L. Tang, Z. Hong, M. A. P. Gonçalves, M. R. McCarter, C. Klewe, K. X. Nguyen, F. Gómez-Ortiz, P. Shafer, E. Arenholz, V. A. Stoica, S. L. Hsu, B. Wang, C. Ophus, J. F. Liu, C. T. Nelson, S. Saremi, B. Prasad, A. B. Mei, D. G. Schlom, J. Íñiguez, P. García-Fernández, D. A. Muller, L. Q. Chen, J. Junquera, L. W. Martin, R. Ramesh, *Nature* **2019**, *568*, 368.
- [12] Y. J. Wang, Y. P. Feng, Y. L. Zhu, Y. L. Tang, L. X. Yang, M. J. Zou, W. R. Geng, M. J. Han, X. W. Guo, B. Wu, X. L. Ma, *Nat. Mater.* **2020**, *19*, 881.
- [13] J. Wang, D. Liang, J. Ma, Y. Fan, J. Ma, H. M. Jafri, H. Yang, Q. Zhang, Y. Wang, C. Guo, S. Dong, D. Liu, X. Wang, J. Hong, N. Zhang, L. Gu, D. Yi, J. Zhang, Y. Lin, L.-Q. Chen, H. Huang, C.-W. Nan, *Nat. Commun.* **2023**, *14*, 3941.
- [14] Y. J. Wang, Y. P. Feng, Y. L. Tang, Y. L. Zhu, Y. Cao, M. J. Zou, W. R. Geng, X. L. Ma, *Nat. Commun.* **2024**, *15*, 3949.
- [15] W. R. Geng, X. W. Guo, H. L. Ge, Y. L. Tang, Y. L. Zhu, Y. J. Wang, B. Wu, M. J. Zou, Y. P. Feng, X. L. Ma, *Nano Lett.* **2022**, *22*, 8892.
- [16] A. R. Damodaran, J. D. Clarkson, Z. Hong, H. Liu, A. K. Yadav, C. T. Nelson, S. L. Hsu, M. R. McCarter, K. D. Park, V. Kravtsov, A. Farhan, Y. Dong, Z. Cai, H. Zhou, P. Aguado-Puente, P. Garcia-Fernandez, J. Iniguez, J. Junquera, A. Scholl, M. B. Raschke, L. Q. Chen, D. D. Fong, R. Ramesh, L. W. Martin, *Nat. Mater.* **2017**, *16*, 1003.
- [17] V. A. Stoica, N. Laanait, C. Dai, Z. Hong, Y. Yuan, Z. Zhang, S. Lei, M. R. McCarter, A. Yadav, A. R. Damodaran, S. Das, G. A. Stone, J. Karapetrova, D. A. Walko, X. Zhang, L. W. Martin, R. Ramesh, L. Q. Chen, H. Wen, V. Gopalan, J. W. Freeland, *Nat. Mater.* **2019**, *18*, 377.
- [18] K. Du, M. Zhang, C. Dai, Z. N. Zhou, Y. W. Xie, Z. H. Ren, H. Tian, L. Q. Chen, G. Van Tendeloo, Z. Zhang, *Nat. Commun.* **2019**, *10*, 4864.
- [19] P. Chen, X. Zhong, J. A. Zorn, M. Li, Y. Sun, A. Y. Abid, C. Ren, Y. Li, X. Li, X. Ma, J. Wang, K. Liu, Z. Xu, C. Tan, L. Chen, P. Gao, X. Bai, *Nat. Commun.* **2020**, *11*, 1840.
- [20] X. Li, C. Tan, C. Liu, P. Gao, Y. Sun, P. Chen, M. Li, L. Liao, R. Zhu, J. Wang, Y. Zhao, L. Wang, Z. Xu, K. Liu, X. Zhong, J. Wang, X. Bai, *Proc. Natl. Acad. Sci.* **2020**, *117*, 18954.
- [21] P. Chen, C. Tan, Z. Jiang, P. Gao, Y. Sun, L. Wang, X. Li, R. Zhu, L. Liao, X. Hou, K. Qu, N. Li, X. Li, Z. Xu, K. Liu, W. Wang, J. Wang, X. Ouyang, X. Zhong, J. Wang, X. Bai, *Sci. China. Phys. Mech.* **2022**, *65*, 237011.
- [22] M. F. Guo, E. X. Xu, H. B. Huang, C. Q. Guo, H. T. Chen, S. L. Chen, S. He, L. Zhou, J. Ma, Z. H. Shen, B. Xu, D. Yi, P. Gao, C. W. Nan, N. D. Mathur, Y. Shen, *Nat. Commun.* **2024**, *15*, 348.
- [23] R. Zhu, Z. Jiang, X. Zhang, X. Zhong, C. Tan, M. Liu, Y. Sun, X. Li, R. Qi, K. Qu, Z. Liu, M. Wu, M. Li, B. Huang, Z. Xu, J. Wang, K. Liu, P. Gao, J. Wang, J. Li, X. Bai, *Phys. Rev. Lett.* **2022**, *129*, 107601.
- [24] Y.-T. Shao, S. Das, Z. Hong, R. Xu, S. Chandrika, F. Gómez-Ortiz, P. García-Fernández, L.-Q. Chen, H. Y. Hwang, J. Junquera, L. W. Martin, R. Ramesh, D. A. Muller, *Nat. Commun.* **2023**, *14*, 1355.
- [25] M. Li, T. Yang, P. Chen, Y. Wang, R. Zhu, X. Li, R. Shi, H.-J. Liu, Y.-L. Huang, X. Ma, J. Zhang, X. Bai, L.-Q. Chen, Y.-H. Chu, P. Gao, *Nat. Commun.* **2022**, *13*, 6340.
- [26] A. Chaudron, Z. Li, A. Finco, P. Marton, P. Dufour, A. Abdelsamie, J. Fischer, S. Collin, B. Dkhil, J. Hlinka, V. Jacques, J.-Y. Chauleau, M. Viret, K. Bouzehouane, S. Fusil, V. Garcia, *Nat. Mater.* **2024**, *23*, 905.
- [27] Y. L. Tang, Y. L. Zhu, B. Wu, Y. J. Wang, L. X. Yang, Y. P. Feng, M. J. Zou, W. R. Geng, X. L. Ma, *Nano Lett.* **2021**, *21*, 6274.
- [28] S. L. Hsu, M. R. McCarter, C. Dai, Z. Hong, L. Q. Chen, C. T. Nelson, L. W. Martin, R. Ramesh, *Adv. Mater.* **2019**, *31*, 1901014.
- [29] M. Hadjimichael, Y. Li, E. Zatterin, G. A. Chahine, M. Conroy, K. Moore, E. N. O. Connell, P. Ondrejko, P. Marton, J. Hlinka, U. Bangert, S. Leake, P. Zubko, *Nat. Mater.* **2021**, *20*, 495.
- [30] S. Li, Y. L. Zhu, Y. J. Wang, Y. L. Tang, Y. Liu, S. R. Zhang, J. Y. Ma, X. L. Ma, *Appl. Phys. Lett.* **2017**, *111*, 052901.
- [31] L. Pintilie, I. Vrejoiu, D. Hesse, M. Alexe, *J. Appl. Phys.* **2008**, *104*, 114101.
- [32] R. Jacobs, J. Booske, D. Morgan, *Adv. Funct. Mater.* **2016**, *26*, 5471.
- [33] S. R. Spurgeon, J. D. Sloppy, D. M. Kepaptsoglou, P. V. Balachandran, S. Nejadi, J. Karthik, A. R. Damodaran, C. L. Johnson, H. Ambaye, R. Goyette, V. Lauter, Q. M. Ramasse, J. C. Idrobo, K. K. S. Lau, S. E. Lofland, J. M. Rondinelli, L. W. Martin, M. L. Taheri, *ACS Nano* **2014**, *8*, 894.
- [34] Z. Hong, A. R. Damodaran, F. Xue, S. L. Hsu, J. Britson, A. K. Yadav, C. T. Nelson, J. J. Wang, J. F. Scott, L. W. Martin, R. Ramesh, L. Q. Chen, *Nano Lett.* **2017**, *17*, 2246.
- [35] S. Choudhury, J. X. Zhang, Y. L. Li, L. Q. Chen, Q. X. Jia, S. V. Kalinin, *Appl. Phys. Lett.* **2008**, *93*, 162901.
- [36] Z. Hong, L.-Q. Chen, *Acta Mater.* **2018**, *152*, 155.
- [37] Z. Hong, S. Das, C. Nelson, A. Yadav, Y. Wu, J. Junquera, L.-Q. Chen, L. W. Martin, R. Ramesh, *Nano Lett.* **2021**, *21*, 3533.

- [38] L. Baudry, A. Sené, I. A. Luk'yanchuk, L. Lahoche, J. F. Scott, *Phys. Rev. B* **2014**, *90*, 024102.
- [39] A. Gruverman, D. Wu, H. J. Fan, I. Vrejoiu, M. Alexe, R. J. Harrison, J. F. Scott, *J. Phys.: Condens. Matter* **2008**, *20*, 342201.
- [40] P. Gao, C. T. Nelson, J. R. Jokisaari, S. H. Baek, C. W. Bark, Y. Zhang, E. Wang, D. G. Schlom, C. B. Eom, X. Pan, *Nat. Commun.* **2011**, *2*, 591.
- [41] M. Dawber, D. J. Jung, J. F. Scott, *Appl. Phys. Lett.* **2003**, *82*, 436.
- [42] C. Tan, Y. Dong, Y. Sun, C. Liu, P. Chen, X. Zhong, R. Zhu, M. Liu, J. Zhang, J. Wang, K. Liu, X. Bai, D. Yu, X. Ouyang, J. Wang, P. Gao, Z. Luo, J. Li, *Nat. Commun.* **2021**, *12*, 4620.
- [43] W. Weng, C. Ortolland, In European Microscopy Congress 2016: Proceedings, Wiley, New York, Chichester, UK **2016**.
- [44] L. Lu, Y. Nahas, M. Liu, H. Du, Z. Jiang, S. Ren, D. Wang, L. Jin, S. Prokhorenko, C. L. Jia, L. Bellaiche, *Phys. Rev. Lett.* **2018**, *120*, 177601.
- [45] M. J. Hytch, E. Snoeck, R. Kilaas, *Ultramicroscopy* **1998**, *74*, 131.
- [46] Y. L. Tang, Y. L. Zhu, X. L. Ma, *Ultramicroscopy* **2016**, *160*, 57.
- [47] S. M. Anthony, S. Granick, *Langmuir* **2009**, *25*, 8152.
- [48] S. Y. H. Y. L. Li, Z. K. Liu, L. Q. Chen, *Acta Mater.* **2002**, *50*, 17.

# Enhanced energy storage in antiferroelectrics via antipolar frustration

<https://doi.org/10.1038/s41586-024-08505-7>

Received: 28 May 2024

Accepted: 9 December 2024

Published online: 29 January 2025

 Check for updates

Bingbing Yang<sup>1,2,12</sup>, Yiqian Liu<sup>1,12</sup>, Ru-Jian Jiang<sup>3,4,12</sup>, Shun Lan<sup>1</sup>, Su-Zhen Liu<sup>3,4</sup>, Zhifang Zhou<sup>1</sup>, Lvye Dou<sup>1</sup>, Min Zhang<sup>1</sup>, Houbing Huang<sup>5</sup>, Long-Qing Chen<sup>6</sup>, Yin-Lian Zhu<sup>7,8</sup>, Shujun Zhang<sup>9,10</sup>, Xiu-Liang Ma<sup>7,10,11</sup>, Ce-Wen Nan<sup>1</sup> & Yuan-Hua Lin<sup>1,12</sup>

Dielectric-based energy storage capacitors characterized with fast charging and discharging speed and reliability<sup>1–4</sup> play a vital role in cutting-edge electrical and electronic equipment. In pursuit of capacitor miniaturization and integration, dielectrics must offer high energy density and efficiency<sup>5</sup>. Antiferroelectrics with antiparallel dipole configurations have been of significant interest for high-performance energy storage due to their negligible remanent polarization and high maximum polarization in the field-induced ferroelectric state<sup>6–8</sup>. However, the low antiferroelectric–ferroelectric phase-transition field and accompanying large hysteresis loss deteriorate energy density and reliability. Here, guided by phase-field simulations, we propose a new strategy to frustrate antipolar ordering in antiferroelectrics by incorporating non-polar or polar components. Our experiments demonstrate that this approach effectively tunes the antiferroelectric–ferroelectric phase-transition fields and simultaneously reduces hysteresis loss. In PbZrO<sub>3</sub>-based films, we hence realized a record high energy density among all antiferroelectrics of 189 J cm<sup>−3</sup> along with a high efficiency of 81% at an electric field of 5.51 MV cm<sup>−1</sup>, which rivals the most state-of-the-art energy storage dielectrics<sup>9–12</sup>. Atomic-scale characterization by scanning transmission electron microscopy directly revealed that the dispersed non-polar regions frustrate the long-range antipolar ordering, which contributes to the improved performance. This strategy presents new opportunities to manipulate polarization profiles and enhance energy storage performances in antiferroelectrics.

Electric energy storage devices with both high energy density and power density are highly desired for advanced electronics and electrical power systems. Electrostatic capacitors based on dielectrics are recognized to be one of the most promising energy storage devices owing to their fast charging and discharging speed and superior reliability<sup>1,2</sup>. However, the relatively low energy density of dielectrics has long been a bottleneck that hinders the downsizing of energy storage capacitors<sup>3,5,9</sup>. The primary performance metric is the recoverable energy density,  $U_e$ , given by  $U_e = \int_0^{P_m} E dP$  (Supplementary Fig. 1), in which  $P$  is the polarization,  $P_r$  and  $P_m$  are the remanent and maximum polarization, respectively, and  $E$  is the electric field. A small  $P_r$ , a large  $P_m$  and a high breakdown field strength ( $E_b$ ) are crucial for achieving a high  $U_e$ .

Thus far, nonlinear ferroelectric-based (FE-based) materials, including FEs, relaxor FEs and superparaelectrics have been extensively

investigated for dielectric energy storage due to their high polarization and reduced hysteresis. By carefully designing domain configurations and atomic structures, a high energy density beyond 130 J cm<sup>−3</sup> with an efficiency exceeding 75% has been achieved<sup>9,10</sup>. In addition to FE-based materials, antiferroelectrics (AFEs) are highly promising for energy storage because their unique double hysteresis loop inherently integrates many merits<sup>6,13,14</sup>: (1) antiparallel dipole configuration in an AFE state leads to a near-zero  $P_r$ ; (2) a field-induced polar FE state leads to a high  $P_m$ ; and (3) the electric-field-induced AFE–FE transition, bridging the two states, contributes to a concave polarization/depolarization process—all of these account for higher energy storage (Supplementary Fig. 1). However, the low field-induced phase-transition field (that is, the low AFE–FE transition field  $E_p$ ) and large switching hysteresis (that is, a large difference between the  $E_f$  and the FE–AFE transition field  $E_A$ ) pose challenges for further improving AFE performance.

<sup>1</sup>State Key Laboratory of New Ceramics and Fine Processing, School of Materials Science and Engineering, Tsinghua University, Beijing, China. <sup>2</sup>Key Laboratory of Materials Physics, Institute of Solid State Physics, HFIPS, Chinese Academy of Sciences, Hefei, China. <sup>3</sup>Shenyang National Laboratory for Materials Science, Institute of Metal Research, Chinese Academy of Sciences, Shenyang, China. <sup>4</sup>School of Materials Science and Engineering, University of Science and Technology of China, Shenyang, China. <sup>5</sup>Advanced Research Institute of Multidisciplinary Science, Beijing Institute of Technology, Beijing, China. <sup>6</sup>Department of Materials Science and Engineering, Materials Research Institute, The Pennsylvania State University, University Park, PA, USA. <sup>7</sup>Bay Area Center for Electron Microscopy, Songshan Lake Materials Laboratory, Dongguan, China. <sup>8</sup>School of Materials Science and Engineering, Hunan University of Science and Technology, Xiangtan, China. <sup>9</sup>Institute for Superconducting and Electronic Materials, Faculty of engineering and information science, University of Wollongong, Wollongong, New South Wales, Australia. <sup>10</sup>Institute of Physics, Chinese Academy of Sciences, Beijing, China. <sup>11</sup>Quantum Science Center of Guangdong-HongKong-Macau Greater Bay Area, Shenzhen, China. <sup>12</sup>These authors contributed equally: Bingbing Yang, Yiqian Liu, Ru-Jian Jiang. ✉e-mail: shujun@uow.edu.au; xлма@iphy.ac.cn; linyh@tsinghua.edu.cn

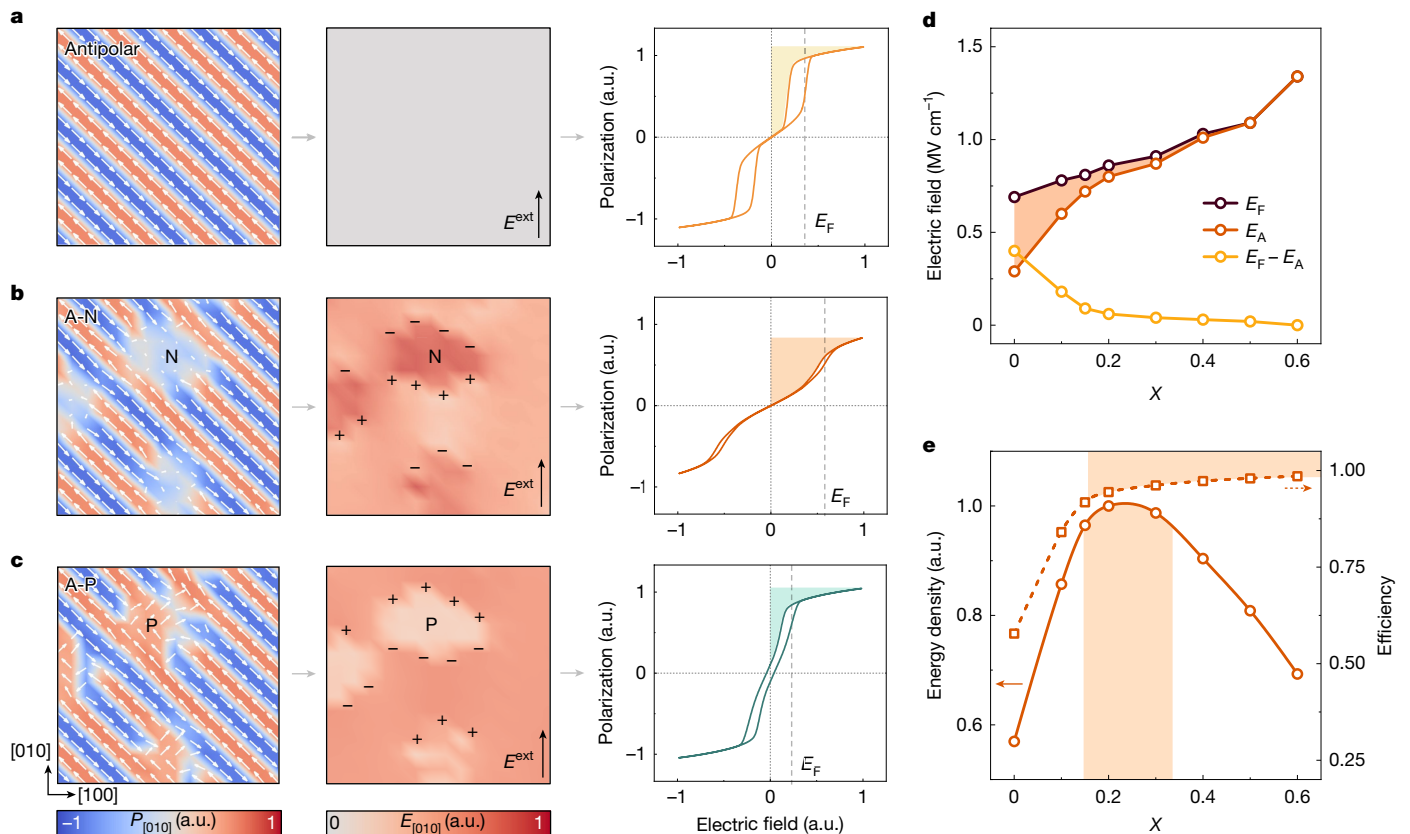


**Fig. 1 | Phase-field demonstration of antipolar ordering frustration.** **a–c**, Schematic polarization configuration (left), simulated electric field distribution (middle) and  $P-E$  loops (in arbitrary units (a.u.)) (right) for AFE (a), A-N type (b) and A-P type (c) structures. N means non-polar regions and P means polar regions. ‘+’ means positive bound charge and ‘-’ means negative bound charge. The external electric field  $E^{\text{ext}}$  is applied along [010] (arrows marked)

far lower than  $E_F$ . The plotted  $E_{[010]}$  is a sum of external field and internal field generated from bound charges. Shaded regions in  $P-E$  loops indicate the recoverable energy density. **d**, Calculated  $E_F$ ,  $E_A$  and  $E_F - E_A$  from simulated  $P-E$  loops for A-N type dielectrics, where the  $x$  is the mole fraction of non-polar contents. **e**, Calculated energy density  $U_e$  and efficiency  $\eta$  of A-N type dielectrics as a function of  $x$ .

In recent years, efforts have been made to address the drawbacks of AFEs. One approach involves using ion dopants and relaxor components to construct relaxor AFEs to reduce the polarization switching hysteresis<sup>13,15–18</sup>. Such a design is conducive to achieving higher energy storage efficiency ( $\eta$ ); for example,  $\eta > 90\%$  is obtained in relaxor AFE ( $\text{Pb}_{0.97}\text{La}_{0.02})(\text{Zr}_{0.55}\text{Sn}_{0.45})\text{O}_3$  (ref. 13). Another method focuses on decreasing the tolerance factor to enhance AFE stability and delay the transition field  $E_F$ , and hence realize a notable enhancement of  $U_e$  (refs. 19–21). For example, the  $U_e$  of  $\text{PbZrO}_3$ -based films increased more than threefold with a decreased tolerance factor<sup>19</sup>. More recently, a superlattice design was also employed to realize a higher  $U_e$  (approximately  $115 \text{ J cm}^{-3}$ ) and to scale up the capacitor volumetrically, compatible with current very large-scale integration processing<sup>5</sup>. Despite these advancements, the energy density of AFEs remains limited, which impedes their broader application. Therefore, it is imperative to design new approaches to simultaneously increase  $E_F$ , minimize hysteresis loss in AFEs and obtain a high overall energy storage performance.

### Theoretical demonstration of frustration in AFEs

It is generally accepted that the polarization behaviours in dielectrics are strongly linked to the dipole configurations<sup>9,22–24</sup>. Typically, the switching loss can be effectively tuned by means of domain engineering in relaxor FEs<sup>9,23</sup>. AFEs, on the other hand, are featured with a special long-range antiparallel dipole configuration. From an electrostatic perspective, frustrating such antipolar ordering can cause polarization discontinuity, leading to bound charges and the redistribution

of electric fields. Therefore, such a frustration effect can be utilized to manipulate the transition field and hysteresis loss in AFEs.

Here we constructed three types of AFE structures: an AFE with antipolar ordering (Fig. 1a), an AFE frustrated by non-polar components when alloyed with paraelectrics (A-N type, where A represents an AFE and N denotes a non-polar component, as shown in Fig. 1b) and an AFE frustrated by polar components when alloyed with FEs (A-P type, where P represents a polar component, as given in Fig. 1c). Polarization discontinuity is evident in the latter two cases. Using phase-field simulations incorporating the classical model of AFEs (details are in Methods), we investigated the electric field distributions and polarization–electric field ( $P-E$ ) loops in all three cases. For the AFE scenario, under an external electric field  $E^{\text{ext}}$  along [010], the long-range antipolar ordered AFE undergoes an AFE–FE transition with a uniform electric field application, yielding a typical double hysteresis loop (Fig. 1a). For the A-N type in Fig. 1b, the polarization in non-polar regions is less responsive and lags behind that in the antipolar region. This gives rise to bound charges at the non-polar/antipolar interface (Extended Data Fig. 1), which generate an internal field that enhances the external field in non-polar regions but offsets it in antipolar regions (Fig. 1b, middle), consequently delaying the AFE–FE transition by making antipolar regions less polarized and non-polar regions more polarized (Fig. 1b, right, and Extended Data Fig. 2). Upon removing the field, the non-polar regions can rapidly revert to their initial state, forcing switched antipolar regions back to the antipolar ordering under a charge-controlled process (Supplementary Fig. 2), which leads to a reduced hysteresis loss. Hence, the A-N design results in both an enlarged  $E_F$  and a reduced  $E_F - E_A$  simultaneously (Fig. 1b). It also implies a more stable AFE state

during the charging–discharging process due to the frustration of non-polar regions (Supplementary Fig. 3).

By contrast, for the A-P type shown in Fig. 1c, the existence of the spontaneous polarization in polar regions produces an inverse polarization gradient, and therefore the bound charges generate an internal electric field that polarizes antipolar regions while inhibiting further polarizing of polar regions (Fig. 1c (middle) and Extended Data Fig. 1). This facilitates the AFE–FE transition (Fig. 1c (right) and Extended Data Fig. 3). Upon discharge, the polar regions maintain a remanent polarization, causing a decreased  $E_A$  and an inevitable large hysteresis. The A-P design decreases  $E_F$  while maintaining a large  $E_F - E_A$  (Fig. 1c), indicating a less stable AFE state due to the frustration of polar regions (Supplementary Fig. 4).

Therefore, the frustration of the long-range antipolar ordering by non-polar/polar components can effectively tune the AFE–FE transition field and the hysteresis. Considering that the enlarged  $E_F$  and suppressed hysteresis loss in an A-N type AFE, a high energy storage performance is expected.

To quantitatively reveal the evolution of  $E_F$  and  $E_F - E_A$  in frustrated AFEs and identify an optimal composition  $(1-x)$ A- $x$ N for energy storage, we calculated the transition fields from a series of  $P$ – $E$  loops (Supplementary Fig. 5 and Methods), which are shown in Fig. 1d. With an increase in the non-polar content  $x$ , the  $E_F$  increases and the  $E_F - E_A$  decreases monotonously, which contributes to an enhanced energy density  $U_e$  and efficiency  $\eta$  (Fig. 1e). However,  $U_e$  decreases with a higher  $x$  because excessive non-polar components can deteriorate polarization. An  $x$  of approximately 0.15–0.35 is suitable for obtaining an optimal  $U_e$  with a high  $\eta$ . The transition field and  $P$ – $E$  loops for A-P type dielectrics were also calculated and given in Supplementary Fig. 6. The AFE fingerprints disappear at around  $x = 0.2$ , making them unsuitable for energy storage.

## Experimental construction of frustrated AFEs

Experimentally, we selected the most typical AFE  $\text{PbZrO}_3$  as the antipolar matrix. Considering that antipolar frustration may sacrifice the polarization values, we initially employed Hf substitution, which was previously reported to increase the polarization of  $\text{PbZrO}_3$  (refs. 25,26). An enhanced polarization and permittivity can be observed in the  $\text{PbZr}_{0.925}\text{Hf}_{0.075}\text{O}_3$  (PZH) composition (Supplementary Fig. 7), which is an ideal pristine AFE platform. Guided by theoretical phase-field simulations, we designed a comparative experiment incorporating a non-polar paraelectric,  $\text{LaScO}_3$  (LS), and a polar FE,  $\text{Na}_{0.5}\text{Bi}_{0.5}\text{TiO}_3$  (NBT), respectively. A series of PZH-based films, namely, A-N type  $(1-x)$ PZH- $x$ LS and A-P type  $(1-y)$ PZH- $y$ NBT were prepared onto  $\text{LaNiO}_3$  buffered  $\text{LaAlO}_3$  substrates (Methods). X-ray diffraction was performed to identify the phase structure, and the results indicate that single-phase A-N and A-P solid-solution films were successfully obtained (Extended Data Fig. 4).

We measured the  $P$ – $E$  loops for the  $(1-x)$ PZH- $x$ LS and  $(1-y)$ PZH- $y$ NBT films. The pristine PZH film possesses a typical AFE double hysteresis loop with a transition field  $E_F$  at approximately  $0.68 \text{ MV cm}^{-1}$  (Fig. 2a,e). With the addition of LS in the  $(1-x)$ PZH- $x$ LS films, as shown in Fig. 2a, the  $E_F$  becomes higher in magnitude and the switching hysteresis loss decreases. With the  $x$  further increased to 0.5, the  $P$ – $E$  loop becomes linear like. Such a trend is more clearly displayed in the electric-field-dependent permittivity ( $dP/(dE \times \epsilon_0)$ , where  $\epsilon_0$  is the vacuum permittivity) and switching current density curves (Fig. 2b and Supplementary Fig. 8a), where the permittivity and current peaks correspond to the higher  $E_F$  and lower  $E_A$ , respectively, as summarized in Fig. 2c. Remarkably, the A-N design enhances both of the transition fields  $E_F$  and  $E_A$  and suppresses the switching hysteresis  $E_F - E_A$ . Conversely, in the  $(1-y)$ PZH- $y$ NBT films, an increase in NBT content induces the  $E_F$  and  $E_A$  shift to lower values, and the AFE polarization behaviours eventually transit to relaxor FEs, losing the double hysteresis loops (Fig. 2e–g and Supplementary Fig. 8b). Based on the above results, we

claim that the antipolar ordering frustration design can effectively tune the AFE–FE transition fields and switching hysteresis, which is highly consistent with phase-field simulations.

We subsequently calculated the energy density  $U_e$  and efficiency  $\eta$  for  $(1-x)$ PZH- $x$ LS and  $(1-y)$ PZH- $y$ NBT films. For the A-N type,  $U_e$  is initially enhanced when  $x$  is increased to 0.2, due to the enlarged  $E_F$  and reduced  $E_F - E_A$ , and then it decreases because of the sacrificed polarization, whereas  $\eta$  monotonously increases. The highest  $U_e$  of  $58 \text{ J cm}^{-3}$  with a high  $\eta$  of 86% is obtained when  $x = 0.2$  (Fig. 2d), which is consistent with phase-field simulations (Supplementary Fig. 9). By contrast, for the A-P type, with an increase in  $y$ , the  $U_e$  and  $\eta$  initially decrease, because of the reduced  $E_F$ , and then show an increasing trend as  $y$  further increases due to the transition from AFE to relaxor FE. Note that the  $U_e$  and  $\eta$  of A-P type are lower than those of A-N type, demonstrating the superiority of the A-N design for higher energy storage performance. This type of material is the main focus hereafter.

## Visualization of frustrated antipolar ordering

As in phase-field simulations, antipolar ordering frustrated by non-polar regions serves as the structural foundation for achieving high energy storage performance. To validate this point, we conducted the high-angle angular dark-field aberration-corrected scanning transmission electron microscopy (HAADF-STEM) characterization on  $(1-x)$ PZH- $x$ LS films to directly reveal polarization configurations. Figure 3a and Extended Data Fig. 5a,c present the atomic-scale HAADF-STEM image and the corresponding selected area electron diffraction (SAED) pattern for PZH film with  $x = 0$ . In addition to the strong peaks along [001] and [010], additional diffraction points along [011] and [0–11] marked by red arrows are also observed, demonstrating an orthorhombic structure of PZH<sup>27,28</sup>. Moreover, superlattice diffraction points located at  $1/3\{011\}$  and  $2/3\{011\}$  (marked by red arrows) are observed, suggesting a polarization modulation with a threefold period, as illustrated in the inset of Fig. 3a (the green box)<sup>27,29</sup>. The polarization mapping was characterized based on the projected displacement of A-site cations (Pb) relative to their four nearest B-site cations (Zr/Hf), revealing the antiparallel arranged dipoles with up-down-down modulations (Fig. 3d and enlarged as shown in the inset d1), corresponding to the distinct superlattice diffraction points in Fig. 3a. We also analysed the polarization structure by extracting the distribution of the horizontal lattice rotation ( $R_\alpha$ ) along the [010]<sub>pc</sub> direction (where ‘pc’ represents the pseudocubic unit cell) (Fig. 3g and Methods)<sup>27</sup>. The periodic  $R_\alpha$  is consistent with the polarization mapping (Fig. 3d), demonstrating a long-range antipolar ordering in PZH film.

In  $(1-x)$ PZH- $x$ LS film with  $x = 0.2$ , the superlattice diffraction points become weaker (Fig. 3b and Extended Data Fig. 5b,d), suggesting the frustration of antipolar ordering. Such a scenario can be further confirmed by the corresponding fast Fourier transform images: although typical bright superlattice diffraction points are present in some regions, for example b1, they are absent in some other regions, for example b2 (Fig. 3b), suggesting the coexistence of antipolar and non-polar regions. We also characterized the polarization mapping for the film with  $x = 0.2$  (Fig. 3e). The regions outlined by brown dashed lines exhibit a disordered polarization direction with a nearly zero magnitude (zoomed-in view in Fig. 3e2), which confirms a non-polar feature, whereas, for the remaining regions, the AFE characteristic with antiparallel dipoles is still sustained (zoomed-in view in Fig. 3e1). These results demonstrate that the long-range antipolar ordering is broken by randomly distributed non-polar regions in the A-N design, resonating with phase-field simulations, and thus contributes to an enlarged phase-transition field  $E_F$  and reduced polarization hysteresis. Such a frustrated polarization configuration is also visibly evident in the corresponding  $R_\alpha$  map where periodically modulated  $R_\alpha$  and disordered  $R_\alpha$  coexist (Fig. 3h).

When  $x$  is further increased to 0.5, the superlattice diffraction points disappear (Fig. 3c), indicating the absence of antipolar ordering.

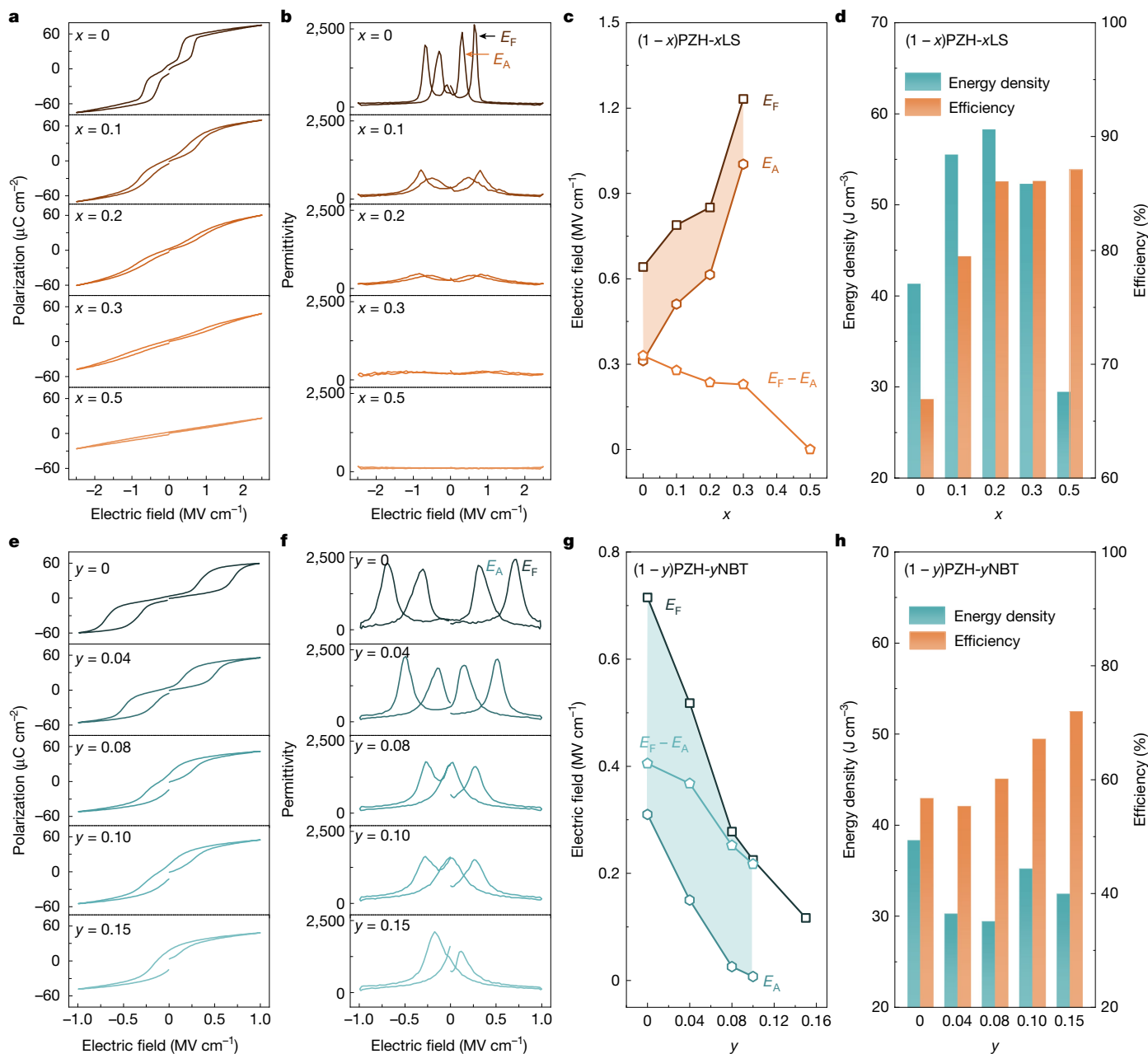


**Fig. 2 | Validating the efficacy of the frustration design experimentally on regulating transition field and switching hysteresis in  $(1-x)$ PZH- $x$ LS and  $(1-y)$ PZH- $y$ NBT films. a–c,  $P$ - $E$  loops (a), electric-field-dependent permittivity (b) and composition-dependent  $E_F$ ,  $E_A$  and  $E_F - E_A$  (c) as a function of  $x$  for the  $(1-x)$ PZH- $x$ LS films at an electric field of  $2.5 \text{ MV cm}^{-1}$ . d, Evolution of energy density and efficiency as a function of  $x$  at an electric field of**

**$2.5 \text{ MV cm}^{-1}$  for the  $(1-x)$ PZH- $x$ LS films. e–g,  $P$ - $E$  loops (e), electric-field-dependent permittivity (f) and composition-dependent  $E_F$ ,  $E_A$  and  $E_F - E_A$  (g) as a function of  $y$  for the  $(1-y)$ PZH- $y$ NBT films at an electric field of  $1.0 \text{ MV cm}^{-1}$ . h, Evolution of energy density and efficiency as a function of  $y$  at an electric field of  $2.5 \text{ MV cm}^{-1}$  for the  $(1-y)$ PZH- $y$ NBT films.**

Figure 3f displays the polarization mapping for the film with  $x = 0.5$ . The entire region shows a nearly completely disordered polarization direction with an almost zero polarization magnitude (zoomed-in view in Fig. 3f1). Additionally, there is no periodically modulated  $R_w$ , which implies the destruction of antipolar ordering, leading to a linear-like  $P$ - $E$  loop.

Based on the above results, we can claim that, by the A-N design, we effectively frustrated the long-range antipolar ordering which is thus responsible for the high energy storage performance. In addition, Extended Data Fig. 6 exhibits atomically resolved elemental mapping for the film with  $x = 0.2$ . All elements exhibit a random distribution in lattice sites without aggregation. This confirms that the frustration arises from polarization inhomogeneity rather than phase separation

and is related to local compositional fluctuations<sup>22,30</sup> (Supplementary Fig. 10).

### Excellent energy storage performance

By the design of frustrating antipolar ordering in AFEs, we demonstrate the advantages of high energy storage benefiting from the controllable phase-transition fields and hysteresis. To further evaluate the full potential of  $(1-x)$ PZH- $x$ LS films in energy storage application, the statistical value of  $E_b$  was obtained by the two-parameter Weibull distribution (Fig. 4a). The value of  $E_b$  gradually increases from  $3.91 \text{ MV cm}^{-1}$  to  $5.51 \text{ MV cm}^{-1}$  when  $x$  is increased to 0.2 owing to the decreased probability of electromechanical and electrical breakdown. In AFEs, the

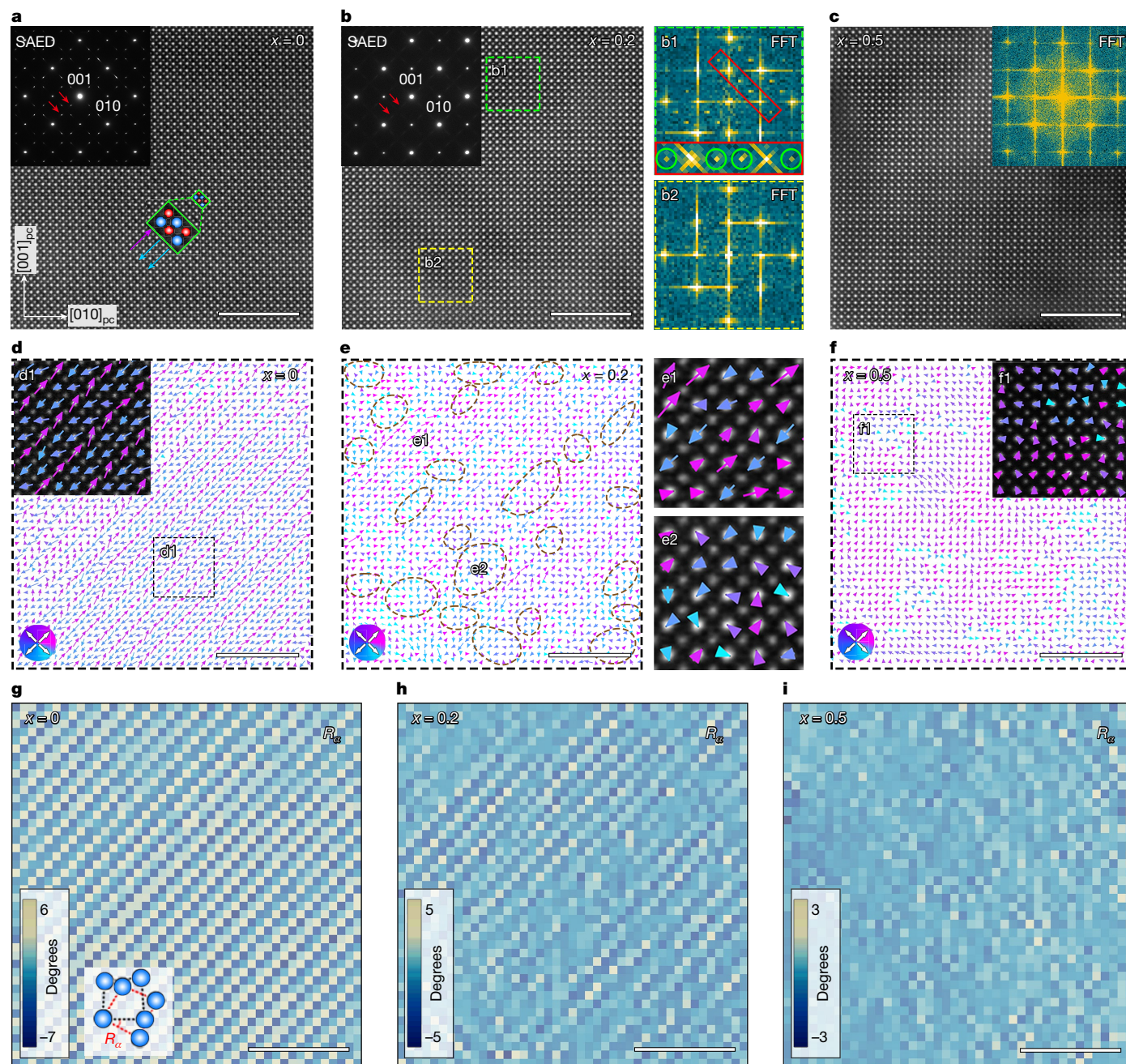


**Fig. 3 | Atomically resolved frustrated antipolar ordering in (1-x)PZH-xLS films. a-c**, Atomic-scale HAADF-STEM images for the films with  $x=0$  (a), 0.2 (b) and 0.5 (c). The insets show the SAED and fast Fourier transform (FFT) patterns. **d-f**, Pb/La cation displacement vector maps for the films with  $x=0$  (d), 0.2 (e) and 0.5 (f), from the corresponding HAADF-STEM images. The insets of **d** and **f**

display the zoomed-in views in the marked black box. Regions outlined by brown dashed lines in **e** delineate non-polar regions. **g-i**, Maps of the horizontal lattice rotation angle extracted from **a-c** for the films with  $x=0$  (**g**), 0.2 (**h**) and 0.5 (**i**). The inset in **g** is the definition of  $R_\alpha$ , where  $+R_\alpha$  denotes an anticlockwise lattice rotation and  $-R_\alpha$  denotes a clockwise lattice rotation. Scale bars, 5 nm.

field-induced phase transition usually involves a large volume change, which can mechanically degrade the breakdown field<sup>7,31</sup>. With the introduction of LS, the phase transition becomes more diffused and smeared with a stronger relaxor feature (Supplementary Fig. 11), leading to a greatly decreased phase-transition-induced volume change together with weakened electrostrains (Supplementary Fig. 12). Additionally, with the introduction of LS, the permittivity decreases because of the existing non-polar regions (Supplementary Fig. 11), which weakens local electric field and bond distortion. Therefore, the electromechanical breakdown is largely inhibited<sup>2</sup>. Moreover, compared with the film with  $x=0$ , the band gap increases in the film with  $x=0.2$  (Supplementary Fig. 13), accounting for the greatly suppressed leakage current

(Supplementary Fig. 14). Consequently, the electrical breakdown probability decreases, which further contributes to a high breakdown field. As  $x$  is further increased to 0.3 and 0.5, the  $E_b$  tends to decline, which is potentially due to the deteriorated film quality from the excessive addition of LS composition (Supplementary Fig. 15). In addition, we observed that the Weibull modulus  $\beta$  monotonously increases from 6.5 ( $x=0$ ) to 11.7 ( $x=0.2$ ) and to 14.6 ( $x=0.5$ ) as  $x$  increases, which implies a more concentrated distribution and an enhanced reliability of  $E_b$  (ref. 12).

The energy density and efficiency were calculated based on the bipolar  $P-E$  loops up to  $E_b$  (Extended Data Fig. 7). The film with  $x=0$  shows a relatively low  $U_c$  of 67 J cm<sup>-3</sup> and an inferior  $\eta$  of 66% due to the small  $E_r$  and large hysteresis loss (Fig. 4b). With the addition of LS, the  $U_c$  is

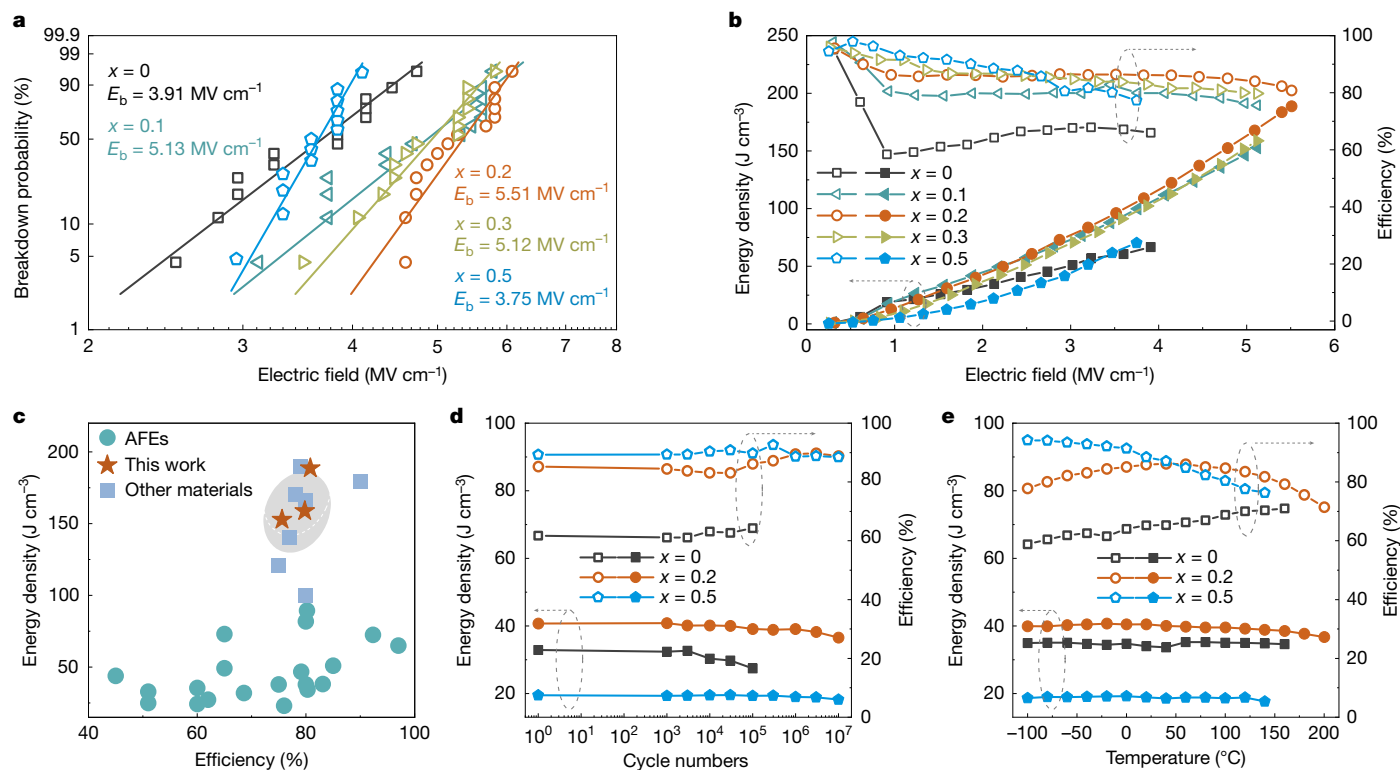


**Fig. 4 | Energy storage performance of (1 - x)PZH.xLS films. a**, Determination of the  $E_b$  by the two-parameter Weibull distribution. **b**, Electric-field-dependent energy density and efficiency. **c**, Comparison of energy density and efficiency of AFE films in this work with state-of-the-art AFE materials and other material

systems with ultrahigh energy storage performances. **d**, Energy storage performance variations as a function of charging-discharging cycle numbers. **e**, Energy storage performance variations as a function of temperature.

substantially enhanced due to the synergy of the delayed field-induced phase transition, minimized hysteresis loss and large  $E_b$ . An ultrahigh  $U_e$  of  $189 \text{ J cm}^{-3}$  is achieved for the PZH-LS film with  $x = 0.2$  (Fig. 4b and Supplementary Fig. 16), which is nearly three times enhanced compared with the film with  $x = 0$ . The films with  $x = 0.1$  and  $0.3$  also exhibit high  $U_e$  values of  $153$  and  $159 \text{ J cm}^{-3}$ , respectively (Fig. 4b). Moreover, a substantial enhancement of  $\eta$  is realized, with  $\eta$  value exceeding 80% over the entire electric field range in the film with  $x = 0.2$ . In short, by the antipolar ordering frustration, we achieved simultaneous improvements in both  $U_e$  of  $189 \text{ J cm}^{-3}$  and  $\eta$  of 81% in AFEs, which are superior to the values of all reported AFE materials (Fig. 4c)<sup>13-17,19-21,32-43</sup> and also rival the most state-of-the-art energy storage dielectrics (Fig. 4c)<sup>9-12,30,44,45</sup>, such as superparaelectrics, with  $U_e$  of  $152 \text{ J cm}^{-3}$  and  $\eta$  of 77% (ref. 30), and relaxor ferroelectrics, with  $U_e$  of  $133 \text{ J cm}^{-3}$  and  $\eta$  of 75% (ref. 10). In addition, such a high energy storage performance can be sustained in the films with larger area (Extended Data Fig. 8).

The cycling reliability and temperature stability of energy storage performance are crucial for the practical application of dielectric capacitors. Considering that capacitors are typically rated at 33–40% of their breakdown voltages to ensure safe operation in practical applications, we adopted electric fields of  $2.00 \text{ MV cm}^{-1}$  (about 36% of  $E_b$ ) for cycling and temperature stability tests. According to the  $P$ - $E$  loops after different cycle numbers (Supplementary Fig. 17), we calculated the energy density and efficiency, as presented in Fig. 4d and Extended Data Fig. 9a. The film with  $x = 0$  breaks down after  $1 \times 10^5$  cycle numbers, whereas the films with  $x = 0.2$  and  $0.5$  demonstrate significantly enhanced charging-discharging lifetimes, surviving up to  $1 \times 10^7$  cycles with a fluctuation of  $U_e < 8\%$  and  $\eta < 18\%$  (Fig. 4d). This indicates enhanced cycling reliability. The improved service lifetime is related to reduced hysteresis loss and electrostrains. In AFEs, large switching hysteresis induces an incompatible AFE and FE transition, leading to a large volume change and cracks that initiate and propagate

during repeated forward and reverse transitions, ultimately causing dielectric capacitor failure<sup>46,47</sup>. With increasing  $x$ , the phase transition becomes more diffused with a reduced polarization hysteresis, facilitating more compatible AFE and FE phases. The temperature stability was also evaluated across a wide temperature range from  $-100$  to  $200 \text{ }^\circ\text{C}$ . We measured the  $P$ - $E$  loops at different temperatures (Supplementary Fig. 18) and calculated the performance variations, as given in Fig. 4e and Extended Data Fig. 9b. We observed that the film with  $x = 0$  fails at the temperature of  $160 \text{ }^\circ\text{C}$ . With the addition of LS, films can withstand temperatures beyond  $200 \text{ }^\circ\text{C}$  because of more temperature-insensitive dielectric characteristics and an enhanced breakdown strength<sup>30,48</sup>. The film with  $x = 0.2$  shows a stable performance with a fluctuation of  $U_e < 10\%$  and  $\eta < 18\%$  over the entire temperature range studied. The high energy density of approximately  $37 \text{ J cm}^{-3}$  at  $200 \text{ }^\circ\text{C}$  is superior to the polymer dielectrics ( $U_e < 10 \text{ J cm}^{-3}$ ) (refs. 49,50). As for the film with  $x = 0.5$ , the temperature stability decreases with a large deterioration in  $\eta$  of approximately 18% and the film breaks down at  $140 \text{ }^\circ\text{C}$ , which can be ascribed to the increased leakage current.

Furthermore, the higher electric field cycling reliability and temperature stability for the film with  $x = 0.2$  were also evaluated at  $3.0$  to  $5.0 \text{ MV cm}^{-1}$ . The film maintained good performance reliability up to  $1 \times 10^6$  cycles at electric fields of  $3.0$  and  $4.0 \text{ MV cm}^{-1}$  (Extended Data Fig. 9c and Supplementary Fig. 19). However, the fatigue endurance dropped at higher electric fields of  $5.0 \text{ MV cm}^{-1}$ , which is generally expected, as a higher electric field activates more carriers, increasing the likelihood of accumulative breakdown<sup>10,12</sup>. In addition, it was found that the films can still hold a relatively high energy density up to  $150 \text{ }^\circ\text{C}$  at electric fields of  $3.0$  and  $4.0 \text{ MV cm}^{-1}$  (Extended Data Fig. 9d and Supplementary Fig. 20), demonstrating good temperature stability. It is noted that the energy storage efficiency shows a relatively larger decline with the increased electric field, and the film breaks down up to  $80 \text{ }^\circ\text{C}$  at an electric field of  $5.0 \text{ MV cm}^{-1}$ , which should be linked to the

thermally stimulated conduction loss<sup>12</sup>. The enhanced cycling reliability and temperature stability for the film with  $x = 0.2$  make it suitable for applications in harsh working conditions. To consider the prospects of the dielectric capacitors for pulsed-power applications, we measured the overdamped discharging performance at electric fields of 3.0 to 5.0 MV cm<sup>-1</sup> with a load resistor (20 kΩ) for the film with  $x = 0.2$  (Extended Data Fig. 10). A high discharge energy density of 121 J cm<sup>-3</sup> with an ultrafast discharge speed ( $t_{0.9}$ ) of 3.2 μs was obtained, indicating promising performance in pulsed-power equipment.

## Conclusion

In summary, we demonstrated that the antipolar ordering frustration strategy in classic perovskite PbZrO<sub>3</sub>-based AFE materials can substantially delay the  $E_F$  and suppress the hysteresis during the phase transition, which remarkably boosts the overall energy storage performance. It unlocks an untapped pathway to flexibly tune polarization profiles and field-induced phase transition of AFEs, which is useful not only for energy storage but also for piezoelectrics, electrocalorics and so on. Moreover, the polarization discontinuity arising from order frustration also offers a constructive viewpoint of the underlying mechanism of polarization behaviours in FEs and relaxor FEs and should be of general interest within the field. Therefore, this strategy can be, in principle, extended to other perovskite materials and possibly also beyond perovskite systems (for example, fluorites), if a frustrated (anti) polar structure is established. In addition, as on-chip capacitor applications continue to advance, frustration-modulated high-performance AFE materials can potentially be promising candidates for multilayer, large-scale and three-dimensional capacitors.

## Online content

Any methods, additional references, Nature Portfolio reporting summaries, source data, extended data, supplementary information, acknowledgements, peer review information; details of author contributions and competing interests; and statements of data and code availability are available at <https://doi.org/10.1038/s41586-024-08505-7>.

- Chu, B. et al. A dielectric polymer with high electric energy density and fast discharge speed. *Science* **313**, 334–336 (2006).
- Yang, L. et al. Perovskite lead-free dielectrics for energy storage applications. *Prog. Mater. Sci.* **102**, 72–108 (2019).
- Palneedi, H., Peddigari, M., Hwang, G.-T., Jeong, D.-Y. & Ryu, J. High-performance dielectric ceramic films for energy storage capacitors: progress and outlook. *Adv. Funct. Mater.* **28**, 1803665 (2018).
- Li, J. et al. Grain-orientation-engineered multilayer ceramic capacitors for energy storage applications. *Nat. Mater.* <https://doi.org/10.1038/s41586-020-0704-x> (2020).
- Cheema, S. S. et al. Giant energy storage and power density negative capacitance superlattices. *Nature* **629**, 803–809 (2024).
- Liu, Z. et al. Antiferroelectrics for energy storage applications: a review. *Adv. Mater. Technol.* <https://doi.org/10.1002/admt.201800111> (2018).
- Qi, H. et al. Ultrahigh energy-storage density in NaNbO<sub>3</sub>-based lead-free relaxor antiferroelectric ceramics with nanoscale domains. *Adv. Funct. Mater.* **29**, 1903877 (2019).
- Si, Y. et al. Antiferroelectric oxide thin-films: fundamentals, properties, and applications. *Prog. Mater. Sci.* **142**, 101231 (2024).
- Pan, H. et al. Ultrahigh energy storage in superparaelectric relaxor ferroelectrics. *Science* **374**, 100–104 (2021).
- Kim, J. et al. Ultrahigh capacitive energy density in ion-bombarded relaxor ferroelectric films. *Science* **369**, 81–84 (2020).
- Han, S. et al. High energy density in artificial heterostructures through relaxation time modulation. *Science* **384**, 312–317 (2024).
- Yang, B. et al. High-entropy enhanced capacitive energy storage. *Nat. Mater.* **21**, 1074–1080 (2022).
- Zhang, T. et al. Superior energy storage performance in antiferroelectric epitaxial thin films via structural heterogeneity and orientation control. *Adv. Funct. Mater.* **34**, 2311160 (2024).
- Li, D. et al. Ultrahigh energy density of antiferroelectric PbZrO<sub>3</sub>-based films at low electric field. *Adv. Funct. Mater.* **33**, 2302995 (2023).
- Shuai, W. et al. Superior and ultrafast energy storage performance of relaxor antiferroelectric HfO<sub>2</sub>-based supercapacitors. *Energy Stor. Mater.* **62**, 102931 (2023).
- Cheng, H. et al. Achieving a high energy storage density in Ag(Nb,Ta)O<sub>3</sub> antiferroelectric films via nanograin engineering. *J. Adv. Ceram.* **12**, 196–206 (2023).
- Er, X., Chen, P., Chen, J. & Zhan, Q. Exploring the energy storage capacity of the Pb<sub>1-x</sub>La<sub>x</sub>HfO<sub>3</sub> system by composition engineering. *J. Eur. Ceram. Soc.* **43**, 4008–4014 (2023).
- Li, J., Li, F., Xu, Z. & Zhang, S. Multilayer lead-free ceramic capacitors with ultrahigh energy density and efficiency. *Adv. Mater.* **30**, e1802155 (2018).
- Li, Y. Z., Wang, Z. J., Bai, Y. & Zhang, Z. D. High energy storage performance in Ca-doped PbZrO<sub>3</sub> antiferroelectric films. *J. Eur. Ceram. Soc.* **40**, 1285–1292 (2020).
- Acharya, M. et al. Exploring the Pb<sub>1-x</sub>Sr<sub>x</sub>HfO<sub>3</sub> system and potential for high capacitive energy storage density and efficiency. *Adv. Mater.* **34**, 2105967 (2022).
- Hao, X., Wang, Y., Zhang, L., Zhang, L. & An, S. Composition-dependent dielectric and energy-storage properties of (Pb,La)(Zr,Sn,Ti)O<sub>3</sub> antiferroelectric thick films. *Appl. Phys. Lett.* **102**, 163903 (2013).
- Li, F. et al. Ultrahigh piezoelectricity in ferroelectric ceramics by design. *Nat. Mater.* **17**, 349–354 (2018).
- Zhang, M. et al. Ultrahigh energy storage in high-entropy ceramic capacitors with polymorphic relaxor phase. *Science* **384**, 185–189 (2024).
- Chen, L. et al. Giant energy-storage density with ultrahigh efficiency in lead-free relaxors via high-entropy design. *Nat. Commun.* **13**, 3089 (2022).
- Song, J., Iwamoto, Y., Iijima, T. & Okamura, S. Electrical properties of antiferroelectric Pb(Zr,Hf)O<sub>3</sub> films fabricated by chemical solution deposition. *Jpn. J. Appl. Phys.* **61**, SN1010 (2022).
- Li, W. et al. Enhanced energy-storage density in (Pb<sub>0.98</sub>La<sub>0.02</sub>)(Zr<sub>0.45-x</sub>Sn<sub>0.55</sub>Hf<sub>x</sub>)<sub>0.995</sub>O<sub>3</sub> antiferroelectric ceramics. *Scripta Mater.* **242**, 115959 (2024).
- Jiang, R.-J. et al. Atomic insight into the successive antiferroelectric–ferroelectric phase transition in antiferroelectric oxides. *Nano Lett.* **23**, 1522–1529 (2023).
- Viehland, D. Transmission electron microscopy study of high-Zr-content lead zirconate titanate. *Phys. Rev. B* **52**, 778–791 (1995).
- Yu, Z. et al. Room-temperature stabilizing strongly competing ferrielectric and antiferroelectric phases in PbZrO<sub>3</sub> by strain-mediated phase separation. *Nat. Commun.* **15**, 3438 (2024).
- Pan, H. et al. Ultrahigh-energy density lead-free dielectric films via polymorphic nanodomain design. *Science* **365**, 578–582 (2019).
- Yang, J. et al. Field-induced strain engineering to optimize antiferroelectric ceramics in breakdown strength and energy storage performance. *Acta Mater.* **257**, 119186 (2023).
- Shen, B. Z. et al. Enhanced energy-storage performance of an all-inorganic flexible bilayer-like antiferroelectric thin film via using electric field engineering. *Nanoscale* **12**, 8958–8968 (2020).
- Ma, B. et al. PLZT film capacitors for power electronics and energy storage applications. *J. Mater. Sci., Mater. Electron.* **26**, 9279–9287 (2015).
- Gao, H. et al. Enhanced electrocaloric effect and energy-storage performance in PBLZT films with various Ba<sup>2+</sup> content. *Ceram. Int.* **42**, 16439–16447 (2016).
- Zhang, T. et al. Tunable polarization-driven superior energy storage performance in PbZrO<sub>3</sub> thin films. *J. Adv. Ceram.* **12**, 930–942 (2023).
- Zhang, Y. et al. High energy storage performance of PZO/PTO multilayers via interface engineering. *ACS Appl. Mater. Interfaces* **15**, 7157–7164 (2023).
- Viegas, A. E., Kuehnel, K., Mart, C., Czernohorsky, M. & Heitmann, J. Stabilizing antiferroelectric-like aluminum-doped hafnium oxide for energy storage capacitors. *Adv. Eng. Mater.* **25**, 2300443 (2023).
- Ali, F. et al. Silicon-doped hafnium oxide anti-ferroelectric thin films for energy storage. *J. Appl. Phys.* **122**, 144105 (2017).
- Payne, A. et al. Dielectric, energy storage, and loss study of antiferroelectric-like Al-doped HfO<sub>2</sub> thin films. *Appl. Phys. Lett.* **117**, 221104 (2020).
- Yi, S.-H., Lin, H.-C. & Chen, M.-J. Ultra-high energy storage density and scale-up of antiferroelectric TiO<sub>2</sub>/ZrO<sub>2</sub>/TiO<sub>2</sub> stacks for supercapacitors. *J. Mater. Chem. A* **9**, 9081–9091 (2021).
- Park, M. H. et al. Thin Hf<sub>0.5</sub>Zr<sub>1.5</sub>O<sub>2</sub> films: a new lead-free system for electrostatic supercapacitors with large energy storage density and robust thermal stability. *Adv. Energy Mater.* **4**, 1400610 (2014).
- Lomenzo, P. D., Chung, C.-C., Zhou, C., Jones, J. L. & Nishida, T. Doped Hf<sub>0.5</sub>Zr<sub>0.5</sub>O<sub>2</sub> for high efficiency integrated supercapacitors. *Appl. Phys. Lett.* **110**, 232904 (2017).
- Pešić, M., Hoffmann, M., Richter, C., Mikolajick, T. & Schroeder, U. Nonvolatile random access memory and energy storage based on antiferroelectric like hysteresis in ZrO<sub>2</sub>. *Adv. Funct. Mater.* **26**, 7486–7494 (2016).
- Shu, L. et al. Partitioning polar-slush strategy in relaxors leads to large energy-storage capability. *Science* **385**, 204–209 (2024).
- Yang, B. B. et al. Engineering relaxors by entropy for high energy storage performance. *Nat. Energy* **8**, 956–964 (2023).
- Pan, W., Zhang, Q., Bhalla, A. & Cross, L. E. Field-forced antiferroelectric-to-ferroelectric switching in modified lead zirconate titanate stannate ceramics. *J. Am. Ceram. Soc.* **72**, 571–578 (1989).
- Mohapatra, P., Johnson, D. D., Cui, J. & Tan, X. Effect of electric hysteresis on fatigue behavior in antiferroelectric bulk ceramics under bipolar loading. *J. Mater. Chem. C* **9**, 15542–15551 (2021).
- Shvartsman, V. V., Lupascu, D. C. & Green, D. J. Lead-free relaxor ferroelectrics. *J. Am. Ceram. Soc.* **95**, 1–26 (2012).
- Li, Q. et al. Flexible high-temperature dielectric materials from polymer nanocomposites. *Nature* **523**, 576–579 (2015).
- Chen, J. et al. Ladderphane copolymers for high-temperature capacitive energy storage. *Nature* **615**, 62–66 (2023).

**Publisher's note** Springer Nature remains neutral with regard to jurisdictional claims in published maps and institutional affiliations.

Springer Nature or its licensor (e.g. a society or other partner) holds exclusive rights to this article under a publishing agreement with the author(s) or other rightsholder(s); author self-archiving of the accepted manuscript version of this article is solely governed by the terms of such publishing agreement and applicable law.

© The Author(s), under exclusive licence to Springer Nature Limited 2025

## Methods

### Precursor solutions and films preparation

Raw materials, including lead acetate (Macklin, 99.99%), zirconium n-propoxide (Alfa Aesar, 70%), hafnium 2,4-pentanedionate (Alfa Aesar, 97%), lanthanum nitrate (Alfa Aesar, 99.99%), scandium nitrate (Aladdin, 99.99%), sodium acetate (Alfa Aesar, 99.997%), bismuth acetate (Alfa Aesar, 99.999%), tetrabutyl titanate (Aladdin, 98%) and nickel acetate (Alfa Aesar, 99.999%) were used to prepare the precursor solutions. The solvent was 2-methoxyethanol (Aladdin, 99.5%) and propionic acid (Meryer, 99.5%). A 20% excess of lead was added to compensate for the volatilization of Pb in the heat treatment. (1) For the production of Hf-doped PbZrO<sub>3</sub> compositions, lead acetate and hafnium 2,4-pentanedionate were initially dissolved in 2-methoxyethanol at 120 °C for 1 h. Subsequently, zirconium n-propoxide was introduced into the solution upon cooling to room temperature. The resultant mixture underwent continuous stirring at ambient conditions for 3 h to ensure complete dissolution, yielding a clear and transparent precursor solution. The precursor solution concentration of 0.2 M was subject to adjustment by the addition of 2,4-pentanedionate. (2) For the case of PZH-LS compositions, stoichiometric quantities of lead acetate, hafnium 2,4-pentanedionate, lanthanum nitrate and scandium nitrate were dissolved in 2-methoxyethanol at 120 °C for 1 h. Following this, zirconium n-propoxide was incorporated into the solution upon reaching room temperature, and the resulting mixture underwent continuous stirring for 3 h until complete dissolution. Similar steps were undertaken for the preparation of PZH-NBT compositions, albeit utilizing propionic acid as the solvent medium. (3) For the LaNiO<sub>3</sub> precursor solution, stoichiometric lanthanum nitrate and nickel acetate were dissolved into 2-methoxyethanol at 60 °C for 10 min and then continuously stirred at room temperature for 5 h to obtain a clear and transparent precursor solution.

Preparation of LaNiO<sub>3</sub> buffered LaAlO<sub>3</sub> substrates was as follows. The LaNiO<sub>3</sub> precursor was deposited onto LaAlO<sub>3</sub> (001) single-crystal substrates using the spin-coating technique, operating at a speed of 5,000 rpm for a duration of 20 s. Subsequently, the deposited wet films were subjected to baking at 200 °C for 2 min to facilitate the evaporation of the organic solvent, followed by pyrolysis at 450 °C for 5 min to eliminate residual organics. Final crystallization of the films occurred at 700 °C for 10 min. This sequence of procedures was iterated twice to minimize LaNiO<sub>3</sub> electrode resistivity. For the preparation of PZH, PZH-LS and PZH-NBT films, following a 48-h ageing period, precursor solutions were spin-coated onto the LaNiO<sub>3</sub> buffered LaAlO<sub>3</sub> substrates at a speed of 3,000 rpm for 30 s. The resulting wet films underwent baking at 200 °C for 1 min to remove organic solvents, followed by pyrolysis at 450 °C for 5 min to eliminate residual organics. This process was repeated several times to achieve the desired film thickness (Supplementary Figs. 21 and 22). To prevent Pb loss during subsequent heat treatment, a 0.4 M PbO precursor solution was deposited onto the film surfaces at 3,000 rpm for 30 s as a capping layer. The small amounts of residual PbO layer had negligible effect on our conclusions because the same preparation processes were adopted for all films. Finally, the films were crystallized at 650 °C for 200 s.

### Characterizations

The crystal structures of the fabricated films underwent characterization utilizing an X-ray diffractometer (Empyrean, Malvern Panalytical) employing Cu K $\alpha$  radiation (wavelength  $\lambda = 1.5418$  Å). Film thicknesses and surface microstructures were analysed using field-emission scanning electron microscopy (SEM, MERLIN VP Compact, ZEISS). Electrical properties were measured using circular Au top electrodes (approximately 100  $\mu\text{m}$  diameter and approximately 100 nm thickness) deposited onto the film surface by means of a stainless-steel shadow mask. Ferroelectric and leakage current properties were evaluated using a Sawyer–Tower circuit (Precision Multiferroic II, Radiant

Technologies). Bipolar hysteresis  $P$ – $E$  loops were generated using bipolar triangular voltage waves at a frequency of 10 kHz, from which the energy storage density and efficiency were calculated. Leakage currents were measured by applying a direct current voltage ladder waveform with a soak time of 200 ms and a measurement time of 400 ms for each data point. Accelerated charging and discharging cycling tests were conducted by subjecting the samples to successive bipolar triangular voltage waves, followed by the acquisition of bipolar  $P$ – $E$  loops. Dielectric permittivity and loss tangent were assessed across a wide frequency and temperature range using a precision impedance analyser (HP 4294 A, Agilent) with an alternating current voltage of 0.5 V. The discharging time and energy density were tested on a fast discharge test system (PK-CPR1901-20012, PolyK Technologies, LLC USA). By measuring the discharged current versus time curves, the discharging energy density ( $U_{\text{dis}}$ ) can be calculated by the formula  $U_{\text{dis}} = \frac{R \int I(t)^2 dt}{V}$ , where  $R$  is the load resistor (20 k $\Omega$ ),  $I$  is the discharged current,  $t$  is the time and  $V$  is the sample volume. The characteristic discharging time ( $t_{0.9}$ ) was taken to be when 90% of the energy had been discharged.

### TEM and STEM characterizations

Cross-sectional samples for transmission electron microscopy (TEM) and STEM observations were prepared by slicing, gluing, mechanical grinding, dimpling and finally ion milling using a Gatan Precision Ion Polishing System 695. Before ion milling, the samples were dimpled down to 20  $\mu\text{m}$  using a Gatan 656 Dimple Grinder. At the beginning of ion milling, the incident angles of 9° and milling voltage of 5.5 kV were used. Then, the incident angle and voltage were gradually reduced to 5° and 4.0 kV, respectively. Finally, the ion milling voltage was set at 0.1 kV for 5 min to reduce the amorphous layer produced in the milling process. The specimens were cleaned before they were allowed to be inserted into the TEM. Diffraction contrast TEM images and SAED patterns were acquired using a conventional TEM (JEOL F200). All HAADF-STEM images were acquired by an aberration-corrected scanning TEM (Spectra 300 microscope equipped with double aberration ( $C_s$ ) correctors from CEOS, which was operated at 300 kV). The atomic-scale HAADF-STEM images for acquiring the A-site cation displacement map were recorded by STEM drift corrected frame integration. Each high-resolution HAADF-STEM image was acquired by adding up 20 original images with the dwell time of 100 ns, using Velox software (Thermo Fisher Scientific) for image acquisition and processing. Acquiring images in this way can reduce the influence of sample drift and scanning noises. To reduce the noises in the obtained images, a Wiener filter was used for all atomic-scale HAADF-STEM images. The positions of atom columns in the HAADF-STEM images were determined on the basis of the two-dimensional Gaussian fitting<sup>51</sup>, which was carried out using the MATLAB software. Because of the generally small displacements of the B-site cation in PZO-based materials, their positions were averaged as reference sites for calculating A-site cation displacement. In addition, the lattice distribution features could be distinguished by calculating the horizontal lattice rotation ( $R_x$ ) (the angle between the lines of two neighbouring A-site cations and the horizontal direction).

### Phase-field simulations

An AFE can be thermodynamically described as two order parameters  $P$  and  $q$  (ref. 52). The competition of  $P$  and  $q$  determines symmetry and stability of AFE and FE phases. Here we focus more on polarization behaviours and thus take  $P$  as the only order parameter, following a triple-well energy landscape (Supplementary Fig. 23)<sup>53</sup>. The phase-field simulation for AFEs treats the polarization vector of an enlarged unit cell,  $\mathbf{P} = (P_1, P_2, P_3)$ , as the order parameter and solves the time-dependent Landau–Ginzburg–Devonshire equation

$$\frac{\partial \mathbf{P}}{\partial t} = -L \frac{\partial F}{\partial \mathbf{P}} \quad (1)$$

# Article

where  $L$  is the kinetic coefficient,  $t$  is the time and  $F$  is the free energy, which is expressed as the integral of the individual free energy densities

$$F = \iiint (f_{\text{Landau}} + f_{\text{gradient}} + f_{\text{elastic}} + f_{\text{electric}}) dV \quad (2)$$

The Landau energy is approximated to a six-order polynomial with a triple-well landscape with a positive coefficient of the square term, which is distinguished from the double-well landscape for ferroelectrics with a negative coefficient of the square term. The free energy terms are therefore given by

$$\begin{aligned} f_{\text{Landau}} = & \alpha_1(P_1^2 + P_2^2 + P_3^2) + \alpha_{11}(P_1^4 + P_2^4 + P_3^4) \\ & + \alpha_{12}(P_1^2P_2^2 + P_2^2P_3^2 + P_1^2P_3^2) + \alpha_{111}(P_1^6 + P_2^6 + P_3^6) \\ & + \alpha_{112}[P_1^4(P_2^2 + P_3^2) + P_2^4(P_1^2 + P_3^2) + P_3^4(P_1^2 + P_2^2)] \\ & + \alpha_{123}P_1^2P_2^2P_3^2 \end{aligned} \quad (3)$$

$$\begin{aligned} f_{\text{gradient}} = & \frac{1}{2}G_{11}(P_{1,1}^2 + P_{2,2}^2 + P_{3,3}^2) \\ & + \frac{1}{2}G_{44}[(P_{1,2} + P_{2,1})^2 + (P_{2,3} + P_{3,2})^2 + (P_{1,3} + P_{3,1})^2] \\ & + \frac{1}{2}G'_{44}[(P_{1,2} - P_{2,1})^2 + (P_{2,3} - P_{3,2})^2 + (P_{1,3} - P_{3,1})^2] \end{aligned} \quad (4)$$

$$f_{\text{elastic}} = \frac{1}{2}C_{ijkl}(\varepsilon_{ij} - \varepsilon_{ij}^0)(\varepsilon_{kl} - \varepsilon_{kl}^0) \quad (5)$$

$$f_{\text{electric}} = -\frac{1}{2}K_{ij}\varepsilon_0E_iE_j - E_iP_i \quad (6)$$

where  $\alpha$ ,  $G$ ,  $C$ ,  $\varepsilon_{ij}$ ,  $\varepsilon_{ij}^0$ ,  $K$ ,  $\varepsilon_0$  and  $E$  are the Landau coefficients, gradient coefficients, elastic stiffness, total strain, spontaneous strain, background dielectric constant, dielectric permittivity of vacuum and local electric field, respectively<sup>54</sup>. The Landau coefficients were chosen to fit the pure  $\text{PbZrO}_3$   $P$ - $E$  loop. The spontaneous strain, which is also called the eigenstrain, is calculated using the electrostrictive coefficients  $Q$  as

$$\varepsilon_{ii}^0 = Q_{11}P_i^2 + Q_{12}(P_j^2 + P_k^2) \quad (7)$$

$$\varepsilon_{ij}^0 = Q_{44}P_iP_j \quad (8)$$

The local field can be obtained by calculating the gradient of the electric potential  $\mathbf{E} = -\nabla\varphi$ , which is solved using the Poisson equation

$$K_{ij}\frac{\partial^2\varphi}{\partial x_i\partial x_j} = \frac{\partial P_i}{\varepsilon_0\partial x_i} \quad (9)$$

The bound charge distribution is given by

$$Q = -\nabla \cdot \mathbf{P} \quad (10)$$

The values of the coefficients for AFEs are given in Supplementary Information Table 1 (ref. 55).

The simulation of the total grid had dimensions of  $128\Delta \times 128\Delta \times 1\Delta$  in the  $[100]$ ,  $[010]$  and  $[001]$  directions, where  $\Delta = 1.0$  nm was the grid

spacing. The initial polarization nuclei consisted of randomized noise within  $0.001$  C m<sup>-2</sup> in magnitude. The periodic boundary condition was employed and an electric field along the  $[010]$  direction was applied to obtain bound charge, electric field, polarization and strain distribution, and  $P$ - $E$  loops. The frustration was imparted by generating randomized regions with linear dielectric (for non-polar) and ferroelectric (for polar) features. These Landau coefficients can be found in Supplementary Table 2 (FE modified from ref. 56). For A-N type materials, non-polar components were set with different permittivity, and the corresponding transition fields and energy storage performance are mapped in Supplementary Figs. 24 and 25. A permittivity of approximately 50 was sufficient to obtain a high energy storage so this case is placed in Fig. 1d,e.

To support our simulations based on the above methods, we also employed two other models. Details can be found in the Supplementary Information (Supplementary Notes 1 and 2 and Supplementary Figs. 26–33).

The phase-field simulation was conducted using the commercial Mu-Pro modules (<http://mupro.co/>).

## Data availability

The data supporting the findings of this study are available in the paper and the Supplementary Information. All data are available at Figshare (<https://doi.org/10.6084/m9.figshare.27643437.v1>)<sup>57</sup>. Source data are provided with this paper.

- Anthony, S. M. & Granick, S. Image analysis with rapid and accurate two-dimensional Gaussian fitting. *Langmuir* **25**, 8152–8160 (2009).
- Haun, M. J. et al. Thermodynamic theory of  $\text{PbZrO}_3$ . *J. Appl. Phys.* **65**, 3173–3180 (1989).
- Caretta, L. et al. Non-volatile electric-field control of inversion symmetry. *Nat. Mater.* **22**, 207–215 (2023).
- Hong, Z. et al. Stability of polar vortex lattice in ferroelectric superlattices. *Nano Lett.* **17**, 2246–2252 (2017).
- Haun, M. J. *Thermodynamic Theory of the Lead-zirconate-titanate Solid Solution System*. PhD thesis, Pennsylvania State Univ. (1988).
- Bell, A. J. & Cross, L. E. A phenomenological gibbs function for  $\text{BaTiO}_3$  giving correct  $e$  field dependence of all ferroelectric phase changes. *Ferroelectrics* **59**, 197–203 (1984).
- Yang, B. Source data. Figshare <https://doi.org/10.6084/m9.figshare.27643437.v1> (2024).

**Acknowledgements** This work was financially supported by the National Key Research and Development Program of China (grant no. 2021YFB3800601 to Y.-H.L.); the National Natural Science Foundation of China (NSFC) (grant nos 12474095 and 52402323 to B.Y.); the Basic Science Center Project of the National Natural Science Foundation of China (NSFC) (grant no. 52388201 to Y.-H.L. and C.-W.N.); the State Key Laboratory of New Ceramic Materials Tsinghua University (grant no. KFZD202403 to B.Y.); the NSFC (grant nos 5238B201, 52372100 and 51971223 to Y.L., H.H. and Y.-L.Z.); the Guangdong Provincial Quantum Science Strategic Initiative (grant nos GDZX2202001 and GDZX2302001 to X.-L.M.); and the Anhui Provincial Natural Science Foundation (grant no. 2408085ME116 to B.Y.).

**Author contributions** Y.-H.L., B.Y. and Y.L. conceived this study. B.Y. fabricated the samples. B.Y., Z.Z., L.D. and M.Z. carried out the electrical measurements and analysis. Y.L. conducted phase-field simulations under the supervision of Y.-H.L., H.H. and L.-Q.C. R.-J.J. and S.-Z.L. performed TEM and STEM characterizations under the supervision of X.-L.M. and Y.-L.Z. Y.-H.L., C.-W.N., S.Z. and X.-L.M. supervised the study. B.Y., Y.L., R.-J.J., S.L., S.Z., X.-L.M., C.-W.N. and Y.-H.L. wrote the manuscript. All authors discussed the results and revised the manuscript.

**Competing interests** The authors declare no competing interests.

## Additional information

**Supplementary information** The online version contains supplementary material available at <https://doi.org/10.1038/s41586-024-08505-7>.

**Correspondence and requests for materials** should be addressed to Shujun Zhang, Xiu-Liang Ma or Yuan-Hua Lin.

**Peer review information** Nature thanks Suraj Cheema, Bai-Xiang Xu and the other, anonymous, reviewer(s) for their contribution to the peer review of this work.

**Reprints and permissions information** is available at <http://www.nature.com/reprints>.